

ABSTRACT

Title of Document: CHARACTERIZATION AND APPLICATIONS OF FEGA/PZT MULTIFERROIC CANTILEVERS

Yi Wang, Doctor of Philosophy, 2014

Directed By: Professor Ichiro Takeuchi,
Department of Physics,
Department of Materials Science and
Engineering

Multiferroic materials and structures, which possess two or more ferroic properties, have been widely investigated because of their ability to transfer one different form of signals. The magnetoelectric (ME) effect, which results in induced voltage under applied magnetic field, makes multiferroic materials promising in applications for new types of transducers, sensors, and information storage devices. The laminated bulk composite multiferric devices had attracted a lot of attention because of their high ME coefficients, which define the strength of ME coupling.

We fabricated mechanically-resonant ME devices by depositing magnetostrictive FeGa and piezoelectric PZT thin films on Si cantilevers. Various sized cantilevers were found to exhibit different behaviors. With a 1 Oe AC magnetic driving field H_{AC} , the small cantilever ($0.95 \text{ mm} \times 0.2 \text{ mm} \times 5 \text{ }\mu\text{m}$) shows a high ME coefficient ($33 \text{ V}/(\text{cm} \times \text{Oe})$) with a bias DC magnetic field of 66.1 Oe at the resonant frequency f_r of

3833 Hz in vacuum. We found that the f_r of the small cantilever continuously shifts with the bias magnetic field. A magnetic cantilever theory was used to explain this shift. In addition, we are able to demonstrate application of magnetic cantilevers in AC magnetic energy harvesters with an efficiency of 0.7 mW/cm^3 .

By driving the cantilever into the nonlinear regime with an AC magnetic field larger than 3 Oe or AC electric field larger than 5 mV, we are able to demonstrate its application in a robust multi-mode memory device based on bistable solutions of the Duffing oscillation. We can use the driving frequency, the driving amplitude, DC magnetic field, or DC electric field as the input, and use bistable vibration amplitudes of the device as the output.

We also show that parametric amplification can be used to substantially increase the ME coefficient by adding a pump voltage on the PZT layer. The parametric gain is sensitive to both the phase of pumping signal and the phase of the driving signal. The gain diverges as the pump voltage approaches the threshold. With parametric amplification, the ME coefficient can be boosted to a value as large as $2 \times 10^6 \text{ V/(cm} \times \text{Oe)}$ from $33 \text{ V/(cm} \times \text{Oe)}$.

CHARACTERIZATION AND APPLICATIONS OF FE₂GA/PZT MULTIFERROIC
CANTILEVERS

By

Yi Wang

Dissertation submitted to the Faculty of the Graduate School of the
University of Maryland, College Park, in partial fulfillment
of the requirements for the degree of
Doctor of Philosophy
2014

Advisory Committee:
Professor Ichiro Takeuchi, Chair
Professor Robert Anderson
Professor Richard Greene
Professor Frederick Wellstood
Professor Christopher Lobb

© Copyright by
Yi Wang
2014

Dedication

To my wife

Ding, Yanni

Parents

Wang, Qitie

Li, Maiyun

Acknowledgements

First, I would like to thank my advisor, Professor Ichiro Takeuchi, who has offered me a great opportunity to study many interesting projects. He guided me throughout the Ph.D. study with his patience and insights. I am deeply thankful to have him as my advisor and friend. I also would like to thank the rest of my committee members: Professors J. Robert Anderson, Richard Greene, Frederick Wellstood, and Christopher Lobb. They have been very helpful throughout the time when I studied in CNAM and very supportive during the graduation process.

I would like to thank all my group members and colleagues including Anbu Varatharajan, Arun Luykx, Fengxia Yang, Gilad Kusne, Iain Kierzewski, Jason Hatrick-Simpers, Jing Li, Kui Jin, Jonghee Lee, Jongmoon Shin, Joseph Langreo, Lei Fang, Monti Tamara, Nathan Orloff, Richard Suchoski, Saya Takeuchi, Se-Young Jeong, Sean Fackler, Shintaro Yasui, Shingo Maruyama, Stephen Yang, Tamin Tai, Tieren Gao, Xiaohang Zhang, Yangang Liang, and Yiming Wu, for many helpful discussions.

I would like to especially thank Tiberiu-Dan Onuta for fabricating the small cantilever device and working with me closely on my thesis projects. I would also like to thank Christian Long for contributing to the small cantilever characterization and sharing his knowledge of near-field microwave microscopy and MATLAB. I would like to thank Dr. Samuel Lofland for contributing to the theory I used in this thesis. I would like to thank Peng Zhao for help with the large magnetoelectric device I used for the magnetic field sensing, Luz Sanchez for providing the assistance with the piezoelectric PZT, and Dwight Hunter for providing help with the magnetostrictive FeGa. I would like to thank everyone in the Physics Department, the Materials Science and Engineering department, CNAM, Fablab, machine shop, NISP lab, and other facilities on campus for providing knowledge or service.

My deepest thanks are to my wife, Yanni Ding, and my parents, Maiyun Li, and Qitie Wang, for providing endless love and support during my Ph.D. study.

Table of Contents

Dedication.....	ii
Acknowledgements.....	iii
Table of Contents.....	v
List of Tables.....	ix
List of Figures.....	x
List of Abbreviations.....	xiv
Chapter 1: Introduction to Multiferroic Materials and Structures.....	1
1.1 Multiferroic Materials.....	1
1.2 History of Multiferroic Materials.....	2
1.3 Types of Multiferroic Materials.....	4
1.3.1 Single Phase Multiferroics.....	4
1.3.2 Composite Multiferroics.....	6
1.4 Chapter Descriptions.....	12
Chapter 2: Multiferroic Materials and the Magnetoelectric Coupling.....	14
2.1 Introduction.....	14
2.2 Piezoelectricity and Ferroelectricity.....	14
2.2.1 Piezoelectricity.....	14
2.2.2 Ferroelectricity.....	19
2.2.3 The Perovskite Structure.....	21
2.2.4 Lead Zirconate Titanate (PZT).....	22
2.3 Magnetism and Magnetostriction.....	23
2.3.1 Diamagnetism, Paramagnetism, and Ferromagnetism.....	23

2.3.2 Magnetostriction.....	25
2.3.3 Iron Gallium (FeGa)	27
2.4 Magnetoelectric Coupling.....	27
2.4.1 Magnetic Field Sensing.....	27
2.4.2 The ME coefficient and the ME Magnetic Field Sensors.....	29
2.4.3 Characteristics of Large ME Devices (4.5 mm × 20 mm × 30 μm).....	33
2.4.4 The Clamping Effect on Thin Films from the Substrate.....	37
2.5 Conclusion.....	39
Chapter 3: Basic Characteristics of Multiferroic Cantilevers and Their Application in	
Energy Harvesting	40
3.1 Magnetic Field Sensing Mode.....	40
3.2 Fabrication of FeGa/PZT Multiferroic Cantilevers.....	41
3.3 Cantilever Theory.....	43
3.4 Measurement Setup.....	46
3.5 Butterfly Curves for Small Cantilevers (0.95 mm × 0.2 mm × 5 μm).....	49
3.6 Derivation of $f_{R, magnetic}(H_{DC})$ Expression and the Fitting of the Data.....	51
3.7 Energy Harvesting Applications.....	56
3.8 Conclusion.....	59
Chapter 4: Dynamic Multiferroic Memory with Nonlinearity	
4.1 Introduction	60
4.2 Nonlinearity: the Origin of Hysteresis.....	61
4.3 Electric-field Driven Mode.....	64
4.3.1 Nonlinearity and Hysteresis.....	64

4.3.2 Switchable Memory Based on Nonlinear Mechanical Vibration.....	68
4.3.3 The Role Magnetic Layer Plays in Electric-field Driven Mode.....	73
4.3.4 Phase Diagram Analysis.....	74
4.4 Magnetic-field Driven Mode	76
4.5 How the Different Driving Modes Are Related.....	78
4.6 Multi-mode Memory based on Nonlinear Hysteresis.....	80
4.6.1 Memory Switch Mechanism.....	80
4.6.2 Need for New Memory Devices.....	82
4.6.3 DC Magnetic Field or DC Electric Field Triggered Memories.....	83
4.6.4 Frequency Modulation (FM) and Amplitude Modulation (AM) triggered Memory where FM pulses and AM pulses are interchangeable.....	87
4.7 The Size Effect.....	90
4.8 Conclusion.....	91
Chapter 5: Colossal Magnetoelectric Effect Assisted by Parametric Amplification.....	92
5.1 Abstract.....	92
5.2 Parametric Amplification Theory.....	92
5.3 Parametric Amplification Setup.....	98
5.4 Experiment Data.....	100
5.4.1 Measurement of the Phase Sensitive Gain.....	100
5.4.2 Nonlinear Increase of Gain with Pumping Voltage	102
5.4.3 Quality Factor as a Function of Gain or ME voltage.....	106
5.5 Assessing the Noise.....	107
5.6 Conclusion.....	108

Chapter 6: Summary and Future Work.....	110
Appendix.....	114
A.1 Using Nyquist-like Plot to Subtract Inductive Signal.....	114
A.1 Fit Frequency Response with Lorentzian Function.....	117
Bibliography.....	118
Publications and Presentations.....	127

List of Tables

Table 1.1 Summary of some ME bulk composites and their ME coefficients.....	9
Table 2.1 Materials' magnetostriction, bias magnetic field needed to optimize their ME coefficients, relative permeability, and magnetoelastic sensitivity.....	32

List of Figures

Fig. 1.1 The definition of multiferroic	2
Fig. 1.2 R3c structure of BiFeO ₃	5
Fig. 1.3 Schematic view of G-type antiferromagnetic structure of BiFeO ₃	6
Fig. 1.4 Three types of magnetoelectric composite schemes.....	8
Fig. 2.1 Piezoelectric coefficients: d ₃₁ and d ₃₃	18
Fig. 2.2a Ferroelectric P-E Hysteresis.....	20
Fig. 2.2b Paraelectric P-E Curve.....	20
Fig. 2.3 The cubic phase and the tetragonal phase of perovskite structures.....	22
Fig. 2.4 Magnetization vs Magnetic field (M-H Loop).....	25
Fig. 2.5 Typical magnetostriction vs H _{DC} for positive magnetostrictive materials.....	31
Fig. 2.6 Butterfly curve: ME coefficient as a function of DC bias magnetic field.....	35
Fig. 2.7 The ME coefficient in vacuum vs the ME coefficient in air.....	36
Fig. 2.8 Schematic illustration of FeGa/PZT large cantilever (4.5 mm × 20 mm × 30 μm).	37
Fig. 2.9 The ME coefficient as a function of cantilever thickness.....	38
Fig. 3.1 The heterostructure of FeGa/PZT multiferroic cantilever.....	41
Fig. 3.2 Cantilevers with silicon nitride films of different thicknesses.....	42

Fig. 3.3 Examples of applications with cantilevers.....	44
Fig. 3.4 Different vibration modes of a cantilever.....	46
Fig. 3.5 Schematic of ME measurement with (0.95 mm × 0.2 mm × 5 μm) cantilevers.....	47
Fig. 3.6 Coils and vacuum chamber are mounted inside of a mu-metal box on a sand box..	48
Fig. 3.7 DC and AC Coils are calibrated with a gauss-meter.....	49
Fig. 3.8 ME signal and the resonant frequency vs DC bias magnetic field.....	50
Fig. 3.9 Schematic of a heterostructured multiferroic cantilever and its coordinates.....	52
Fig. 3.10 Characteristics of a multiferroic cantilever vs the theoretical prediction	56
Fig. 3.11 Energy harvesting scheme.....	57
Fig. 3.12 Power and voltage in the energy harvesting application.....	58
Fig. 4.1 Simulation of amplitude and phase vs driving frequency for Duffing oscillators.....	63
Fig. 4.2 Schematic of the electric-field driven mode.....	65
Fig. 4.3 Experimental data: Increasing driving excitation leads to nonlinear tilting of frequency response curve.....	66
Fig. 4.4 The electric-field driven mode: the frequency response vs H _{DC}	67
Fig. 4.5 Switching memory test triggered by tuning the driving frequency.....	69
Fig. 4.6 Schematic figure of the cantilever as a memory device.....	71

Fig. 4.7 Evolution of potential well due to tuning the driving frequency.....	72
Fig. 4.8 Translation of frequency-response hysteresis loop with varying H_{DC}	74
Fig. 4.9 Multiferroic cantilever dynamics in the “phase-space” representation at $H_{DC} = 0$..	75
Fig. 4.10 Magnetic linear/nonlinear mode: the ME signal vs the driving frequency.....	77
Fig. 4.11 The connection of different driving modes.....	79
Fig. 4.12 Switching mechanism.....	81
Fig. 4.13 Frequency hysteresis bistability as a function of H_{DC} or E_{DC}	83
Fig. 4.14 Operation of multiferroic memory using H_{DC} and E_{DC} as input.....	86
Fig. 4.15 FM and AM used as the input of the memory, respectively.....	89
Fig. 4.16 Interchangeable operation of FM and AM Mode.....	90
Fig. 5.1 (a) Swing by changing center of mass.....	93
Fig. 5.1 (b) Swing by rotating.....	93
Fig. 5.2 Signal relations in parametric amplification.....	94
Fig. 5.3 Theoretical gain vs pumping phase θ and driving phase ϕ , for $k_p/k_t = 0.5$	98
Fig. 5.4 Block diagram showing the system in parametric amplification mode.....	99
Fig. 5.5 Phase sensitive parametric amplification data.....	101
Fig. 5.6 Experimental and theoretical gain as a function of the pumping voltage.....	102

Fig. 5.7 The ME signals vs pumping voltage, for different driving fields.....	104
Fig. 5.8 The ME coefficient vs pump voltage for driving magnetic field of 282 pT.....	105
Fig. 5.9 The quality factor as a function of the gain and the ME Voltage.....	107
Fig. A.1 Nyquist adjustment process.....	116
Fig. A.2 Frequency responses fitted with a Lorentzian function.....	117

List of Abbreviations

FeGa Iron Gallium

PZT $\text{Pb}(\text{Zr}_x\text{Ti}_{1-x})\text{O}_3$

ME Magnetoelectric

AC Alternate Current

DC Direct Current

Tc Curie temperature

SQUID Superconducting Quantum Interference Devices

MTJ Magnetic Tunnel Junctions

CNAM Center for Nanophysics and Advanced Materials

RTA Rapid Thermal Annealing

CVD Chemical Vapor Deposition

ONO Silicon Oxide-nitride-oxide Stack

MEMS/NEMS Micro/Nano-electromechanical System

SEM Scanning Electron Microscope

AFM Atomic Force Microscope

RMS Root Mean Square

Oe Oersted

MRAM Magnetoresistive Random Access Memory

FeRAM Ferroelectric Random Access Memory

FM Frequency Modulation

AM Amplitude Modulation

PA Parametric Amplification

Eq. Equation

Fig. Figure

Q Quality Factor

MPB Morphotropic Phase Boundary

Re Real Part of a Complex Number

Im Imaginary Part of a Complex Number

Units:

C = coulomb, m = meter, N = Newton, V = Volt, A = Ampere, s = second, F = Faraday, Hz = Hertz

Unit Prefix:

m/ μ /n/p/f = mili/micro/nano/pico/fento = $10^{-3}/10^{-6}/10^{-9}/10^{-12}/10^{-15}$

K/M/G = kilo/mega/giga = $10^3/10^6/10^9$

Chapter 1: Introduction to Multiferroic Materials and Structures

1.1 Multiferroic Materials

Multiferroic materials possess two or more primary ferroic properties (ferroelectricity, magnetism, and ferroelasticity). This is schematically shown in Fig. 1.1 [1]. Ferroelectric materials have spontaneous electric polarization which is reversible under an applied electric field. Ferromagnetic materials have spontaneous magnetization that is reversible under an applied magnetic field. Ferroelastic materials have spontaneous strain which is reversible under stress. Coupling of ferroelectricity and elasticity is known as the piezoelectricity. Similarly, simultaneous ferromagnetism and elasticity lead to magnetostriction. The effect where electric polarizations change under magnetic field is called the magnetoelectric (ME) effect. The effect where electric field induces magnetization is called the converse magnetoelectric effect [2]. The magnetoelectric (ME) coefficient α , which is used to quantify the strength of the ME coupling, is defined as the electric field E induced in the material per unit applied magnetic field H . With their ability to transform different forms of signal, multiferroic materials have the potential to deliver new types of transducers, actuators, sensors, and information storage devices.

Among multiferroic materials, magnetoelectric materials have been intensely investigated because of their possible application to magnetic field sensing, energy harvesting, wireless control systems, and electric controlled magnetic memory devices. Often, when present day researchers use the term ‘multiferroics’, they are referring to magnetoelectric materials.

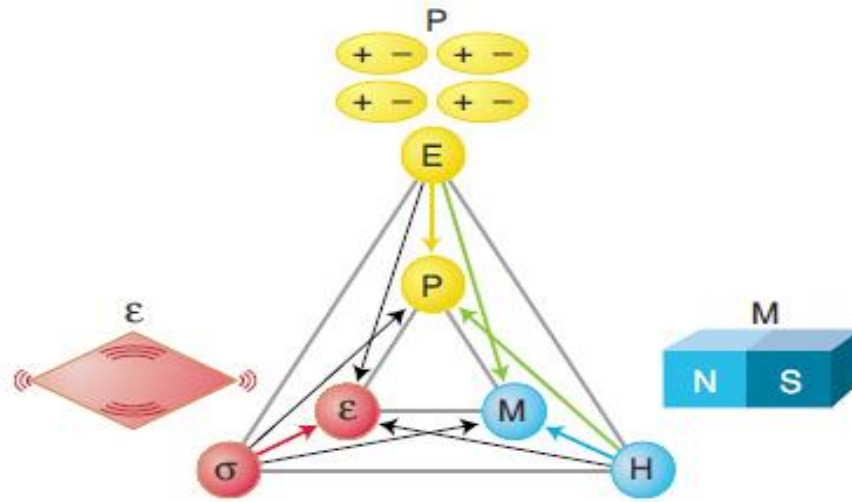


Fig. 1.1 The electric polarization P , magnetization M , and strain ϵ are controlled by the electric field E , magnetic field H , and stress σ , respectively. Two or more ferroic properties coexist in multiferroic materials. In a magnetoelectric multiferroic, P may be modulated by H or M may be induced by E (green arrows). From Ref [1].

1.2 History of Multiferroic Materials

Ferromagnetic materials in the form of naturally formed magnets were first discovered by ancient civilizations. The earliest known descriptions of magnetic materials are from Greece, India, and China and date from around 500 BC. Many centuries later, ferroelectricity was discovered in 1920 in Rochelle salt by Valasek [3]. It was first conjectured by Pierre Curie in 1884 that there could be materials which can be electrically polarized by magnetic field and magnetized by electric field [4]. Since then, researchers have looked for coexistence of ferroelectricity and ferromagnetism. In 1926, Peter Debye coined the term ‘magnetoelectric’ [5]. In 1957, L. D. Landau and E. M. Lifshitz gave a more rigorous prediction of the magnetoelectric effect only in time-asymmetric media, *e.g.*, magnetically ordered media [6]. Based on this, in

1960, Dzyaloshinskii predicted that the magnetoelectric effect should exist in the antiferromagnetic material chromium oxide Cr_2O_3 [7]. A few months later, D. Astrov observed electric field induced magnetization in Cr_2O_3 [8]. G. T. Rado and V. J. Folen discovered magnetically induced polarization in Cr_2O_3 [9]. In 1966, coexistence of ferroelectricity and ferromagnetism was found in Nickel-Iodine Boracite $\text{Ni}_3\text{B}_7\text{O}_{13}\text{I}$ below 61 K [10]. $\text{Ni}_3\text{B}_7\text{O}_{13}\text{I}$ is in a large crystal structure family with the general formula $\text{M}_3\text{B}_7\text{O}_{13}\text{X}$, where M can be Mg, Cr, Mn, Fe, Co, Ni, Cu, Zn, etc, and X can be OH, F, Cl, Br, I or NO_3 . It turns out that most of the boracites become ferroelectric and weakly ferromagnetic at low temperatures. In 1960s, Smolensky was seeking multiferroics by replacing some of the d^0 B cations in ferroelectric perovskite oxides (with formula ABO_3) by magnetic d^n cations. His first synthesized ferromagnetic ferroelectric material was $(1 - x)\text{Pb}(\text{Fe}_{2/3}\text{W}_{1/3})\text{O}_3 - x\text{Pb}(\text{Mg}_{1/2}\text{W}_{1/2})\text{O}_3$ [11]. As this field started to attract more and more attention, a series of workshops of a Magnetoelectric Interaction Phenomena in Crystals (MEIPIC) were organized. Before the first MEIPIC (1973) was held, more than 80 magnetoelectric compounds had been found.

While some researchers were making efforts to find new single phase multiferroics, others were studying composite materials. Initially, researchers used unidirectional solidification in a eutectic composite to create a composite of ferroelectric BaTiO_3 and ferromagnetic CoFe_2O_4 [12]. Composite materials achieve magnetoelectric coupling through mechanical interaction between the piezoelectric phase and magnetostrictive phase. Compared to single phase multiferroics with relatively weak magnetoelectric coupling ($\alpha = 20 \text{ mV}/(\text{cm} \times \text{Oe})$ for Cr_2O_3 [13]), composite materials can display much stronger magnetoelectric coupling [14,15], and thus they can be more attractive for applications such as magnetic field sensors. Recently, the ME coefficient of composites has reached $20 \text{ kV}/(\text{cm} \times \text{Oe})$ for resonant devices [16]. Using thin film techniques,

material scientists are able to synthesize higher quality piezoelectric materials [17,18] and magnetostrictive materials [19-21].

Multiferroic materials convert magnetic energy to electric energy, and vice versa. With improvement in efficiency of converting magnetic energy into electric energy, magnetoelectric coupled materials could be promising in applications of magnetic field sensors [22-25], energy harvesters [21,26-28], and energy transducers. The converse magnetoelectric effect is expected to realize electrically controlled magnetic domains [29-31], which can potentially be used for magnetic information storage and reduce the energy required for read and write processes.

1.3 Types of Multiferroic Materials

1.3.1 Single Phase Multiferroics

Single phase materials that exhibit both ferroelectricity and magnetism are rare. This is because ferroelectricity requires empty d orbitals, while ferromagnetism usually requires partially filled d orbitals [32]. However, this contra-indication can be broken in some circumstances and there are some single phase multiferroic materials.

$\text{Ni}_3\text{B}_7\text{O}_{13}\text{I}$ and other nickel iodine boracites, among which are the first compounds found to be multiferroics in 1960s, show ferroelectricity due to the large number of inter-ionic interactions. Manganites RMnO_3 (R = Sc, Y, Dy, Ho, Er, Tm, Yb, Lu) are also well known single phase multiferroic materials. In hexagonal manganites, long-range dipole–dipole interactions and oxygen rotations lead to ferroelectricity and these materials also exhibit antiferromagnetism [33,34].

It is not easy for both ferroelectricity and ferromagnetism (or antiferromagnetism) to coexist in one material. If they do coexist, they tend to be very weakly coupled and have very low Néel

temperatures or Curie temperatures. Thus, single phase multiferroicity tends to exist only at low temperatures.

There are some well-known exceptions, however. BiFeO_3 is a single phase multiferroic material with a ferroelectric Curie temperature of 1143 K and a Néel temperature of 653 K [35]. It is a multiferroic material at room temperature and it is the most intensely studied single phase multiferroic material. The crystal structure of BiFeO_3 is a rhombohedrally distorted perovskite structure with the space group $R3c$ (see Fig. 1.2). With this structure, the spontaneous ferroelectric polarization can be in any of the eight diagonal $[111]$ directions.

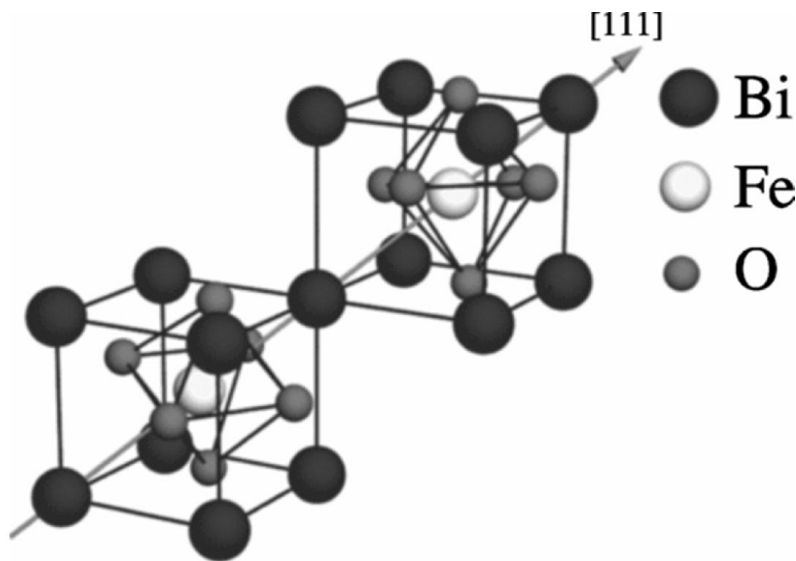


Fig. 1.2 $R3c$ structure of BiFeO_3 . Two cubic perovskite unit cells are shown. The cations are displaced along the $[111]$ direction relative to the anions, and oxygen octahedra rotate around the $[111]$ axis. From Ref. [36].

The magnetic properties of BiFeO_3 arise from the Fe^{3+} cations, which form a so-called G-type antiferromagnetic structure (see Fig. 1.3). The Fe cations are slightly twisted by the oxygen atoms through an antisymmetric spin-orbit coupling. Thus a weak ferromagnetism is present in

BiFeO₃ along with ferroelectricity. The interaction that gives rise to the weak ferromagnetism is called the Dzyaloshinskii-Moriya (DM) interaction [37,38]. Because of the DM interaction, the ferroelectricity and weak ferromagnetism of BiFeO₃ are coupled. This interaction allows tuning of the magnetic order in BiFeO₃ through application of an electric field and makes BiFeO₃ one of the most attractive materials for pursuing electric-field controlled magnetic devices [29,31,39].

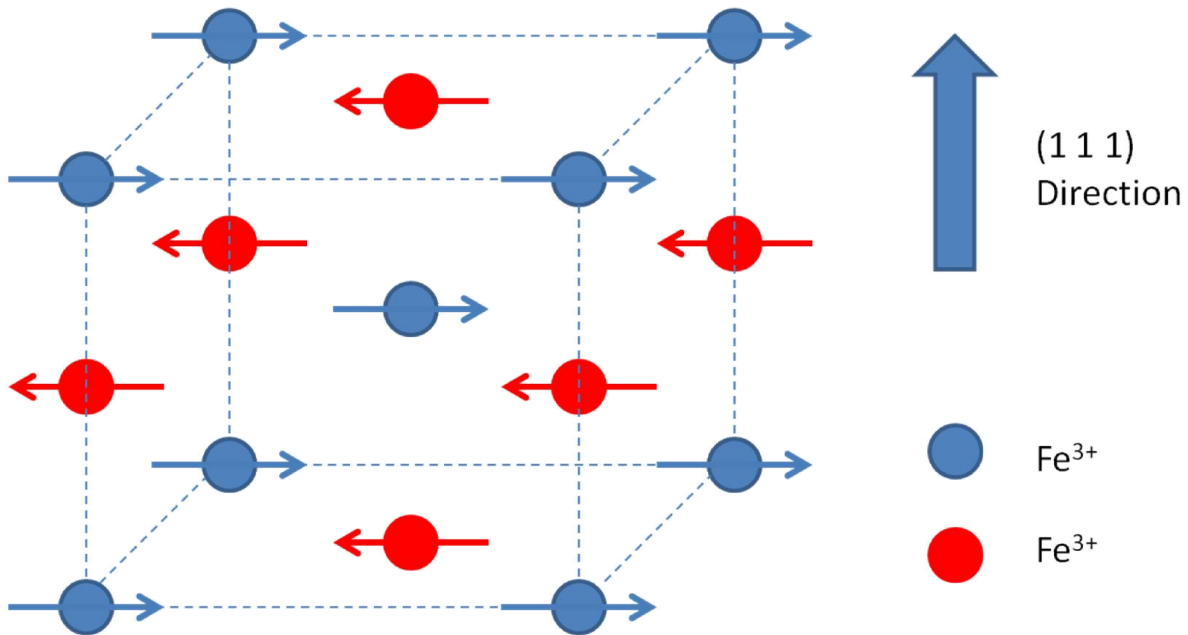


Fig. 1.3 Schematic view of G-type antiferromagnetic structure of BiFeO₃. Alternating Fe³⁺ ions have spins pointing in opposite directions.

1.3.2 Composite Multiferroics

Because single phase multiferroic materials are relatively rare and their multiferroic couplings are generally weak, many researchers have turned to composites combine of piezoelectric and magnetostrictive materials. Individually, neither the piezoelectric or magnetostrictive materials are multiferroic. However, when combined together, the mechanical

interaction between the two can enable magnetoelectric coupling. As a magnetic or electric field is applied to a composite material, strain can be induced in the magnetostrictive or piezoelectric phase. Because the two phases are mechanically coupled, stress induced in one leads to a transduced signal in the other. Both the magnetoelectric (ME) effect and the converse ME effect can be thought as being the resulting product of magnetostrictive effect and piezoelectric effect

$$\text{ME effect} = \frac{\text{electric}}{\text{mechanical}} \times \frac{\text{mechanical}}{\text{magnetic}}, \quad (1.1)$$

$$\text{converse ME effect} = \frac{\text{magnetic}}{\text{mechanical}} \times \frac{\text{mechanical}}{\text{electric}}, \quad (1.2)$$

Researchers use the ME coefficient α to define the strength of the magnetoelectric coupling.

$$\alpha = \frac{\partial E}{\partial H}, \quad (1.3)$$

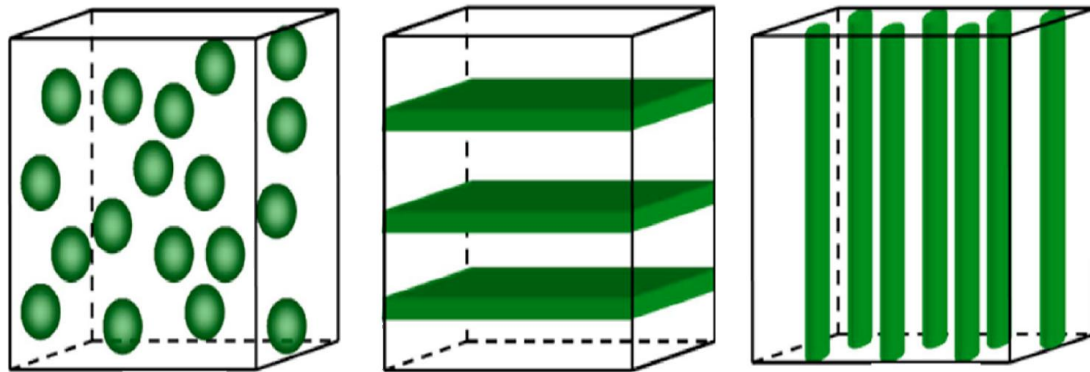
The stronger the electric field that is induced per unit magnetic field, the stronger the ME coupling α is.

Many composite materials exhibit magnetoelectric coefficients that are orders of magnitude higher (see Table 1.1) than those of single phase multiferroics ($\alpha = 20 \text{ mV}/(\text{cm} \times \text{Oe})$ for Cr_2O_3 [13]) and many of them can work at room temperature. A composite also allows some freedom to choose from a wide range of piezoelectric materials and magnetostrictive materials.

It is important to note that it is the piezoelectricity in the ferroelectric phase which leads to the ME coupling. All ferroelectric materials are piezoelectric, but not all piezoelectric materials are ferroelectric. In composite ME effects, all that is needed is a piezoelectric strain. For example, AlN, a non-ferroelectric piezoelectric material with piezoelectric coefficient $d_{31} = -1.98 \text{ pC/N}$ [40], was recently found to be very effective in ME coupling [24].

There are a variety of geometrical ways in which one can combine piezoelectric and magnetostrictive phases. Newnham *et al.* introduced the concept of phase connectivity to classify

different composite schemes [41]. The most commonly studied schemes are the 0-3 particulate composites, the 2-2 laminate composites, and the 1-3 fiber composites (see Fig. 1.4). Usually the first number indicates the dimension of the ferromagnetic (magnetostrictive) phase, while the second number indicates the dimension of the ferroelectric phase.



0-3 particulate composite

2-2 laminate composite

1-3 fiber/rod composite.

Fig. 1.4 Three types of magnetoelectric composite schemes. They are defined according to the phase connectivity. The ferroelectric (piezoelectric) phase is indicated in green. From Ref. [2].

The 0-3 particulate composite materials were studied as early as in the 1970s, when directional solidification from a eutectic melt or sintering method was used to grow $\text{BaTiO}_3/\text{CoFe}_2\text{O}_4$ composites [42,43]. Their ME coefficient reached as high as $130 \text{ mV}/(\text{cm} \times \text{Oe})$ at room temperature. Sintering is an easier and cheaper method than directional solidification, and it is used to make various composites. However, sintering has the problem that it can lead to phase and element diffusion across interfaces, leading to current leakage in piezoelectric

Table 1.1 Summary of some ME bulk composites and their ME coefficients. CFO: CoFe_2O_4 , BTO: BaTiO_3 , NZFO: $\text{Ni}_{0.8}\text{Zn}_{0.2}\text{Fe}_2\text{O}_4$, PZT: $\text{Pb}(\text{Zr}_{0.52}\text{Ti}_{0.48})\text{O}_3$, NCZF: $\text{Ni}_{0.6}\text{Cu}_{0.2}\text{Zn}_{0.2}\text{Fe}_2\text{O}_4$, Terfenol-D: $\text{Tb}_x\text{Dy}_{1-x}\text{Fe}_2$, $x \sim 0.3$, PMN-PT: $\text{Pb}(\text{Mg,Nb})\text{O}_3\text{-PbTiO}_3$, PVDF: polyvinylidene-fluoride $(-\text{C}_2\text{H}_2\text{F}_2)_n$, P(VDF-TrFE): poly(vinylidene fluoride $(\text{C}_2\text{H}_2\text{F}_2)$ -trifluoroethylene $(\text{CF}_2=\text{CFH})$). From Ref. [47]

ME Composite	ME Coefficient ($\text{mV cm}^{-1} \text{Oe}^{-1}$)	Ref.
Ceramic Composites:		
(0-3) CFO/BTO	50 @ f_r	[48]
(0-3) NZFO/PZT	155 @ 1 kHz	[49]
(2-2) NCZF/PZT/NCZF	782 @ 1 kHz	[50]
Ceramic Alloy Composites:		
(2-2) Terfenol-D/PMT-PT	10.3×10^3 @ 1k Hz	[51]
(2-2) Terfenol-D/PVDF	1.43×10^3	[52]
(2-1) FeBSiC/PZT-fiber	22×10^3 @ 1 Hz and 750×10^3 @ f_r	[53,54]
(2-2) FeBSiC/PVDF	21.46×10^3 @ 20 Hz	[55]
(2-2) FeCoSiB/AlN	3.1×10^3 @ 1 Hz and 737×10^3 @ f_r	[24]
Polymer-Based Composites		
(2-2) PZT in PVDF/Terfenol-D in PVDF	80 @ 1 kHz and 3×10^3 @ f_r	[56]
(1-3) Terfenol-D in epoxy/PZT	500 @ 100 Hz and 18.2×10^3 @ f_r	[57]
(0-3) CFO/P(VDF-TrFE)	40 @ 5 kHz	[58]

materials. The 0-3 particulate composite and the 1-3 fiber composite are usually more difficult to make compared to 2-2 laminate composites.

Since the time the first multiferroic composites were synthesized in the 1970s, many more composites have been developed with a variety of configurations and materials. High ME coefficients are desired, because with higher ME coefficients, the ME devices will be more effective in applications such as magnetic field sensors, actuators, energy harvesters, and transducers. Researchers have mostly worked on 2-2 laminate structures since 1990s because laminate structures have typically shown higher ME coefficients than other forms. Bulk laminate magnetolectric materials that feature a piezoelectric $\text{Pb}(\text{Zr}_x\text{Ti}_{1-x})\text{O}_3$ (PZT) layer and a magnetostrictive ferrite layer glued together with conductive epoxy have shown the ME coefficient of up to 270 mV/(cm × Oe), as reported by Srinivasan *et al.* [44]. They also made periodically alternating piezoelectric and magnetostrictive layers and reported ME coefficients of 1.5 V/(cm × Oe) [45]. In 2001, Ryu reported a ME coefficient of 4.68 V/(cm × Oe) by stacking and bonding PZT and Terfenol-D disks [46]. This work was a milestone because of the large ME coefficient. Until recently, the ME coefficient was considered very large if it exceeded over 1 V/(cm × Oe).

Table 1.1 shows a summary of some ME bulk composites and their ME coefficients reported to date. The Table shows that the 2-2 laminate ceramic/alloy combinations have much higher ME coefficients than the other types of composites. The highest ME coefficient in Table 1.1 is 750 V/(cm × Oe) from a device made of Metglas (FeBSiC) and PZT-fiber. This device was measured at the mechanical resonant frequency to boost the ME coefficient significantly from 22 V/(cm × Oe) at off resonance to 750 V/(cm × Oe) at the resonance [53]. In fact, Quandt, *et al.* in

2013 showed they were able to measure the ME coefficient of $20 \text{ kV}/(\text{cm} \times \text{Oe})$ with FeBSiC/AlN at the resonant frequency of 152 Hz [16].

PZT has one of the highest piezoelectric coefficients among known piezoelectric materials, while Terfenol-D ($\text{Tb}_x\text{Dy}_{1-x}\text{Fe}_2$, $x \sim 0.3$) exhibits the highest magnetostrictive coefficient of all known magnetostrictive materials. This is the reason why these are often used in composites. However, PZT has lead which is not desirable for widespread applications, while Terfenol-D is so brittle it may not be useful in many circumstances. Terfenol-D is also very expensive. Popular alternatives for PZT are AlN and PVDF, which is a polymer with formula of $-(\text{C}_2\text{H}_2\text{F}_2)_n-$. PVDF and AlN can be used in biomedical applications because they are lead free. AlN, with its low dielectric constant ($\epsilon_r = 9$ [40]), can outperform PZT ($\epsilon_r = 900$ [59]) in magnetoelectric coupling [24], even though it has a much lower piezoelectric coefficient ($d_{31} = -1.98 \text{ pC/N}$ [40]) than PZT ($d_{31} = 120 \text{ pC/N}$ [59]). This is because it is the ratio of the piezoelectric coefficient to the dielectric constant that determines contribution to the ME coefficient from the piezoelectric material.

Other promising magnetostrictive materials are Permendur (FeCoV), Metglas ($(\text{Fe}_{90}\text{Co}_{10})_{78}\text{Si}_{12}\text{B}_{10}$), and FeGa. A recent study shows that formation of certain nanostructures can lead to the occurrence of heterogeneous magnetostriction of FeCo. The magnetostriction λ in FeCo can be doubled by quenching after sputtering [20]. Metglas does not have a high magnetostriction ($\lambda = 42 \text{ ppm}$ [60]). However, its relative permeability is as high as 10^6 . This suggests Metglas could form an extremely sensitive material for magnetic field sensors using the ME effect. FeGa, also called Galfenol, when Fe content is 80% or 70%, shows large saturation magnetostriction near 180 ppm for thin film structures and 400 ppm for bulk structures [19].

1.4 Chapter Descriptions

The main purpose of my thesis was to characterize a new type of microfabricated FeGa/PZT multiferroic cantilever device and to investigate and demonstrate potential applications of these devices. These devices have the “2-2” laminate composite configuration. The cantilevers were fabricated by my co-worker Dr. Tiberiu-Dan Onuta in my advisor Professor Ichiro Takeuchi’s group, in the Department of Materials Science and Engineering at the University of Maryland.

This thesis consists of six Chapters, starting with the introduction to multiferroic materials and structures in Chapter 1.

In Chapter 2 I elaborate on the general theory of multiferroic materials, and provide background regarding magnetoelectric (ME) devices including their basic characterization and application for magnetic field sensors. The reasons of choosing PZT and FeGa as functional materials in our magnetoelectric devices will be discussed. We will also present the basic characteristics of large ($4.5 \text{ mm} \times 20 \text{ mm} \times 30 \text{ }\mu\text{m}$) multiferroic cantilevers, such as the “butterfly” curve (the ME coefficient as a function of the DC bias magnetic field) and factors that affect the magnetoelectric coefficients of those cantilevers.

Chapter 3 discusses the basic characteristics of microfabricated small ($0.95 \text{ mm} \times 0.2 \text{ mm} \times 5 \text{ }\mu\text{m}$) multiferroic cantilevers and their applications in energy harvesting. A different “butterfly” curve where the resonant frequency shifts with the DC magnetic field is found. A magnetic cantilever theory developed by S. E. Lofland will be used to explain this behavior. Thus, why the small device has a different “butterfly” curve will be pointed out.

Chapter 4 investigates the nonlinear behavior of the cantilevers and its application as multimode memories based on bistability of the nonlinear mechanical vibration amplitude near the resonant frequency. We will show that our devices are Duffing oscillators. Because of the

multiferroic structure, we are able to use a few switching parameters, such as the driving frequency, the driving amplitude, the DC magnetic field, and the DC electric field, as the trigger to switch our memory devices.

Chapter 5 shows how parametric amplification can be used on multiferroic cantilevers to significantly enhance the ME coefficient, quality factor, and the sensitivity of the ME device. We will introduce how the parametric amplification can lead to a phase sensitive gain and how the gain will diverge as the pump voltage approaches the threshold.

Chapter 6 summarizes this thesis work and discusses possible future directions.

Chapter 2: Multiferroic Materials and the Magnetoelectric Coupling

2.1 Introduction

In this Chapter, basics of multiferroic materials and cantilever devices are presented. Our device is made of two functional materials, piezoelectric PZT and magnetostrictive FeGa. First, I will introduce the concept of piezoelectricity, ferroelectricity, and PZT. Then, properties of ferromagnetism, magnetostriction, and FeGa will be described. The coupling between the two types of materials, the magnetoelectric coupling will then be presented. Finally, our previous generation of device, a $4.5 \text{ mm} \times 20 \text{ mm} \times 30 \text{ }\mu\text{m}$ FeGa/PZT multiferroic cantilever that was studied by Peng, will be discussed.

2.2 Piezoelectricity and Ferroelectricity

2.2.1 Piezoelectricity

Piezoelectricity, first discovered by Jacques and Pierre Curie in 1880, is the effect that electric charges build up in certain solid materials when mechanical stress is applied. These materials are called piezoelectric materials. The name ‘piezo’ is derived from Greek, meaning to squeeze or press. Because of their ability to transfer mechanical deformation to electric signals, piezoelectric materials are widely used for applications in mechanical sensors, such as microphones [61,62] and ultrasonic wave detectors [63]. Because the piezoelectric effect generates electricity, it has been used for high voltage power sources [64] and energy harvesters [65].

Piezoelectric materials can convert mechanical energy into electric energy, and they can also transfer electric charges into a mechanical displacement. The latter is called the converse piezoelectric effect. With the ability to make mechanical vibration or displacement according to an electric signal, piezoelectric materials have been widely used in applications such as speakers, piezoelectric motors, and quartz clocks [66,67].

Piezoelectricity requires materials to have non-centrosymmetric structures. It is the microscopic asymmetry in crystal structures that induces macroscopic asymmetric charge densities appearing at the surfaces. In this chapter, we will discuss how the crystal structure change is translated into piezoelectricity for PZT.

For now, let us look at the piezoelectric effect mathematically. Normally, without piezoelectricity, dielectric materials display a dielectric response given by

$$\mathbf{D} = \xi \mathbf{E} \quad (2.1)$$

and a mechanical response given by the Hooke's law

$$\boldsymbol{\varepsilon} = \mathbf{S} \boldsymbol{\sigma} \quad (2.2)$$

, where \mathbf{D} is vector of dielectric displacement (C/m^2), ξ is permittivity of the material (F/m), \mathbf{E} is applied electric field (V/m), $\boldsymbol{\varepsilon}$ is strain vector (m/m), \mathbf{S} is compliance coefficient (m^2/N), and $\boldsymbol{\sigma}$ is stress vector (N/m^2).

As one can see, the dielectric response and the mechanical response are well separated.

However, for a piezoelectric material, the two properties are coupled. If we take into account that stress and strain are 2nd rank tensors, the coupled equations become

$$\varepsilon_{ij} = \sum_{kl} S_{ijkl} \sigma_{kl} + \sum_k d_{kij} E_k \quad (2.3)$$

$$D_i = \sum_{jk} d_{ijk} \sigma_{jk} + \sum_j \xi_{ij} E_j \quad (2.4)$$

, where D is vector of dielectric displacement (C/m^2), ξ is permittivity of the material (F/m), E is applied electric field (V/m), ε is strain vector (m/m), S is compliance coefficient (m^2/N , 4th rank tensor), σ is stress vector (N/m^2), d is piezoelectric strain constant (3rd rank tensor), and i, j, k, l can be 1, 2, 3 (space coordinate index)

Considering the solid system we usually deal with in piezoelectric materials, due to conservation of angular momentum, the stress tensor should be symmetric, and thus $\sigma_{ij} = \sigma_{ji}$. This is the Cauchy's second law of motion. As a result, the stress tensor matrix only has 6 independent elements, which are $\sigma_{11}, \sigma_{22}, \sigma_{33}, \sigma_{23}, \sigma_{13}, \sigma_{12}$. If we re-label them as $\sigma_1, \sigma_2, \sigma_3, \sigma_4, \sigma_5, \sigma_6$, we can reshape the 3 by 3 stress matrix into a 6 by 1 matrix, thus the coupled Eq. (2.3) and Eq. (2.4) can be rewritten into matrix form of

$$\begin{bmatrix} \varepsilon_1 \\ \varepsilon_2 \\ \varepsilon_3 \\ \varepsilon_4 \\ \varepsilon_5 \\ \varepsilon_6 \end{bmatrix} = \begin{bmatrix} S_{11} & S_{12} & S_{13} & S_{14} & S_{15} & S_{16} \\ S_{21} & S_{22} & S_{23} & S_{24} & S_{25} & S_{26} \\ S_{31} & S_{32} & S_{33} & S_{34} & S_{35} & S_{36} \\ S_{41} & S_{42} & S_{43} & S_{44} & S_{45} & S_{46} \\ S_{51} & S_{52} & S_{53} & S_{54} & S_{55} & S_{56} \\ S_{61} & S_{62} & S_{63} & S_{64} & S_{65} & S_{66} \end{bmatrix} \begin{bmatrix} \sigma_1 \\ \sigma_2 \\ \sigma_3 \\ \sigma_4 \\ \sigma_5 \\ \sigma_6 \end{bmatrix} + \begin{bmatrix} d_{11} & d_{21} & d_{31} \\ d_{12} & d_{22} & d_{32} \\ d_{13} & d_{23} & d_{33} \\ d_{14} & d_{24} & d_{34} \\ d_{15} & d_{25} & d_{35} \\ d_{16} & d_{26} & d_{36} \end{bmatrix} \begin{bmatrix} E_1 \\ E_2 \\ E_3 \end{bmatrix} \quad (2.5)$$

$$\begin{bmatrix} D_1 \\ D_2 \\ D_3 \end{bmatrix} = \begin{bmatrix} d_{11} & d_{12} & d_{13} & d_{14} & d_{15} & d_{16} \\ d_{21} & d_{22} & d_{23} & d_{24} & d_{25} & d_{26} \\ d_{31} & d_{32} & d_{33} & d_{34} & d_{35} & d_{36} \end{bmatrix} \begin{bmatrix} \sigma_1 \\ \sigma_2 \\ \sigma_3 \\ \sigma_4 \\ \sigma_5 \\ \sigma_6 \end{bmatrix} + \begin{bmatrix} \xi_{11} & \xi_{12} & \xi_{13} \\ \xi_{21} & \xi_{22} & \xi_{23} \\ \xi_{31} & \xi_{32} & \xi_{33} \end{bmatrix} \begin{bmatrix} E_1 \\ E_2 \\ E_3 \end{bmatrix} \quad (2.6)$$

For crystals with space group $4mm$ (to which PZT belongs) and $6mm$, and considering more symmetry conditions of these materials, many of the coefficients in the above matrices will be either zero, or can be expressed in terms of other coefficients. The non-zero coefficients are:

$$S_{11} = S_{22} \quad (2.7)$$

$$S_{13} = S_{31} = S_{23} = S_{32} \quad (2.8)$$

$$S_{12} = S_{21} \quad (2.9)$$

$$S_{44} = S_{55} \quad (2.10)$$

$$S_{66} = 2(S_{11} - S_{12}) \quad (2.11)$$

$$d_{31} = d_{32} \quad (2.12)$$

$$d_{15} = d_{24} \quad (2.13)$$

$$\xi_{11} = \xi_{22} \quad (2.14)$$

$$\xi_{33} \quad (2.15)$$

Then the coupled equations become

$$\begin{bmatrix} \varepsilon_1 \\ \varepsilon_2 \\ \varepsilon_3 \\ \varepsilon_4 \\ \varepsilon_5 \\ \varepsilon_6 \end{bmatrix} = \begin{bmatrix} S_{11} & S_{12} & S_{13} & 0 & 0 & 0 \\ S_{21} & S_{11} & S_{23} & 0 & 0 & 0 \\ S_{31} & S_{32} & S_{33} & 0 & 0 & 0 \\ 0 & 0 & 0 & S_{44} & 0 & 0 \\ 0 & 0 & 0 & 0 & S_{44} & 0 \\ 0 & 0 & 0 & 0 & 0 & 2(S_{11} - S_{12}) \end{bmatrix} \begin{bmatrix} \sigma_1 \\ \sigma_2 \\ \sigma_3 \\ \sigma_4 \\ \sigma_5 \\ \sigma_6 \end{bmatrix} + \begin{bmatrix} 0 & 0 & d_{31} \\ 0 & 0 & d_{31} \\ 0 & 0 & d_{33} \\ 0 & d_{15} & 0 \\ d_{15} & 0 & 0 \\ 0 & 0 & 0 \end{bmatrix} \begin{bmatrix} E_1 \\ E_2 \\ E_3 \end{bmatrix} \quad (2.7)$$

$$\begin{bmatrix} D_1 \\ D_2 \\ D_3 \end{bmatrix} = \begin{bmatrix} 0 & 0 & 0 & 0 & d_{15} & 0 \\ 0 & 0 & 0 & d_{15} & 0 & 0 \\ d_{31} & d_{31} & d_{33} & 0 & 0 & 0 \end{bmatrix} \begin{bmatrix} \sigma_1 \\ \sigma_2 \\ \sigma_3 \\ \sigma_4 \\ \sigma_5 \\ \sigma_6 \end{bmatrix} + \begin{bmatrix} \xi_{11} & 0 & 0 \\ 0 & \xi_{11} & 0 \\ 0 & 0 & \xi_{33} \end{bmatrix} \begin{bmatrix} E_1 \\ E_2 \\ E_3 \end{bmatrix} \quad (2.8)$$

In the piezoelectric coefficient matrix d_{ij} , the d_{31} and d_{33} are the most frequently mentioned coefficients. Referring to Fig. 2.1, d_{31} and d_{33} are the coefficients which indicate how strong the piezoelectric response is in Direction 3, when normal stress is applied in Direction 1 and Direction 3, respectively (Fig. 2.1). AlN has a d_{31} of 1.98 pC/N [40]. For PZT grown by the sol-gel method, d_{31} is nearly 120 pC/N [59]. D_{33} s of them are usually 2-2.5 times as large as their d_{31} s [68].

In the case for thin films, d_{31} is mostly used, since electric charges are usually collected in the normal direction of the film while stress is applied along the film in-plane direction.

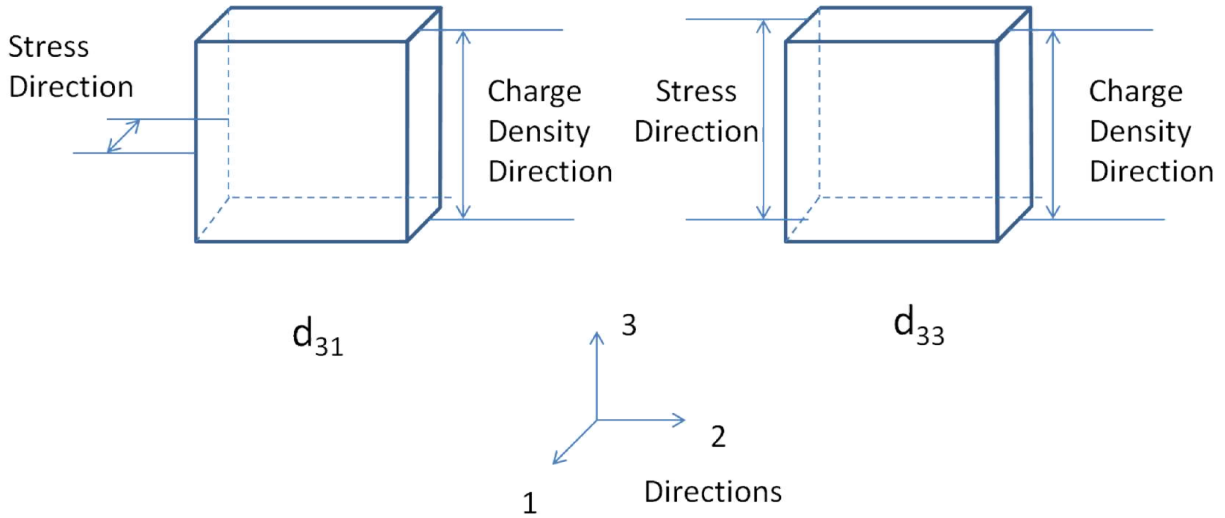


Fig. 2.1 d_{31} and d_{33} are the charge densities induced in Direction 3 in response to applied stress in different directions.

For \mathbf{d} matrix for PVDF, a polymer with chemical formula of $-(C_2H_2F_2)_n^-$, though should be modified to

$$\begin{bmatrix} 0 & 0 & d_{31} \\ 0 & 0 & d_{32} \\ 0 & 0 & d_{33} \\ 0 & d_{24} & 0 \\ d_{15} & 0 & 0 \\ 0 & 0 & 0 \end{bmatrix}$$

, which reflects the nonisotropic piezoelectric property in Directions 1 and 2. d_{31} of PVDF is 20 pC/N [69].

2.2.2 Ferroelectricity

Ferroelectricity is the phenomenon that materials show spontaneous stable electric polarization which is switchable under electric field (Fig. 2.2a). Such switchable polarization makes ferroelectric materials good materials for memory device elements. The fact that the polarization is stable without supplying an electric field makes them non-volatile memories. The electric field affects the materials through increasing, decreasing, or rotating the electric dipoles in the materials.

Ferroelectric materials are known to be also pyroelectric, as charges would be induced when heated or cooled. This is because that the lattice constants change as the temperature changes. In fact, as temperature goes up, the crystal structure of ferroelectric materials gains inversion symmetry at some point, and the materials become paraelectric. This transition temperature is called the Curie temperature, T_c . Paraelectric materials have no spontaneous polarization (Fig. 2.2b).

Fig. 2.2a is a typical hysteresis loop of a ferroelectric material. As the figure shows, for a ferroelectric material, the polarization as a function of electric field has two possible output states. If the material starts from the maximum positive electric field at point **a**, it has a positive saturation polarization P_s , in which case all the electric dipoles are aligned and maximized in positive field direction. As the electric field is decreased from maximum field at point **a** to zero field at point **b**, the dipoles in the positive direction decrease while the dipoles in the opposite direction increase, and the polarization decreases to remnant polarization P_r , which is still above zero for ferroelectric materials. This is what is needed for the non-volatile memory where a polarization is maintained even when the electric field is turned off. As we continue to increase the electric field in the other direction until it reached $-E_c$, the material undergoes curve from

point **b** to point **c**, where the positive dipoles cancel with the negative dipoles completely so that the net polarization is zero. The electric field at point **c** is called the coercive field, which one can see as the field that the material needs to overcome to neutralize the polarization. Then, as we further increase the electric field in the negative direction until saturation field, the polarization reaches negative saturation polarization, where only negative dipoles exist. Now if one decides to decrease the negative electric field to zero and then increase the positive field to saturation, the material will follow the lower curve from point **d** through point **e** and **f** back to point **a**, which is a similar process compared to the upper curve except that everything now is with an opposite sign.

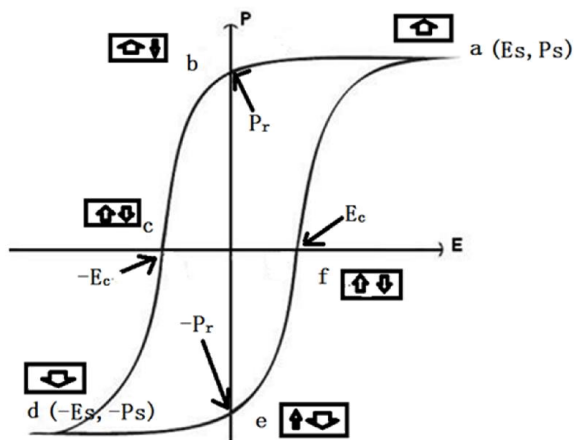


Fig.2.2a Ferroelectric P-E Hysteresis

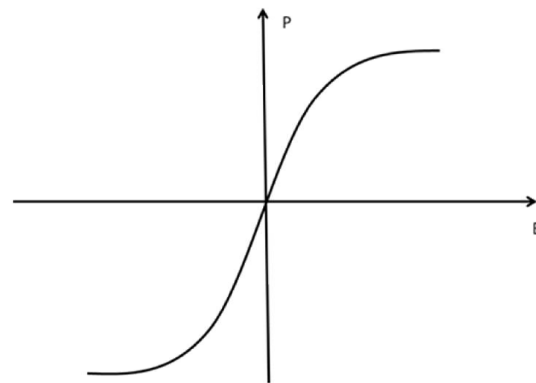


Fig. 2.2b Paraelectric P-E Curve

E_s is the saturation electric field (V/m), E_c is the electric coercive field (V/m), P_s is saturation polarization (C/m^2) and P_r is remnant polarization (C/m^2).

Ferroelectric materials are all piezoelectric, but not all the piezoelectric materials are ferroelectric. For example, quartz and AlN do not have any spontaneous polarizations without

electric field applied. However, PZT, the material that we are using in this thesis, is both piezoelectric and ferroelectric.

2.2.3 The Perovskite Structures

It is usually the case that the microstructure defines macroscopic properties of a material. We have mentioned that the piezoelectricity and ferroelectricity both come from the non-centrosymmetric structures. To be more specific, crystal structure of PZT belongs to the perovskite structure.

The name of perovskite was originally given to calcium titanium oxide, which has the chemical formula CaTiO_3 . The general chemical formula for perovskite oxide structures is ABO_3 , where 'A' and 'B' are different atoms. In an ideal cubic perovskite oxide unit-cell in Fig. 2.3 (a), there are eight 'A' atoms sitting at the eight corners, one 'B' atom sitting at the center of the cubic, and six oxygen atoms sitting at the face centers of the cubic. Each 'A' atom is shared by eight neighbored unit cells while each oxygen atom is shared by two neighbored unit cells. This makes one unit cell ABO_3 .

In a cubic structure (Fig. 2.3 (a)), the unit cell is centrosymmetric, thus the material will have no piezoelectricity or ferroelectricity. On the contrary, in the tetragonal structure (Fig. 2.3 (b)), charge centers of the positive charges and negative charges no longer overlap, and thus there is a spontaneous electric dipole moment in the unit cell. This dipole can be further increased or decreased under electric field, depending on the direction of the field. As a result, the electric polarization and surface charges will also be changed. When stress is applied on the material, the unit cell will respond in such a way so that there is a charge density change, too. In summary, the

asymmetric unit cell is the key to both ferroelectricity and piezoelectricity for insulating perovskite crystals.

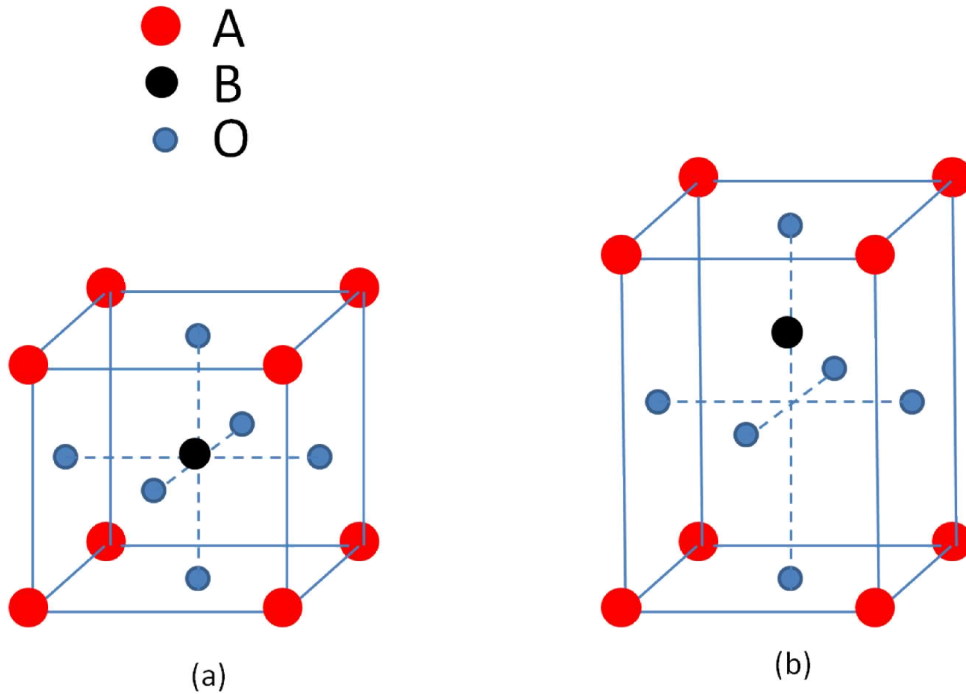


Fig. 2.3 (a) is a cubic phase perovskite, while (b) is a tetragonal perovskite

Ferroelectricity is only observed when the material is below its Curie temperature. In perovskite oxide, they are in the cubic phase above T_c . Below T_c , they are in a tetragonal or a lower symmetry structure.

2.2.4 Lead Zirconate Titanate (PZT)

PZT, which has the chemical formula of $\text{Pb}(\text{Zr}_x\text{Ti}_{1-x})\text{O}_3$ for $0 \leq x \leq 1$, is a perovskite. In its unit cell, Pb atoms sit in the 'A' site, while Zr and Ti atoms sit in 'B' site. There are $x \times 100\%$ of the 'B' site occupied by Zr atoms whereas $(1-x) \times 100\%$ Ti atoms.

Depending on the doping concentration, PZT has the dielectric constant at room temperature ranging from 300 to 3850 [70,71], which makes it a very good material for capacitors. It is also frequently used for ultrasound transducers, sensors, and actuators due to its high piezoelectricity (up to 290 pC/N at room temperature) [70,71]. Its ferroelectricity makes it useful in ferroelectric RAM (random-access memory) devices [72,73], which have the advantages of lower power consumption, faster write performance, and longer write-erase cycles compared to traditional RAMs.

For making devices for this thesis work, we want the piezoelectric coefficient d_{31} to be as high as possible, thus Zr concentration of $x=0.52$ is chosen. This is near the so called morphotropic phase boundary (MPB), where the piezoelectric coefficient is significantly increased due to the increased number of allowable domain states. The d_{31} of our PZT thin film grown by sol-gel method is 120 pC/N after poling by electric field of 20 MV/m for 2 to 3 minutes. This is also a regime where the tetragonal phase and the rhombohedral phase can coexist. T_c for this Zr content is between 330 °C to 350 °C.

2.3 Magnetism and Magnetostriction

2.3.1 Diamagnetism, Paramagnetism, and Ferromagnetism

In classical physics, the only entities that can interact with magnetic field are moving charges. In an atom, there are electrons orbiting around the nucleus which are moving charges. However, quantum mechanics dictates there are spins, too. The spin of electrons and the orbital angular momentum combines the total magnetic dipole moments for the atoms. Under magnetic field, the orbital dipole moment will precess around the direction of magnetic field because of the torque that is perpendicular to the magnetic moment, while the spin would align with the magnetic field

to minimize magnetic energy. The precessing orbital dipole moment is equivalently adding a magnetic moment opposing the applied magnetic field, thus reducing the total local magnetic field. This is the phenomenon of diamagnetism. The spin that aligns with applied magnetic field will enhance the total local magnetic field. For some materials with no unpaired electrons such as water, carbon, copper, and silver, the enhancement of local magnetic field from spin is not enough to compensate the opposite precessing moment. They are diamagnetic materials, which create small magnetic field opposing the applied magnetic field. Paramagnetic materials are those which will create magnetic field in the same direction of the applied field. However, the created magnetic field will vanish if the external field is taken off. When it is below a certain temperature, some paramagnetic materials will transform into ferromagnetic materials developing a spontaneous magnetization (magnetic moment per volume) without applied field. This is when the magnetic energy outperforms the thermal vibration below this particular temperature, called the Curie temperature. (This is similar to the case of ferroelectricity.) Not only are the magnetizations spontaneous, ferromagnetic materials also have much stronger magnetizations than paramagnetic materials under magnetic field. More general information can be found in Chapter 1 of Ref. [74].

In an unmagnetized ferromagnetic material, there are many small magnetic domains which are groups of local magnetizations aligned in the same direction. These domains are randomly oriented to minimize the total magnetic energy. When an external magnetic field is applied up to saturation field, all the magnetic domains will align with the magnetic field, as at the point **a** in Fig. 2.4. There is a hysteresis in plot of magnetization (M) vs magnetic field (H). On this M - H plot, the coordinates (H , M) of a ferromagnetic material follow the upper curve $a \rightarrow b \rightarrow c \rightarrow d$ when the external magnetic field decreases from H_s to $-H_s$. On the contrary, when the external

magnetic field increases from $-H_s$ to H_s , the coordinates follow the lower curve $d \rightarrow e \rightarrow f \rightarrow a$. This is similar to the case of ferroelectric materials, which we have discussed in Section 2.2.2. M_s is the saturation magnetization the material would reach when the external magnetic field is H_s . M_r is the remnant magnetization that the material will maintain when the magnetic field is reduced from H_s to zero. H_c is the coercive field that is needed in the opposite direction to bring the magnetization from M_r to zero.

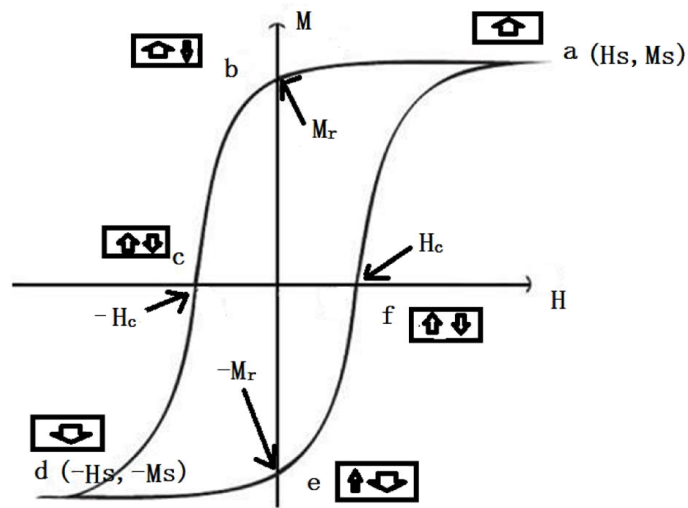


Fig. 2.4 Magnetization vs Magnetic field (M-H Loop). H_s is saturation applied magnetic field (Oe), H_c is magnetic coercive field (Oe), M_s is saturation magnetization (emu/cm^3), and M_r is remnant magnetization (emu/cm^3)

2.3.2 Magnetostriction

In this section, we will have a short discussion about magnetostriction. Detailed information can be found in the Chapter 13 of Ref. [74]. Magnetostriction is a property of ferromagnetic materials that they will change their shape when they are magnetized. The effect was first discovered by Jame Joule when studying a sample of iron in 1842.

There are two types of magnetostriction. One is called spontaneous magnetostriction, which is caused by ordering of the magnetic moment as domains are formed at the Curie temperature. The other is the magnetic-field-induced magnetostriction, when domains are reoriented by an external magnetic field. In both situations, magnetostriction strain is defined as λ , the fractional change in a dimension of the material.

$$\lambda = \Delta l / l \quad (2.9)$$

This value can be either positive or negative depending on if the materials expand or shrink when magnetized. Usually when magnetostriction coefficient is discussed, it is just the magnetic-field-induced magnetostriction coefficient.

The origin of magnetostriction is the spin-orbit coupling effect. As we know from quantum mechanics, magnetic moments come from two sources that are the spin of the electrons and orbital angular momentum of electrons. Both the spin angular momentum and the orbital angular momentum will respond to the external magnetic field. The two also interact with each other, because they are both actually affected by the magnetic field from each other.

Then, why we need spin-orbit coupling to generate magnetostriction? In a spin magnetization rich ferromagnetic material, when an external magnetic field is applied, the spins will be aligned in the magnetic field direction. Then because of the spin-orbit coupling, the orbits of electrons are affected. The orbit of the electrons is essentially determined by the detailed chemical bonds and lattice constants. Thus, applying a magnetic field induces the strain in ferromagnetic materials.

Strictly speaking, magnetostriction exists in all materials due to the orbital magnetization. However, magnetostriction in ferromagnetic materials (or at least ferrimagnetic materials) is

orders of magnitude higher than those of non-magnetic materials, which have no spin magnetizations.

2.3.3 Iron Gallium (FeGa)

The iron gallium alloy ($\text{Fe}_{1-x}\text{Ga}_x$) thin film is the material that is used in this thesis. It has peaks in magnetostriction when the Ga content is about 20% or 30% in the case of both thin film and bulk materials [19]. The thin film $\text{Fe}_{0.8}\text{Ga}_{0.2}$ and bulk $\text{Fe}_{0.8}\text{Ga}_{0.2}$ have magnetostriction of 160 ppm and 400 ppm respectively. In thin film $\text{Fe}_{0.7}\text{Ga}_{0.3}$, the magnetostriction is about 180 ppm compared to 400 ppm in bulk. The magnetostrictions for the thin films are less than half of those of bulk materials. This is because of the residual strain from deposition and the fact that we only applied magnetic field in parallel direction and assume perpendicular deflection being zero. There are several reasons that this material is selected for our magnetostrictive phase. First, our group has the ability to make high quality FeGa thin film. Secondly, the magnetostriction is high, and it still has advantage of being less brittle than Terfenol-D. Third, thin film FeGa can be deposited at room temperature which minimizes the degradation of the PZT layer under it, because high temperature (above 300 °C) treatment for long time leads to the diffusion of Lead in PZT, which degrades the ferroelectric and piezoelectric properties of PZT.

2.4 Magnetolectric Coupling

2.4.1 Magnetic Field Sensing

New magnetic field sensors are needed in the applications such as magnetoencephalography [75,76] and under water magnetic field detectors [77,78]. These applications require the sensitivity from 1 pT/ $\sqrt{\text{Hz}}$ level to 10 fT/ $\sqrt{\text{Hz}}$ level at low frequency (10^{-2} to 10^3 Hz), where

superconducting quantum interference devices (SQUID) magnetometers can serve very well with its sensitivity of $1 \text{ fT}/\sqrt{\text{Hz}}$ for low temperature (below 4.2 K) [79]. The noise floor would increase one order of magnitude when measured at 77 K instead of 4.2 K due to more thermal environmental noise. The SQUID magnetometers are the most sensitive magnetic field sensors. Also they don't suffer from pink noise, also called $1/f$ noise, which usually dominates the noise floor for the other magnetometer techniques at the frequency below 1000 Hz. However, given that it has to operate at very low temperature, SQUID magnetometers are also expensive and inconvenient. Thus, there are alternative magnetic field sensor technologies such as atomic magnetometer [80] and magnetic tunnel junctions (MTJ) [81]. These two techniques are both active sensors which require either an optical pumping signal or an electric current signal. The atomic magnetometer is able to reach the noise level $\text{fT}/\sqrt{\text{Hz}}$ at low frequencies [82], however, it has a size as big as 1000 cm^3 . A relatively smaller atomic sensor was able to detect magnetoencephalographic signals (0.6 pT at 10 Hz) that are believed to be the signal from the brain linked to closing and opening of eyes [80]. Recently, the MTJ magnetometers with the help of flux concentrator have reached noise level of $50 \text{ pT}/\sqrt{\text{Hz}}$ at 1 Hz, and $5 \text{ pT}/\sqrt{\text{Hz}}$ at 100 Hz at room temperature [81]. Flux concentrator modulation is believed to further reduce the $1/f$ noise to $1 \text{ pT}/\sqrt{\text{Hz}}$ at 1 Hz [83]. An interesting hybrid giant magnetoresistive (GMR) sensor with a superconducting flux-to-field transformer has reached noise level of $300 \text{ fT}/\sqrt{\text{Hz}}$ at 4.2 K and 1 Hz [84].

Magnetolectric (ME) sensors are another promising magnetometers. Unlike previously mentioned sensors, the ME sensors are passive, thus, they consume very low power. Thanks to the ME coupling, the ME sensor can convert a magnetic field signal to an electric field directly. It has wide range (10^{-11} to 10^{-3} T) in AC magnetic field sensing [85]. The $1/f$ noise still limits the

sensitivity at low frequency range (below 1000 Hz). Wang, *et al.* showed that their (80 mm × 10 mm) ME sensor has noise floor of 10 pT/ $\sqrt{\text{Hz}}$ at 1 Hz and 1 pT/ $\sqrt{\text{Hz}}$ at 10 Hz at room temperature [86]. Jahns, *et al.* showed that their cantilever device has sensitivity of 7.1 pT/ $\sqrt{\text{Hz}}$ at resonant frequency of 669 Hz [87]. They also showed the sensitivity at 1 Hz is improved by factor of 1000 from 1 $\mu\text{T}/\sqrt{\text{Hz}}$ to 1 nT/ $\sqrt{\text{Hz}}$ by using frequency conversion modulation. This modulation technique is similar to the flux concentrator modulation that is used to help MTJ sensors to reduce 1/f noise.

2.4.2 The ME Coefficient and the ME Magnetic Field Sensors

Because of the magnetoelectric effect, our multiferroic devices have great potential of being new magnetic field sensors. With magnetoelectric coupling, magnetic field applied on ME devices will be converted to an electric voltage signal, which can then be easily measured by electronics such as a lock-in amplifier.

The ME coefficient is a figure of merit of multiferroic magnetic field sensors. It provides us a guideline as to the efficiency of the ME sensors. Under the same noise conditions, given ME sensors with the same size, the higher the ME coefficient is, the more sensitive the ME sensor will be. Thus, the lower magnetic field can be detected with a high ME coefficient device.

Magnetoelectric coupling exists in both single phase materials and composite materials. Here we mainly discuss the coupling in composite materials. As we discussed previously in Section 1.3.2, composite multiferroic materials usually have ME coefficients (22 V/(cm × Oe) at 1Hz and 750 V/(cm × Oe) at resonance for FeBSiC/PZT-fiber [53]) which are orders of magnitude higher than those of single phase multiferroic materials (20 mV/(cm × Oe) for Cr₂O₃ [13]). It is also important to note that most composite multiferroic materials are functional at room

temperature, whereas, many single phase multiferroic materials such as manganite only display the ME coupling at low temperatures. Therefore it is more practical to study composite materials for ME sensors.

As we previously mentioned, the ME coefficient is defined as

$$\alpha_{ME} = \frac{E}{H} \quad (2.10)$$

, where E is the electric field induced in piezoelectric materials and H is external field applied in magnetostrictive materials.

For 2-2 laminate structure, if the applied field is along the film direction and the electric field is measured in the perpendicular direction, then the ME coefficient can be written as

$$\alpha = \frac{\partial E_3}{\partial H_1} = \frac{\partial D_3}{\xi \partial \sigma_1} \times \frac{\partial \lambda_1}{\partial H_1} \times \frac{\partial \sigma_1}{\partial \lambda_1} \quad (2.11)$$

, where E_3 is electric field in the piezoelectric film, H_1 is the magnetic field on magnetostrictive film, D_3 is charge density on piezoelectric film, σ_1 is Stress in piezoelectric film, λ_1 is magnetostriction strain in magnetostrictive film, and ξ is dielectric constant of the piezoelectric film.

In Eq. (2.11), the first part $\frac{\partial D_3}{\xi \partial \sigma_1} = \frac{d_{31}}{\xi}$ depends on the ratio of the piezoelectric coefficient d_{31} and the dielectric constant ξ in the piezoelectric material. The second part $\frac{\partial \lambda_1}{\partial H_1}$, called the magnetoelastic sensitivity, depends on the slope of magnetostriction versus external magnetic field in magnetostrictive materials. The third part $\frac{\partial \sigma_1}{\partial \lambda_1}$ is the mechanical coupling between the magnetostrictive materials and the piezoelectric materials.

To optimize the ME coefficient, so that ME sensors will be more sensitive, researchers need to maximize the product of these three parts in the Eq. (2.11). With the advantage of using

composite materials, we have the freedom to choose piezoelectric materials and magnetostrictive materials quite independently. To maximize the piezoelectric coefficient d_{31} , we can use large d_{31} materials such as PZT. However, in some cases, materials with a smaller d_{31} but also a smaller ξ are also desired, such as AlN. The d_{31} of AlN is 2 pC/N which is very small compared to the d_{31} value of 120 pC/N of PZT. However, dielectric constant of AlN is more than 100 times smaller than that of PZT [88]. This makes AlN a generally competitive material not just for ME sensors but also for piezoelectric sensors and actuators.

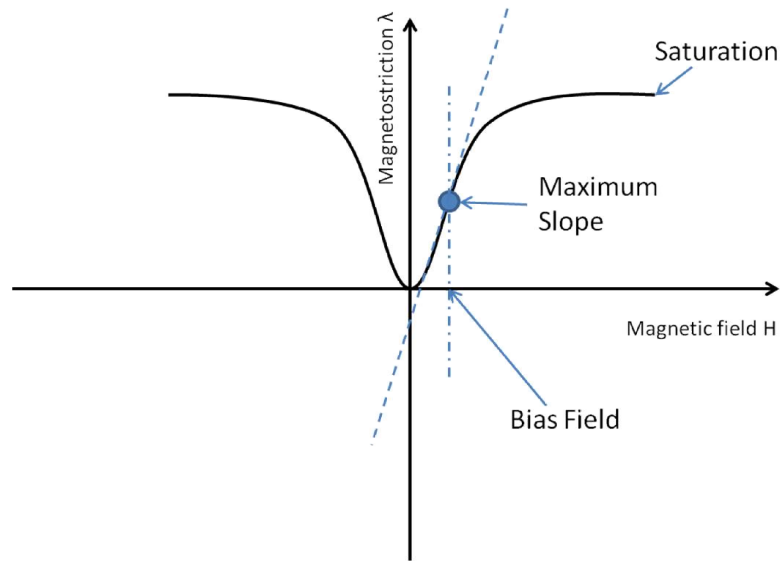


Fig. 2.5 Typical magnetostriction as a function of magnetic field for positive magnetostrictive materials

For the magnetostrictive material, not only do we need the maximum magnetostriction strain to be large, we also need a large slope in the λ - H plot. For a typical λ - H plot as in Fig. 2.5 for positive magnetostrictive materials, which expands under magnetic field, the magnetostriction is mirror symmetric with respect to $H = 0$. The magnetostriction saturates at high magnetic field. In

the case of either $H = 0$ or when H is too large, the slope of magnetostriction is zero. This will make the magnetoelectric coefficient zero, according to Eq. (2.11). In order to get the highest slope in the plot, which is $\frac{\partial \lambda_1}{\partial H_1}$, the material needs to be biased. With optimized bias field applied, the ME sensors will have the highest ME coefficient.

Fig. 2.5 also tells us that it is better to choose those materials with a high saturation magnetostriction but a low saturation magnetic field to get a high ME coefficients.

	λ_s (ppm)	H_{bias} (Oe)	μ_r	$(d\lambda/dH)_{max}$ (ppm/Oe)[89]	Ref.
Terfenol-D	1600	400	< 10 [90]	1	[85,91]
FeGa	270	90	61-285 [92]	0.5	[22,93]
Metglas	42	8	1,000,000 [94]	4	[60]
CoFe ₂ O ₄	-146	2000	< 2 [95]	0.05	[74,96]

Table 2.1 Materials' magnetostriction, bias magnetic field needed to optimize their ME coefficients, relative permeability, and magnetoelastic sensitivity. λ_s is the saturation magnetostriction, H_{bias} is the DC Bias magnetic field to maximize the magnetoelastic sensitivity $(d\lambda/dH)$, $(d\lambda/dH)_{max}$ is the maximum magnetoelastic sensitivity, and μ_r is the relative permeability.

Table 2.1 lists related properties for four magnetostrictive materials that are commonly studied for ME sensors. Terfenol-D has the highest magnetostriction in all materials. As a result, it has very high magnetoelastic sensitivity among all materials. The disadvantage of Terfenol-D

is its brittleness, which limits its applications in some areas. The second material in Table 2.1 is the FeGa, which has a smaller magnetostriction and smaller magnetoelastic sensitivity than Terfenol-D. However, unlike Terfenol-D, FeGa is more ductile, and it requires a much smaller bias field. The third material in the Table 2.1 is Metglas. Metglas is very special in that even though it has the lowest magnetostriction, it still has the highest magnetoelastic sensitivity due to its high permeability. In this case, magnetostrictive part can be expanded into $\frac{\partial \lambda_1}{\partial H_1} = \frac{\partial \lambda_1}{\partial M} \times \frac{\partial M}{\partial H_1}$, where M is the magnetization of the material. $\frac{\partial M}{\partial H_1}$ is, in fact, the permeability of the magnetic material. It is therefore good to use materials with high permeability to pursue high ME coefficients, for example Metglas with the relative permeability of 1,000,000. The last material on the Table 2.1 is CoFe₂O₄. It has the lowest magnetoelastic sensitivity among the four, but it is an insulating spinel oxide, and because it is optically transparent, it can be useful in designing devices coupling magnetostriction with optical properties. An example from our group is a magnetic field sensor where the readout is performed via optical signals [97].

2.4.3 Characteristics of Large ME Devices (4.5 mm × 20 mm × 30 μm)

Previously, we discussed magnetostriction as a function of magnetic field (Fig. 2.5). We had stated that a bias field is needed to maximize the magnetostriction slope as a function of DC magnetic field ($\frac{\partial \lambda}{\partial H}$). We are now to plot this slope as a function of magnetic field, it is essentially the ME coefficient as a function of magnetic field without the piezoelectric part and magnetoelectric coupling part in the Eq. (2.11).

Fig. 2.6 plots the ME coefficient as a function of DC bias magnetic field, called the butterfly curve, for a PZT/FeGa (4.5 mm × 20 mm × 30 μm) cantilever fabricated by Peng, *et al.* [22]. Peng used the cantilever structure to enhance the signal at the mechanical resonance. The

cantilever device (Fig. 2.8) is fabricated by first back-etching the substrate (Si/SiO₂ (30 μm)). This is followed by the deposition of Ti/Pt bottom electrode layers (20 nm/90 nm), a sol-gel PZT layer (1.5 μm), a buffer Pt layer (40 nm), and then sputtering of the FeGa layer (1.5 μm). The cantilevers are then released by laser cutting.

As shown in the Fig. 2.8, AC and DC magnetic field are both applied along the cantilever. Thus, the magnetostrictive FeGa layer will respond to the magnetic field and bend the cantilever according to the driving frequency of the AC magnetic field. At the same time, the piezoelectric PZT layer will respond to the stress from the FeGa layer, inducing a piezoelectric voltage which can be picked up by a lock-in amplifier. This piezoelectric voltage, together with thickness of PZT and AC field amplitude, give us the ME coefficient according to formula

$$\alpha = \frac{dE}{dH} = \frac{V_{\text{piezo}}}{\text{Thickness}_{\text{PZT}} \times H_{\text{AC}}}, \quad (2.12)$$

Because the cantilever is a resonant device, the ME coefficient is maximized at the resonant frequency 333 Hz, as shown in the insert of Fig. 2.6. The resonant frequency of the fundamental vibrational mode is 333 Hz. Further discussion about the different vibrational mode will be presented in Chapter 3. With the help of the mechanical resonance, the ME coefficient is amplified at the resonant frequency. The resonant frequencies of cantilevers can be calculated and measured accurately, and we will introduce this in the later discussion. In relatively large and thick devices such as Peng's device, the resonant frequency is almost exclusively a function of the cantilever dimensions. However, the frequency begins to show a strong departure for smaller devices. This is the main focus of discussion in Chapter 3.

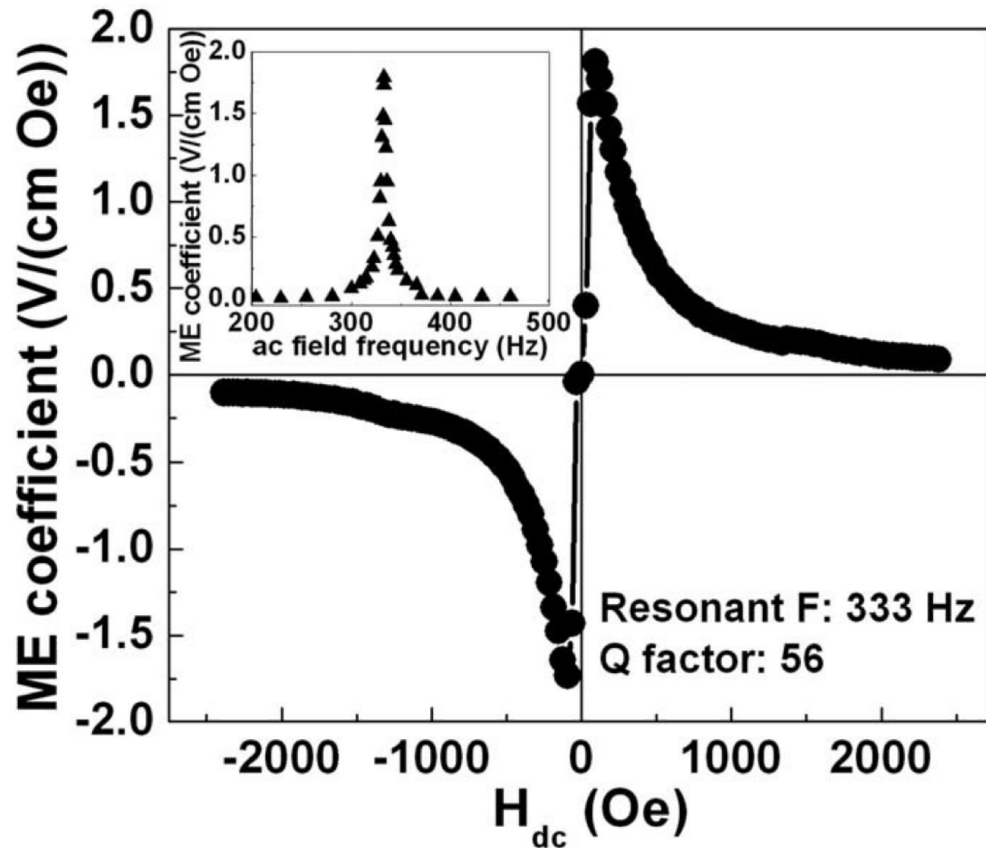


Fig. 2.6 Butterfly curve: ME coefficient as a function of DC bias magnetic field in air. The AC magnetic field is 1 Oe at the resonant frequency of 333 Hz in the fundamental vibrational mode. The insert shows ME coefficient as a function of AC magnetic field frequency. [22]

The curve in Fig. 2.6 is also called the butterfly curve for the ME coefficient, as the shape of the curve looks like a butterfly. The signal is detected with the driving magnetic field being at the resonance when the cantilever is in air. This curve shows that without a bias field the ME coefficient is zero. With a bias field of approximately 90 Oe, the ME coefficient is maximized, and the quality factor of the cantilever is 56. As the bias field is further increased, the ME coefficient decreases. The ME coefficient finally almost reaches zero when bias field is about 2500 Oe, which is the saturation field of the FeGa layer.

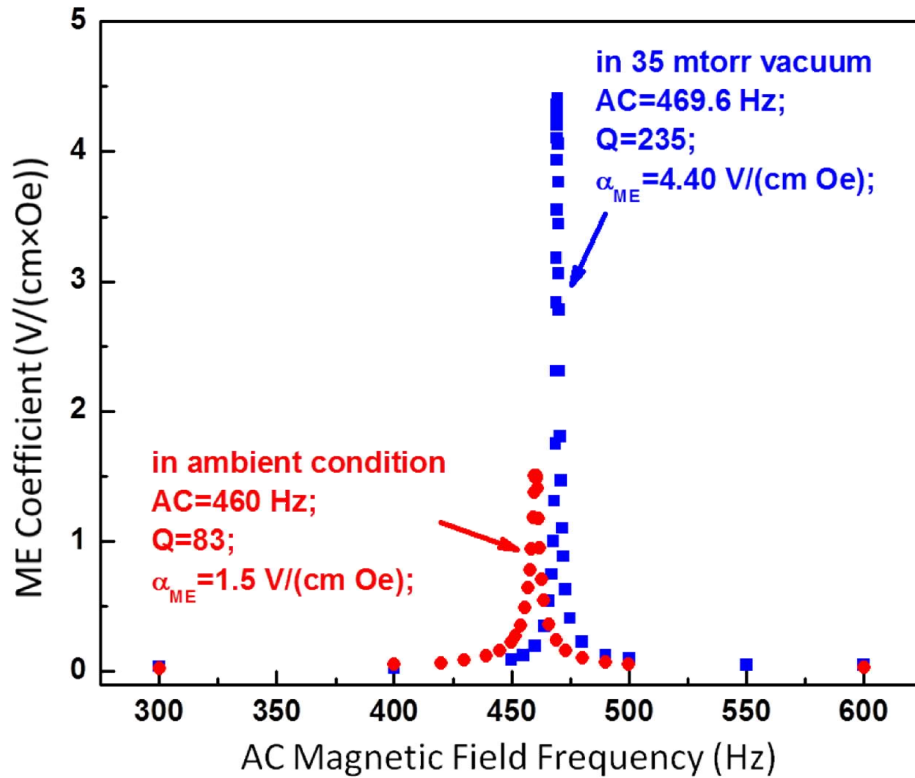


Fig. 2.7 The frequency response of the ME coefficient. Blue dots show the ME coefficients of the device in 35 mTorr vacuum pressure, while red dots show the ME coefficient of the device in ambient condition.

The cantilever in atmosphere is damped by the air. Thus, to optimize the ME coefficient, we need to place the device in vacuum. As shown in Fig. 2.7, the quality factor (Q) of the cantilever is increased from 83 in ambient condition to 235 in 35 mTorr vacuum. The ME coefficient at the resonant frequency is also increased from 1.5 V/(cm × Oe) to 4.4 V/(cm × Oe) by going from air to vacuum. The resonant frequency is slightly shifted from 460 Hz in air to 469.6 Hz in vacuum.

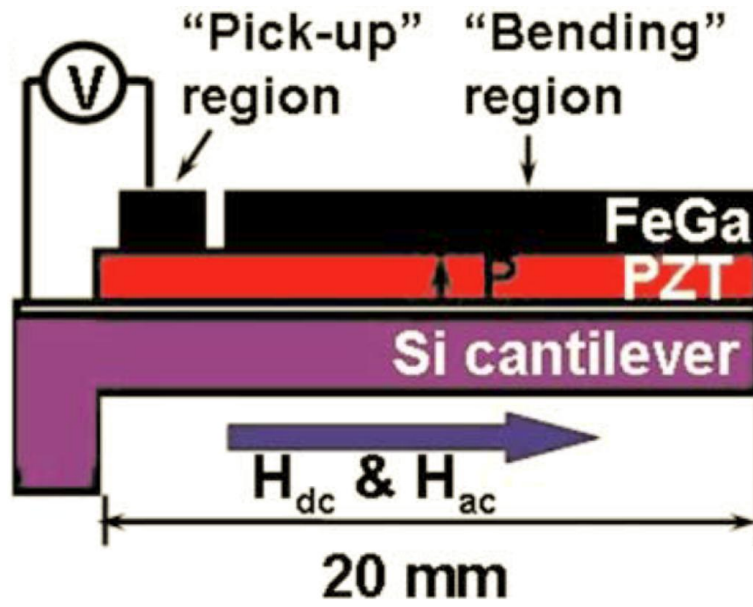


Fig. 2.8 Schematic illustration of FeGa/PZT Peng's cantilever ($4.5 \text{ mm} \times 20 \text{ mm} \times 30 \text{ }\mu\text{m}$). The "Bending" region refers to the part of the cantilever which bends. The "Pick-up region" refers to the region of the voltage where the stress induced piezo voltage is read. In this region, the top FeGa layer is also the top electrode. Underneath the PZT layer, there is a Pt layer which is the bottom electrode.

2.4.4 The Clamping Effect on Thin Films from the Substrate.

In the study by Peng, *et al.*, a $1.5 \text{ }\mu\text{m}$ thick PZT layer and a $1.5 \text{ }\mu\text{m}$ thick FeGa layer were deposited on the $35 \text{ }\mu\text{m}$ Si cantilever, as shown in Fig. 2.8. Compared to bulk ME sensors that are glued by epoxy resin [23], the PZT and FeGa thin film sensors have the advantage of having natural mechanical coupling due to physical thin film adhesion between them and the flexibility to be able to make sensor arrays and other integrate circuits depending on the design. However, because of the presence of the Si substrate, the thin film devices suffer from the clamping effect, which reduces the total ME effect.

Regarding the clamping effect, Peng, *et al.* did a study of the ME coefficient as a function of the thickness of Si substrate [22]. As shown in Fig. 2.9, without changing the thickness of PZT/FeGa layers, as the thickness of the Si substrate decreases, the ME coefficient increases. It is almost 0 V/(cm × Oe) for 400 μm, and it is increased to 1.8 V/(cm × Oe) for 30 μm.

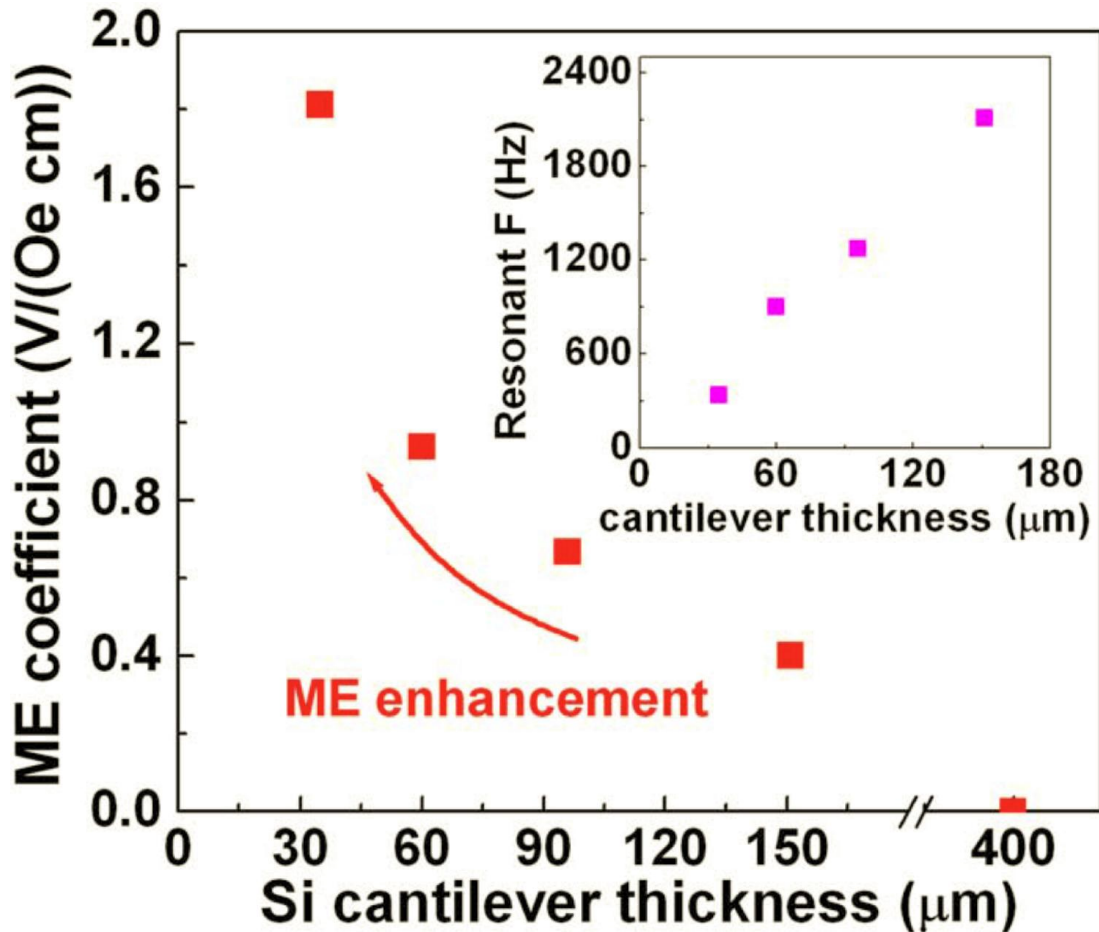


Fig. 2.9. The ME coefficient as a function of cantilever thickness. The PZT/FeGa devices with 1 mm² pick-up region are poled with 210 kV/cm, operated at 90 Oe DC bias magnetic field and excited at their resonant frequencies. The inset shows the linear relationship between the resonant frequency and the thickness of the cantilevers [22]. The “ME enhancement” trend shows that as the thickness of the Si substrate is reduced, the ME coefficient is increased.

The Si substrate thickness was varied by etching the cantilever from the back. This clearly indicates that the thinner the substrate is, the smaller the clamping effect. As a result, as long as there is enough support to the overall structure, one would wish to minimize the thickness of the Si substrate to enhance the ME coupling. As shown in the insert of Fig. 2.9, reducing the thickness of the substrate also leads to linear reduction of the resonant frequency, due to the change in mass of the cantilever. Another way to “tune” the resonant frequency of the device is to reduce the length of the cantilever, which will offset the change due to the loss of mass. More detailed information regarding resonant frequency of cantilevers will be presented in the next chapter.

2.5 Conclusion

In this Chapter, necessary background information for the main thesis work is presented. Magnetolectric materials are useful in applications such as magnetic field sensors, actuators, energy harvesters, and transducers. The ME coefficient is an important figure of merit of ME devices. The piezoelectric material PZT and the magnetostrictive FeGa compose the bilayer composite multiferroic cantilever device. The fundamentals of piezoelectricity, ferroelectricity, magnetostriction, and ferromagnetism were discussed. The cantilever structure we adopted for our devices has the benefit that the magnetolectric signal is boosted at its resonance.

Chapter 3: Basic Characteristics of Multiferroic

Cantilevers and Their Application in Energy Harvesting

3.1 Magnetic Field Sensing Mode

In the previous chapter, we discussed using the device for magnetic field sensors. This is where AC magnetic field induces AC electric voltage through the magnetoelectric coupling effect. The DC bias magnetic field is used to optimize the ME coefficient. We call this the magnetic field driven mode or magnetic field sensing mode. Using the same scheme, we can use the cantilever for other applications. In particular, we discuss energy harvesters. Here AC magnetic field is the “source” of the energy. In previous chapter, we saw the clamping effect of the ME coefficient from the Si substrate. The important goal of going to those smaller dimensional cantilevers ($0.95 \text{ mm} \times 0.2 \text{ mm} \times 5 \text{ }\mu\text{m}$) is that we can go to much thinner Si substrate. In fact, they are so thin that we call them free-standing.

We show the magnetic driving linear mode operation of a $0.95 \text{ mm} \times 0.2 \text{ mm} \times 5 \text{ }\mu\text{m}$ FeGa/PZT multiferroic cantilevers, which are smaller devices compared with the cantilevers we discussed in the previous chapter. First, a general fabrication process for this cantilever device will be introduced. Then, the measurement set up will be discussed. Thirdly, experimental data with a new type of magnetoelectric butterfly curve that involves resonant frequency dependence on DC bias field will be presented. Following this, a magnetic cantilever theory derived by S. E. Loftland will be used to explain the resonant frequency shift under bias field. Lastly, energy harvesting application of the device is discussed.

3.2 Fabrication of FeGa/PZT Multiferroic Cantilevers

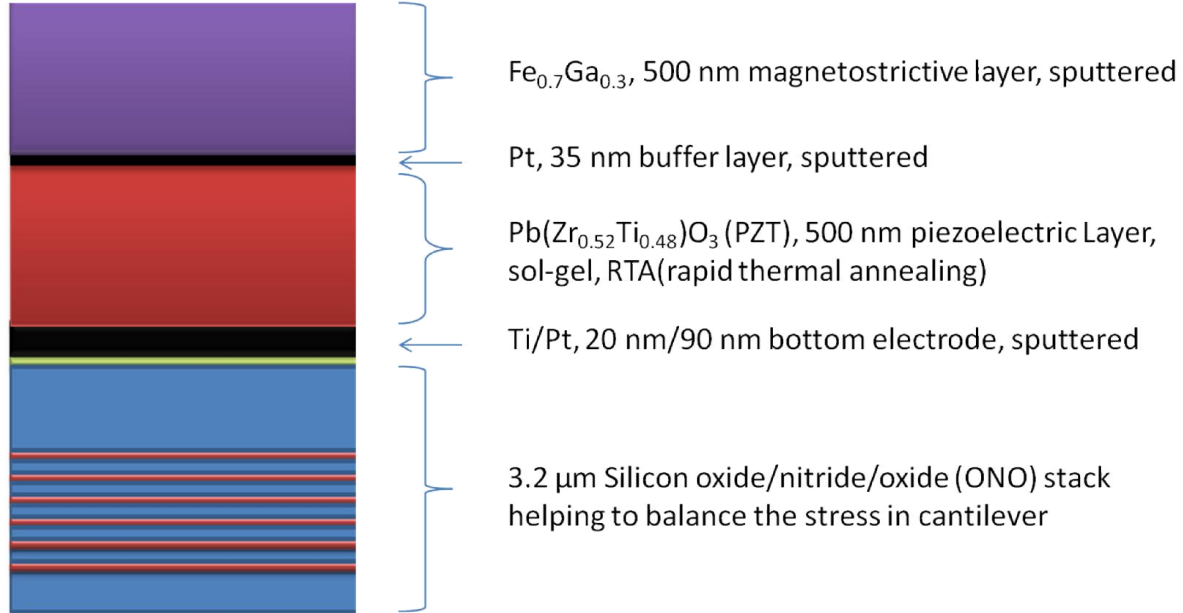


Fig. 3.1 The heterostructure of FeGa/PZT multiferroic cantilever. Silicon oxide is in blue.

The FeGa/PZT multiferroic cantilevers, which are fabricated by Tiberiu-Dan Onuta, consist of a heterostructure that includes 500 nm magnetostrictive Fe_{0.7}Ga_{0.3}, 500 nm piezoelectric Pb(Zr_{0.52}Ti_{0.48})O₃ (PZT), 35 nm platinum buffer layer between FeGa and PZT, 20 nm/90 nm Ti/Pt bottom electrode, and a silicon oxide/silicon nitride/silicon oxide (ONO) stack substrate (Fig. 3.1). The order for materials growth is from bottom to the top, as shown in the figure.

An ONO stack was grown on a Si substrate, using plasma enhanced - chemical vapor depositions (PE-CVD processes) in an Oxford PlasmaLab 100 system. Silane and NO₂ were used as precursors for silicon oxide growth while silane and NH₃ were used for silicon nitride. Rapid thermal annealing (RTA) was used to release stress in the ONO stack. It is necessary to check if the structure develops cracking during RTA, as RTA is also used in a subsequent deposition process of PZT. The proper thickness of nitride layers is important to make sure we get the proper amount of stress. Fig. 3.2 (a) shows cantilevers with a 50 nm nitride film which bend up,

while Fig. 3.2 (b) shows those with a 100 nm nitride film which bend down. The cantilevers with a 75 nm nitride are straight as seen in Fig. 3.2 (c).

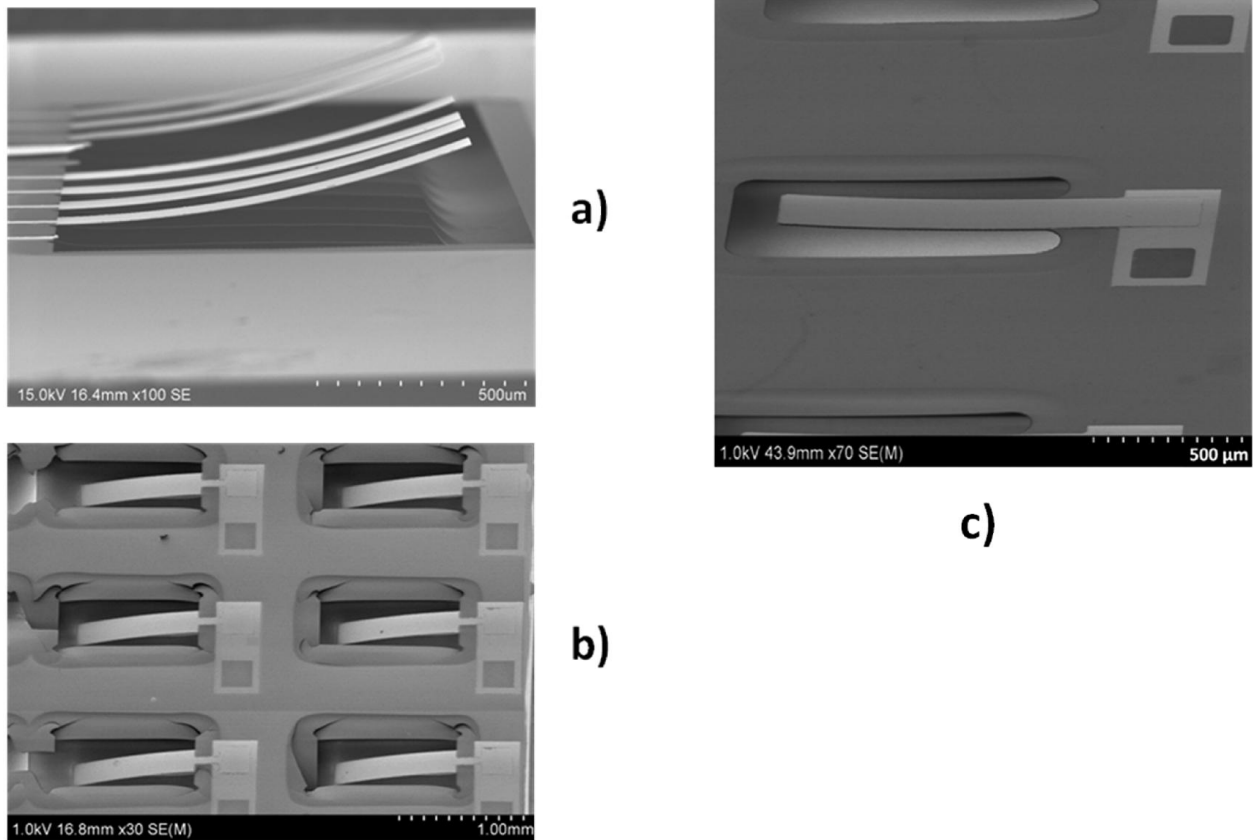


Fig. 3.2 Multiferroic cantilevers with 50 nm silicon nitride films in (a) bend up, with 100 nm silicon nitride films in (b) bend down, and with 75 nm silicon nitride films in (c) are straight.

The next layer on top of the ONO stack is the bottom electrode layer, which is a magnetron sputtered Ti/Pt bilayer. The Ti layer was sputtered as an adhesion layer for the Pt layer. The sputtered Pt layer is mostly a (111) oriented polycrystalline film. Post deposition annealing at 690 °C is necessary to optimize the (111) orientation [98]. This orientation is important to ensure the next layer of polycrystalline PZT is mostly (111) oriented also.

The next thin film on top of the Pt layer is the piezoelectric PZT layer which is deposited using a standard sol-gel method [99]. A two-step spin was used to ensure the uniformity of the PZT film. Rapid thermal annealing in oxygen was carried out at 690 °C for 3 minutes to crystallize the PZT film. The PZT is polycrystalline with (111) orientation dominating because of the (111) Pt layer underneath [100].

After the PZT layer deposition, there is a 35 nm thin buffer layer of Pt sputtered. The buffer layer is added to strengthen the mechanical coupling between PZT and FeGa, which leads to a stronger magnetoelectric coupling effect. According to study from Peng *et al.* [22], the Pt buffer layer in between PZT and FeGa is able to reduce possible leakage current in PZT by providing equal potential at the surface of the PZT layer. They have found that the effect of this is the ME voltage is nearly doubled by adding the Pt buffer layer.

On top of the buffer layer is the magnetostrictive FeGa that was magnetron sputtered at room temperature. The chemical concentration ratio of 0.7:0.3 ensures the FeGa thin film has the highest magnetostriction [19] as discussed in Chapter 2. There is then another 12 nm Pt layer on top for protection of FeGa from oxidation.

3.3 Cantilever Theory

We fabricate our devices on cantilevers to take advantage of the enhancement in the ME signal through their mechanical resonance. Cantilevers are resonant devices that are widely used in sensors, actuators, and energy harvesters. Silicon tips in atomic force microscope (AFM) are used to detect the atomic force between the tip and samples, so that topography of a surface under study can be analyzed [101-103]. For biochemical and medical applications, where even a single molecule can be detected, cantilevers based on micro/nano-electromechanical systems

(MEMS/NEMS) are strong candidates as high sensitivity mass sensors [104]. When functional materials such as magnetostrictive/piezoelectric materials are deposited on the cantilevers, the cantilevers can be used as magnetic field sensors [22,27,105] and electromagnetic energy harvesters [28]. Fig.3.3 shows some examples of cantilevers in various applications. The MEMS/NEMS cantilevers are commonly fabricated from silicon, silicon nitride, and silicon oxide.

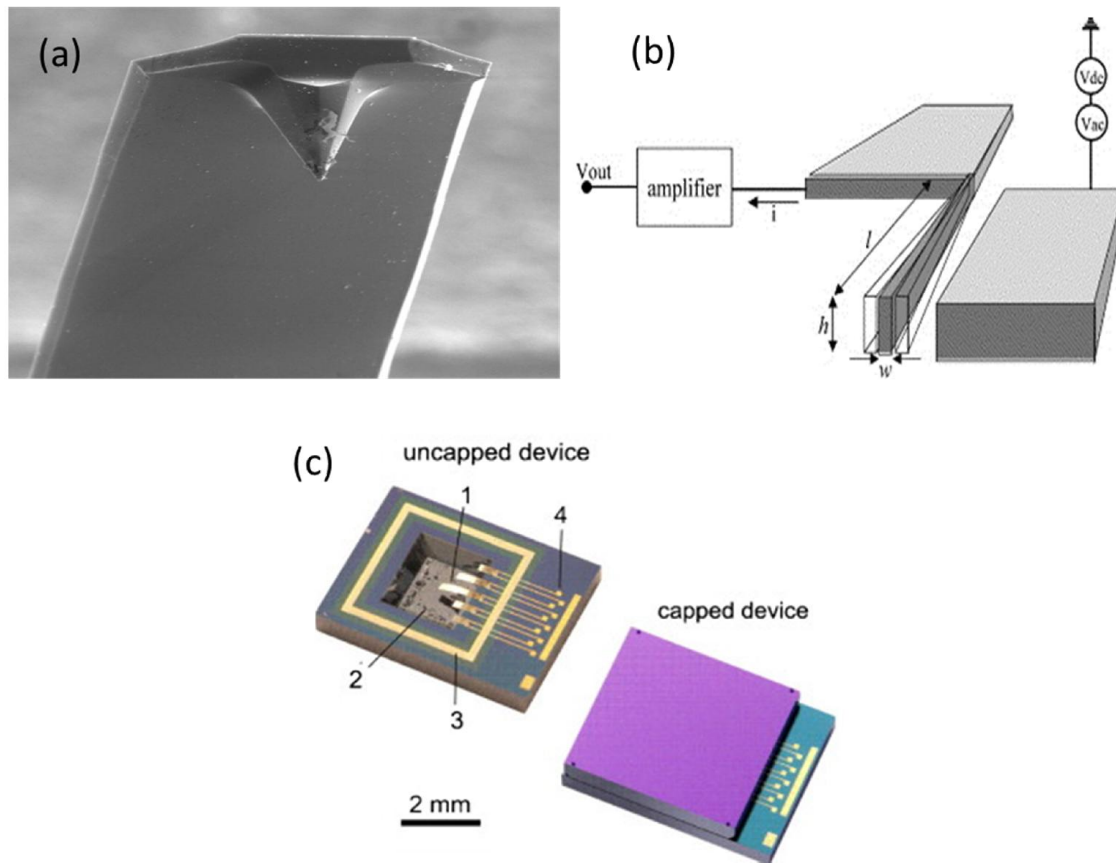


Fig. 3.3 Examples of cantilevers. (a) A scanning electron microscope (SEM) image of an AFM tip. (b) A NEMS Mass sensor [106]. (c) Capped and uncapped magnetic field sensors based on the ME cantilevers, 1 are the cantilevers, 2 is the substrate, 3 and 4 are the two electrodes [105].

Cantilevers which have uniform cross-sections in both width and length directions follow the Euler–Bernoulli beam theory, which is expressed as:

$$EI \frac{\partial^4 z}{\partial x^4} = -\mu \frac{\partial^2 z}{\partial t^2} + q \quad (3.1)$$

, where E is elastic modulus, I is moment of inertia of plane area, z is z coordinate, cantilever deflection, x is x coordinate of point on the beam, μ is mass per length, and q is external load.

In the case of free vibration, where $q=0$, the general solution is found to be

$$z = A_1 \cosh(\beta x) + A_2 \sinh(\beta x) + A_3 \cos(\beta x) + A_4 \sin(\beta x) \quad (3.2)$$

, with $\beta = \left(\frac{\mu \omega^2}{EI}\right)^{1/4}$.

For a cantilever with a length L, boundary conditions are

$$z|_{x=0} = 0, \quad \frac{dz}{dx}|_{x=0} = 0 \quad (3.3)$$

$$\frac{d^2 z}{dx^2}|_{x=L} = 0, \quad \frac{d^3 z}{dx^3}|_{x=L} = 0 \quad (3.4)$$

Non-trivial solutions exist only if $\cosh(\beta x) \cos(\beta x) + 1 = 0$.

This leaves multiple solution modes for β_n , $n=1, 2, 3, 4 \dots$, where $\beta_1 L=1.8751$, $\beta_2 L=4.69409$, $\beta_3 L=7.85476$, $\beta_4 L=10.9955 \dots$

The corresponding frequencies of vibration are $\omega_n = \beta_n^2 \sqrt{\frac{EI}{\mu}}$, $n=1, 2, 3, 4 \dots$

The first four modes are plotted in Fig. 3.4 [107]. However, it is usually the first mode that has the highest deflection. The first mode, also called the fundamental mode, is the preferred mode for sensing and actuating applications.

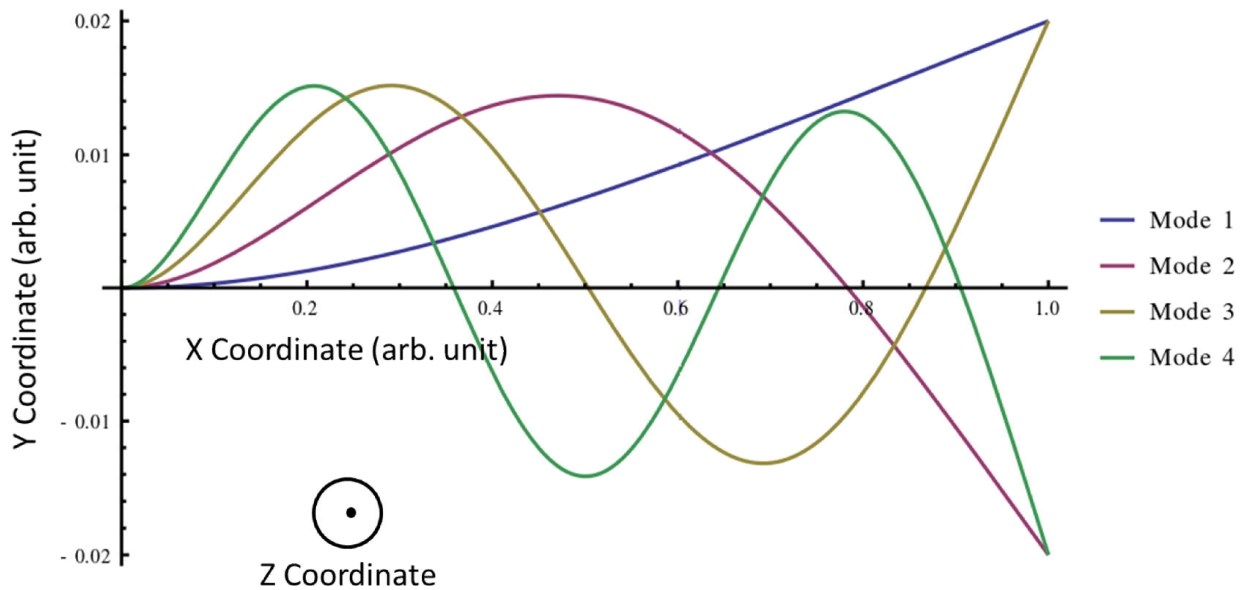


Fig. 3.4 The cross-sectional curves in different colors show different bending styles of the cantilever in different vibration modes. X, Y, and Z are the coordinates, where X is in length direction when the cantilever is at the neutral position, Z is in the width direction, and Y is perpendicular to both of them [107].

3.4 Measurement Setup

The key to the magnetoelectric coupled device is that the piezoelectric voltage in piezoelectric materials can be measured when the magnetic field is applied on the magnetostrictive materials. As shown in the Fig. 3.5, magnetic field applied on the cantilever induces strain in FeGa, which, in turn, applies stress to PZT. PZT experiencing the stress will then develop induced polarization, which gives rise to piezoelectric voltage between its surfaces. The FeGa layer also serves as the top electrode. Then the piezoelectric voltage between the top and bottom electrodes can be detected by a lock-in amplifier, which is locked to the driving frequency of the AC magnetic field.

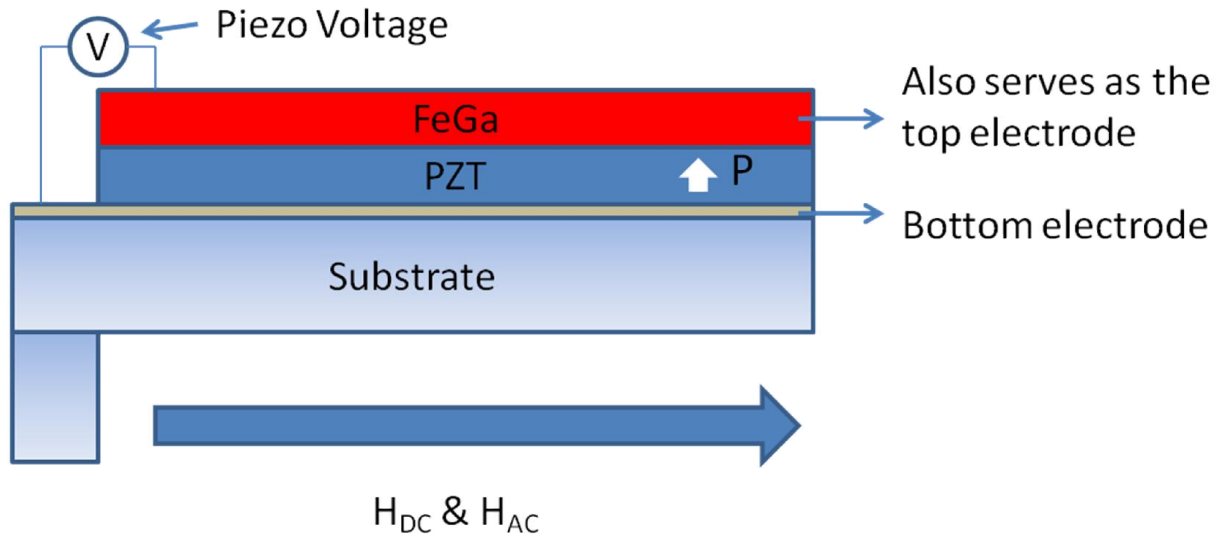
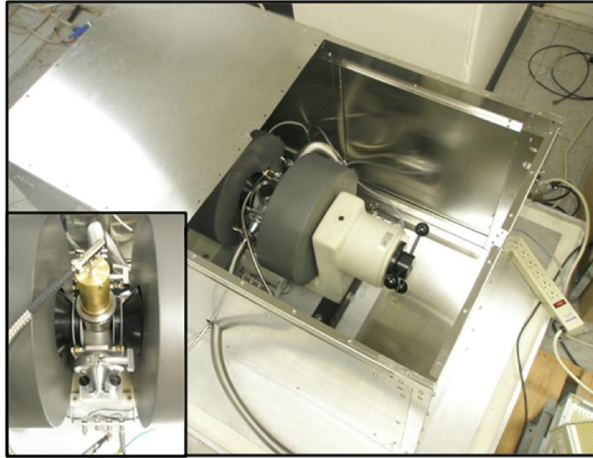


Fig. 3.5 The schematic of magnetoelastic measurement shows piezoelectric voltage across the PZT film is measured when magnetic field is applied along the cantilever.

The cantilever is mounted in a vacuum chamber (Fig. 3.6 (a)), which is surrounded by a pair of large DC coils and a pair of small AC coils (Fig. 3.6 (a) insert). As we discussed in Chapter 2, the cantilever has higher ME coefficient and quality factor in vacuum than in air. The coils and the vacuum chamber together are placed in a mu-metal box which is on a sand box. The mu-metal box shields magnetic field above 20 Hz, leaving us extremely low magnetic field noise of less than $10 \text{ fT}/\sqrt{\text{Hz}}$ [108]. Meanwhile, the sand box isolates most mechanical vibration noise from the ground (Fig 3.6 (b)). The cantilever is mounted in the direction so that it aligns with DC and AC magnetic field. It is also mounted at the center of the coil pairs to get the most uniform magnetic field. Both DC and AC coils are Helmholtz coils with $\partial^2 B/\partial x^2 = 0$ (x is the cantilever longitudinal direction) so that the uniformity of the magnetic field at the center of the coil pairs is optimized.



(a) AC coil and DC coil are in the same direction. Device is in vacuum.



(b) Sand box and a granite sheet placed underneath the mu-metal (20 Hz cut-off)

Fig. 3.6 Magnetic coils and the vacuum chamber are mounted inside of a mu-metal box on a sand box.

The coils, from which the magnetic field is generated, are all calibrated (Fig. 3.7). As we are not going to measure the magnetic field signal directly each time, we would like to refer to the current in either AC coils or DC coils to get the value of magnetic field they are generating. Assuming the linearity of the curves, we can simply multiply a coefficient to convert the current in either coil to obtain the corresponding magnetic field value. For example, for the magnetic field sensing measurements, we need to reliably generate magnetic fields in the range as small as 10 pT. This corresponds to 12.8 nA in AC coils and 0.93 nA in DC coils, which we can control with the Keithley 6221 AC and DC current source.

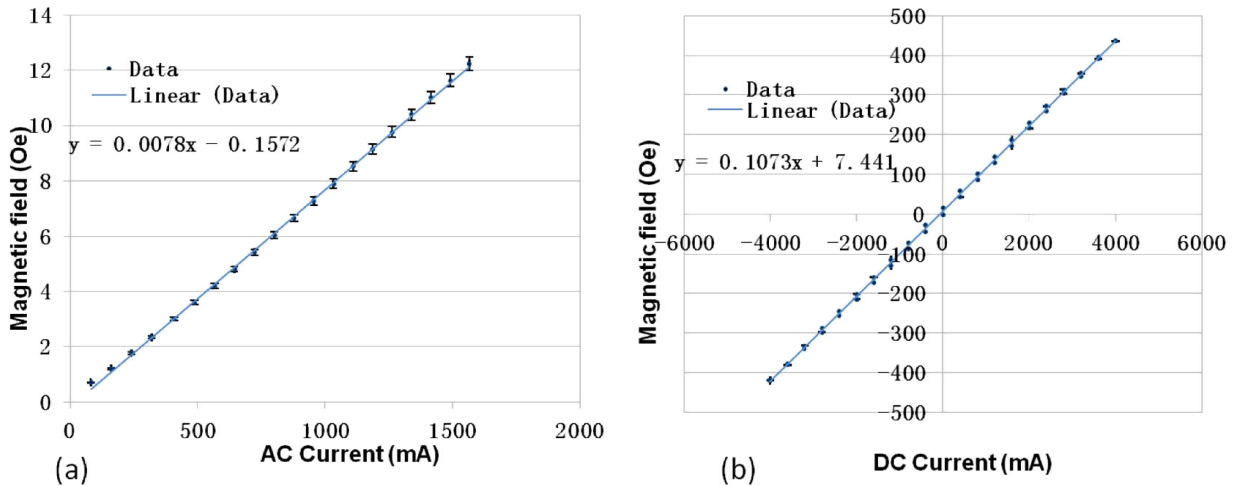


Fig. 3.7 Coils are calibrated so that we know what the magnetic field we are getting is with either AC coils in (a) and DC coils in (b).

3.5 Butterfly Curves for Small Cantilevers ($0.95 \text{ mm} \times 0.2 \text{ mm} \times 5 \text{ }\mu\text{m}$)

As previously introduced in Chapter 2, the butterfly curve (the ME coefficient vs H_{DC}) for the large cantilevers ($4.5 \text{ mm} \times 20 \text{ mm} \times 30 \text{ }\mu\text{m}$) shows that the ME coefficient is purely a function of DC bias field leaving resonant frequency unchanged. However, when we measure this smaller sized cantilevers ($0.95 \text{ mm} \times 0.2 \text{ mm} \times 5 \text{ }\mu\text{m}$), the resonant frequency was found to depend on the DC bias field (Fig. 3.8). In Fig. 3.8 (a), as the DC magnetic field is decreased from around 238 Oe to zero then to about -75 Oe, the resonant frequency decreases from 3843 Hz to 3833 Hz. We also notice that because of the smaller dimensions, the range of the resonant frequency is much larger and it is in the kHz range compared to the earlier larger devices in the 100 Hz range. As the DC bias field continues to decrease from -75 Oe to -238 Oe, the resonant frequency first suddenly jumps from 3833 Hz to 3838 Hz, and then it continues to change linearly from 3838 Hz to 3844 Hz slowly. Fig. 3.8 (b) is obtained by scanning the bias field in the opposite direction from -238 Oe to 238 Oe. As one can see first, the resonant frequency

changes with the bias magnetic field. This shifting of about 10 Hz per 300 Oe is considered to be fairly large, because it is more than a few bandwidth of the frequency scanning curve, which is 1.3-1.9 Hz. It also shows that the bias field generally hardens the spring constant k , as it increases the resonant frequency f_r , because generally f_r is proportional to $k^{1/2}$.

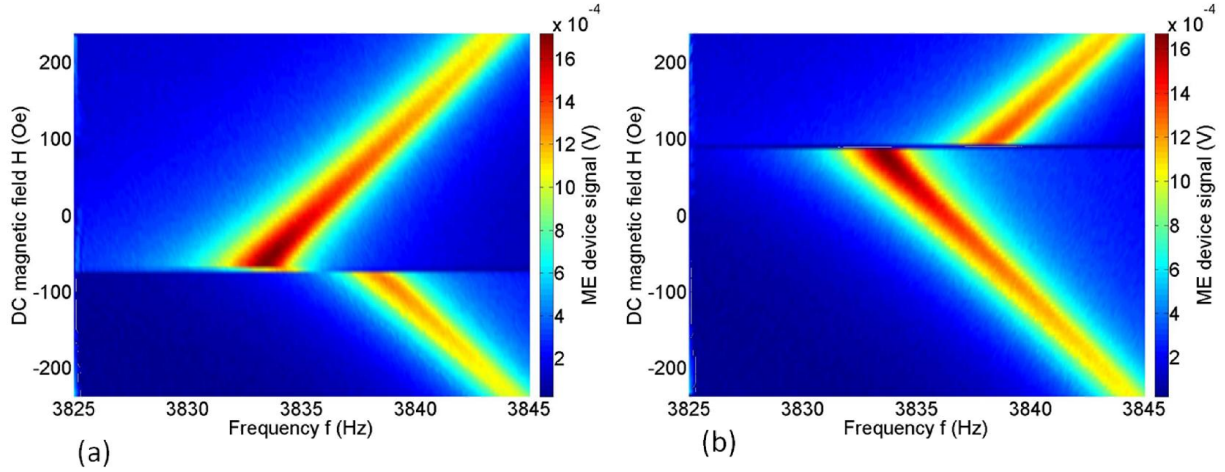


Fig. 3.8 ME signal and the resonant frequency as a function of DC bias field plotted as an intensity plot, while the field is swept in decreasing direction (a), and in increasing direction (b). The AC driving field is 1 Oe field (RMS) [28].

Here, using the highest ME signal, we can calculate our highest ME coefficient α according to Eq. (2.12), where the ME voltage is 1.65 mV, the thickness of the piezoelectric material (PZT) is 500 nm, and the AC magnetic field amplitude is 1 Oe (RMS). Then our highest ME coefficient α is 33 V/(cm \times Oe). We can also reconstructing Eq. (2.12) to calculate our equivalent magnetic field noise floor:

$$H_{AC \text{ noise}} = \frac{V_{\text{piezo noise}}}{\text{Thickness}_{\text{PZT}} \times \alpha} \quad (3.5)$$

Given that our measured $V_{\text{piezo noise}} = 20 \text{ nV}/\sqrt{\text{Hz}}$, then with $\alpha = 33 \text{ V}/(\text{cm} \times \text{Oe})$ and $\text{Thickness}_{\text{PZT}} = 500 \text{ nm}$, our equivalent AC magnetic field noise floor will be $1.2 \times 10^{-5} \text{ Oe}/\sqrt{\text{Hz}}$, which is also $1.2 \text{ nT}/\sqrt{\text{Hz}}$ at resonant frequency (3833 Hz).

It turns out there are very few reports of the phenomenon of the resonant frequency of the cantilevers affected by a DC magnetic field. Previously, a resonant frequency shift was observed in cantilevers with a magnetic particle mounted to the tip of the cantilever [109]. There, the phenomenon was explained as a competition between magnetic anisotropy energy and Zeeman energy with respect to the magnetic particle. But our devices have a different geometry because our cantilevers have a uniform layer of magnetic film deposited on them. To develop a comprehensive understanding of behavior of our cantilevers under magnetic field, S.E. Lofland from Rowan University developed a new theory for the resonant frequency shift of a magnetic cantilever with a uniform magnetic film deposited along the length of the cantilever. The detail of the theory work is presented in the next Section 3.6.

3.6 Derivation of $f_{\text{R, magnetic}}(\mathbf{H}_{\text{DC}})$ Expression and the Fitting of the Data

The total energy U per unit length of a bilayered multiferroic cantilever can be written as a sum of two components, namely the elastic component U_{elastic} and the magnetic component U_{magnetic} :

$$U(z, t) = U_{\text{elastic}}(z, t) + U_{\text{magnetic}}(z, t), \quad (3.6)$$

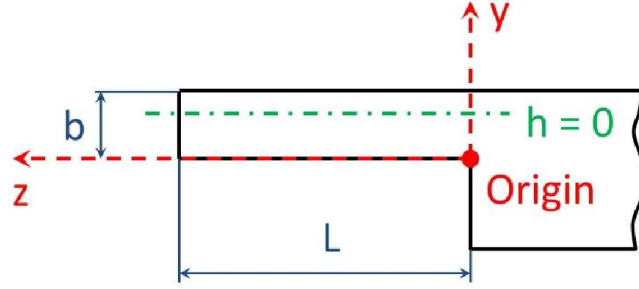


Fig. 3.9 Schematic of a heterostructured multiferroic cantilever and its coordinate system used to describe the formalism behind the resonant frequency shift due to the applied DC magnetic field, H_{DC} .

where z and x are along the cantilever length and in-plane width directions, respectively, (Fig. 3.9) and where $y = y(z, t)$ represents the vertical displacement of the cantilever due to deflection at position z . We place the origin in the middle of the width and at the base of the cantilever root.

We express:

$$U_{\text{elastic}}(z, t) = w \int_{\text{film}}^{(\text{magnetic})} \left[\sigma_m h \frac{d^2 y}{dz^2} + \frac{1}{2} \sigma_m \left(\frac{dy}{dz} \right)^2 \right] dh + w \int_{\text{films}}^{(\text{substrate})} \left[\frac{1}{2} Y_s h^2 \left(\frac{d^2 y}{dz^2} \right)^2 \right] dh \quad (3.7)$$

and

$$U_{\text{magnetic}}(z, t) = w \int_{\text{film}}^{(\text{magnetic})} \left[\frac{1}{2} Y_m(H_{DC}) h^2 \left(\frac{d^2 y}{dz^2} \right)^2 - \mu_0 \vec{M} \cdot \vec{H}_{DC} - \lambda(H_{DC}) Y_m(H_{DC}) \frac{M_z^2}{M_{\text{sat}}^2} h \frac{d^2 y}{dz^2} - \frac{1}{2} \lambda(H_{DC}) Y_m(H_{DC}) \frac{M_z^2}{M_{\text{sat}}^2} \left(\frac{dy}{dz} \right)^2 + \frac{1}{2} \mu_0 M_x^2 \right] dh. \quad (3.8)$$

In Eqs. (3.7, 3.8), the variable h is the vertical position inside the film (FeGa or other non-magnetic film) in the heterostructure from the neutral axis (defined to be where $h = 0$), where there is zero stress on the entire plane (Fig. 3.9). σ_m is the constant internal stress of the *FeGa* film. $Y_m = Y_m(H_{DC})$ and Y_s are the Young's modulus of FeGa and the weighted effective Young's modulus of the multi-layered substrate, respectively. $\lambda = \lambda(H_{DC})$ is the

magnetostriction of FeGa , and M_{sat} is its saturation magnetization. μ_0 is the magnetic permeability of free space and M_x, M_z are the x-, z-components of its magnetization, \vec{M} .

The terms in U are: elastic, internal stress, Zeeman, demagnetization and magnetoelastic in nature. The first term in Eq. (3.7) represents the work done by the internal stress in the FeGa film. The second term is the work done by the torque due to the internal stress in the FeGa film, and the third term is the strain energy in the cantilever substrate. In Eq. (3.8), the first term is the strain energy of the FeGa film, the second term is the Zeeman energy, the third term is the work done by magnetostriction, the fourth term arises from the work done due to the torque from magnetostriction, and the last term represents the demagnetization energy.

To obtain the expression for $f_{R, \text{magnetic}}(H_{\text{DC}})$, Eqs. (3.7) and (3.8) are first integrated along different specified thicknesses within the device structure, and then the total energy from Eq. (3.6) is minimized by evaluating $dU/d\Gamma = 0$ (where $\Gamma = h, M_x$ or M_z) in order to determine both the relative angle of magnetization and the position of the neutral axis (where there is no strain) as a function of z. Assuming that the deflection is small enough so that $dy/dz \sim \theta$ (where θ is the deflection angle of the cantilever) and that the magnetic field does not deviate far from the plane, one can find the Lagrange function of the magnetic cantilever as:

$$\mathcal{L}(x, y, z, t) = \int \left[\frac{1}{2} \rho_{\text{avg}} w b \left(\frac{dy}{dt} \right)^2 - U \right] dz, \quad (3.9)$$

where the first term describes the kinetic energy of the cantilever. The Lagrangian then becomes:

$$\frac{\partial}{\partial t} \left(\frac{\partial \mathcal{L}}{\partial \frac{dy}{dt}} \right) - \left(\frac{\partial \mathcal{L}}{\partial z} \right) + \frac{\partial}{\partial z} \left(\frac{\partial \mathcal{L}}{\partial \frac{dy}{dz}} \right) - \frac{\partial}{\partial z^2} \left(\frac{\partial \mathcal{L}}{\partial \frac{d^2y}{dz^2}} \right) = 0. \quad (3.10)$$

After solving Eq. (3.10), the equation reduces to a differential equation which describes the Euler-Bernoulli beam. The boundary conditions for the Euler-Bernoulli equation are:

$$\begin{cases} y(0) = 0 & \text{(a)} \\ \frac{dy}{dz}(0) = 0 & \text{(b)} \\ \frac{d^2y}{dz^2}(L) = 0 & \text{(c)} \\ \frac{d^3y}{dz^3}(L) + a^2 \frac{dy}{dz}(L) = 0 & \text{(d)} \end{cases}, \quad (3.11)$$

where the coefficient a^2 is the axial load in the magnetic film (Eq. (3.11) d). Analytically, the axial load is described as:

$$a^2 = \frac{(\sigma_m + \lambda Y_m) b_m}{(YI)_{\text{avg}} b}, \quad (3.12)$$

where b_m is the thickness of the FeGa film, b is the total thickness of the cantilever, and $(YI)_{\text{avg}}$ is a weighted average of the product of effective Young's modulus and second moment of inertia of films representing the bending stiffness of the cantilever.

The conditions (a) and (b) are due to the fact that the cantilever end is clamped to its base. The boundary condition (c) is such that the shear energy of the free end of the cantilever is zero and the condition (d) includes the axial load due to the internal stress and magnetostriction. We note that the Lagrangian can also be used to set up the differential equation for the static case. In the magnetic Euler-Bernoulli beam equation, the work done by magnetic torque on an infinitesimal volume element has the same form in the energy term as the work done by the torque produced by the magnetostrictive stress, making it difficult to separate the two from the experimental measurements, although based on this analysis and the relevant values for FeGa, magnetostriction should dominate at low field and the magnetic torque at high field. That is, with the reasonable assumption that the magnetoelastic effects do not change above magnetic saturation, only the magnetic torque will later alter the resonance frequency at high fields. These calculations are based on an idealized cantilever with uniform cross-section (characterized by

weighted geometric and material properties of the stack films). We assume there is no slippage at any of the interfaces.

Assuming that the energy in the FeGa film is much smaller than that of the entire cantilever, the Lagrange formalism leads to the Euler-Bernoulli beam equation, from which the expression for the H_{DC} -field dependent resonance frequency, $f_{R, \text{magnetic}}$, can be derived as:

$$f_{R, \text{magnetic}}(H_{DC}) = f_{R0} \left\{ 1 + \left[\frac{1}{2\pi\rho_{\text{avg}}} \left(\frac{b_m}{b} \right) \frac{\gamma}{f_{R0}} \frac{\mu_0 H_{DC} M^2(H_{DC}) \left(H_{DC} + \frac{1}{2} M(H_{DC}) \right)}{(H_{DC} + M(H_{DC}))^2} + \frac{3b_m}{2(b-b_m)} \lambda(H_{DC}) \frac{\Delta Y_m(H_{DC})}{Y_s} \right] \right\}. \quad (3.13)$$

Here, $\gamma = \zeta^2/f_{R0} = \sqrt{\rho_{\text{avg}}wb/(YI)_{\text{avg}}}$, where f_{R0} is the natural resonant frequency of the fundamental mode, $\zeta (= 1.9/L)$ is the propagation constant for this mode, ρ_{avg} is the weighted density of the entire cantilever, and M is the magnetization along the beam axis. The last term in Eq. (3.13) (which is much smaller than the other terms) leads to the resonant frequency shift due to the H_{DC} -dependent Young's modulus in the magnetic film, where $\Delta Y_m = Y_m(H_{DC} = 0) - Y_m(H_{DC})$. When $\frac{b_m}{b} \rightarrow 0$ or $\frac{b_m}{b-b_m} \rightarrow 0$, we obtain $f_{R, \text{magnetic}}(H_{DC}) \rightarrow f_{R0}$ (from Eq. (3.13)). This shows as the thickness of the magnetic layer increases, the influence of DC magnetic field on the resonant frequency of the cantilever increases. This explains why the earlier devices ($4.5 \text{ mm} \times 20 \text{ mm} \times 30 \text{ }\mu\text{m}$), which have much low fraction of the magnetic layer, did not show any resonant frequency shift due to applied H_{DC} , as we discussed in the previous chapter.

In Fig. 3.10 (a), an overlapped butterfly curve, the ME signal as a function of the DC magnetic field (scanning up and down) and frequency, from another small device is presented. The resonant frequency as a function of DC bias field is extracted in Fig. 3.10 (b), where the

theoretical prediction according to Eq. (3.13) is also presented. The average density of the cantilever and the young's modulus of both magnetic layer and substrate are used as fitting parameters. As we can see, the experimental data of resonant frequency matches the theory very well.

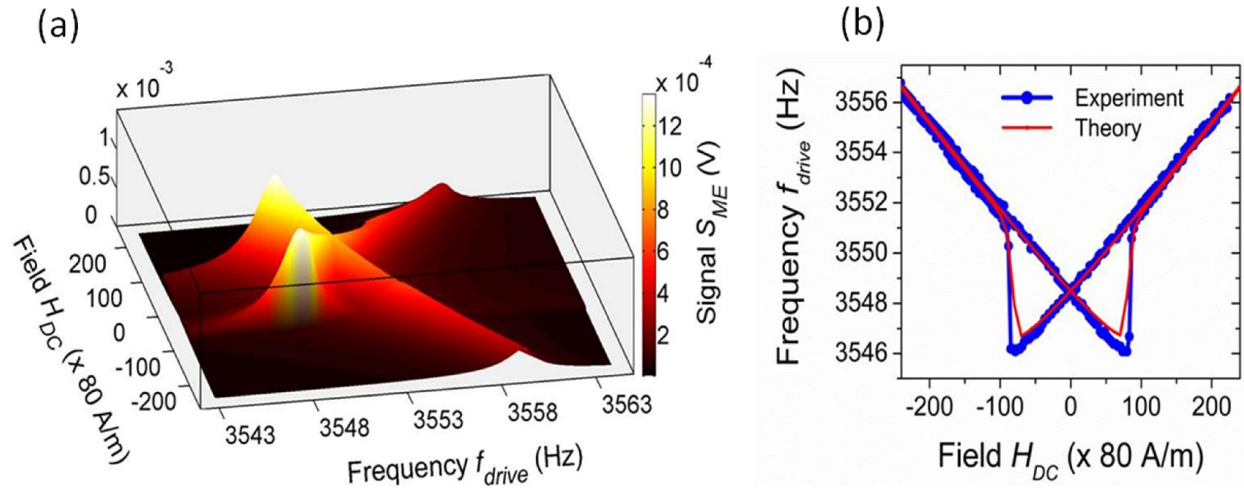


Fig. 3.10. Characteristics of a multiferroic cantilever in linear dynamic regime. (a) Extended butterfly curve of the multiferroic device. The AC magnetic excitation is $H_{AC} = 80$ A/m (RMS), which is also equivalent to 1 Oe. The vertical scale is the device signal (also color coded for clarification). (b) Hysteretic dependence of f_R on H_{DC} . The device first flexural mode is at $f_{R0} = 3548.7$ Hz. Both H_{AC} and H_{DC} are aligned along the cantilever length direction. Measurements are carried out in vacuum of 3.5×10^{-4} mbar. The theory fit $f_{R, magnetic} = f_{R, magnetic}(H_{DC})$ is described in the Supplementary Information.

3.7 Energy Harvesting Applications

Energy harvesting is becoming more and more important in mobile electronics and sensor networks. Not only can it supply extra power to the systems, but it can also help replace the

batteries for microsystems which do not consume too much power [65,110]. In some cases, replacing batteries can be expensive, and the extra wires are troublesome, for example, for heart sensors [111]. There are sensors which need to be placed inside some areas which are difficult to reach (such as inside human body), wireless energy harvesters are ideal to power or charge them. The wireless charging systems based on inductors is already commercially available, such as wireless chargers for Smartphones. However, ME devices, which also convert magnetic energy into electric energy through the magnetoelectric effect, can offer alternative options for wireless charging [112].

In this section, we describe how our device serves as an energy harvester or a transducer, which absorbs electromagnetic waves generated by the AC coils. Magnetic energy is then converted into electricity. Meanwhile, a load resistor is used to share the electric dissipation, as shown in Fig. 3.11. In this scheme, the device serves as a battery of the circuit, while the resistor serves as a load. In this experiment, the range of the load resistor used is from 1k ohm to 4M ohm.

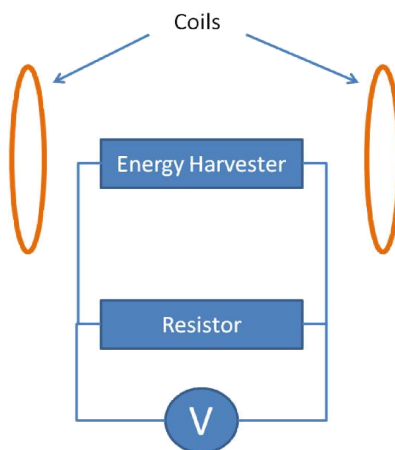


Fig. 3.11 Energy harvesting scheme

To obtain a maximum ME output, we need to operate the device at its resonant frequency, which is a function of the DC bias field. This means the device operates at the peak condition, under which the ME voltage is maximized in Fig. 3.8. That is with DC bias of 66.1 Oe and frequency of 3833.1 Hz where the ME coefficient is 33 V/(cm × Oe). Fig. 3.12 (a) shows that the power dissipation is maximized when load impedance is around 12.5 kΩ, where the load impedance matches the internal impedance of the device. The internal impedance of the device can be calculated as $R_{load} = 1/(2\pi f_{R0} C_0)$, where C_0 is the effective capacitance of the device (measured to be $C_0 = 3.2$ nF).

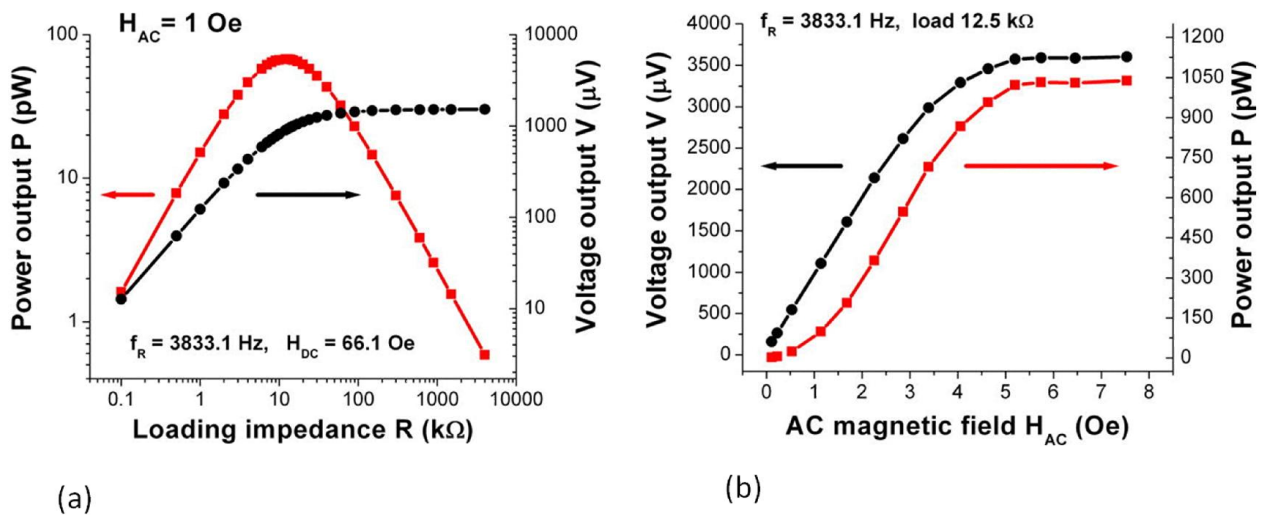


Fig. 3.12 (a) Power and voltage output with variable load impedance. (b) Power and voltage output with varying AC magnetic driving field.

To determine the power density of the multiferroic harvester, an effective volume ($950 \mu\text{m} \times 200 \mu\text{m} \times 0.5 \mu\text{m}$) taking into account the freestanding length of the cantilever and the thickness of the poled (PZT) piezoelectric film was used. The measured peak power density is 0.7 mW/cm^3 (RMS). This value is similar to other reported harvested power densities of bulk

laminated ME devices at 1 Oe (RMS) [112,113]. With a low AC driving field, the electric voltage on load impedance is linear at the beginning. However, as AC magnetic driving field increases up to 3 Oe, the voltage output starts to become nonlinear (Fig. 3.12 (b)). This nonlinearity is because of the Duffing effect, which can be used to design memory device based on mechanical nonlinear vibration and will be further discussed in Chapter 4.

3.8 Conclusion

In this Chapter, multiferroic cantilevers driven by AC magnetic field in the linear mode was investigated. Our clean-room fabricated cantilevers ($950\ \mu\text{m} \times 200\ \mu\text{m} \times 0.5\ \mu\text{m}$) are small enough to present a completely different magnetoelectric behavior as a function of DC bias magnetic field, compared to larger ones previously fabricated and discussed ($4.5\ \text{mm} \times 20\ \text{mm} \times 30\ \mu\text{m}$). The resonant frequency linearly shifts with the DC magnetic field, which is explained by competition between Zeeman energy and anisotropy energy based on a thin film model developed by S. E. Lofland. An application of the ME device in energy harvesting is also demonstrated, where the device behaves like a wireless harvester and energy transducer.

Chapter 4: Dynamic Multiferroic Memory with Nonlinearity

4.1 Introduction

In the linear mode, the driving AC magnetic field is less than 3 Oe, so that the ME cantilevers respond to the AC magnetic field amplitude linearly. In Chapter 3, the linear driving mode of a FeGa/PZT multiferroic cantilever was investigated. For the small cantilevers ($950 \mu\text{m} \times 200 \mu\text{m} \times 0.5 \mu\text{m}$), the magnetoelectric (ME) voltage and the resonant frequency shifts with DC bias field, while the resonant frequency stays the same for large cantilevers ($4.5 \text{ mm} \times 20 \text{ mm} \times 30 \mu\text{m}$). A thin film model was used to explain that the shift is due to the competition between the anisotropic energy and the Zeeman energy of the magnetic film. The linear mode applies to the magnetic field sensing applications. Some ME magnetic field sensors have been shown to achieve sensitivity of $2.3 \text{ pT}/\sqrt{\text{Hz}}$ at resonance ($\sim 1259 \text{ Hz}$) [114,115].

In this chapter, nonlinear driving modes - both magnetic and electric modes are studied. In the nonlinear regime, the AC driving amplitude (magnetic or electric) is strong enough that the cantilever begins to display a nonlinear response. There are two approaches to drive the system into two different nonlinear regimes. The first approach is to parametrically drive a resonant system by periodically modulating the spring constant of the system. We will further discuss the first nonlinear approach in detail in the next Chapter. With the second approach, we use the driving field (E field or B field) which for our devices corresponds to an AC magnetic field above 3 Oe or an AC electric field above 5 mV. In this mode, hysteretic behaviors will appear so that frequency scanning curves split into an upper curve in the frequency increasing direction and

a lower curve in the frequency decreasing direction. Resonant systems in this nonlinear mode are treated as Duffing oscillators [116].

In a nonlinear system, when the system is in a critical state, the small perturbation of the system parameters may lead to a large change in the system state [117]. Thus the nonlinearity of Duffing oscillators are studied to detect very small signals [118] or secure communication through chaotic synchronization [119]. There are studies regarding MEMS Duffing devices. For example, the stochastic switching of cantilevers provides new detection schemes [120], and intermodulation gain of 15 dB is realized for application in high gain narrow band mechanical amplifier with MEMS resonator consisting of double clamped beams [121].

In our case, a bifurcation area arises in the frequency-amplitude plot near the resonant frequency, where the deflection amplitude of the cantilever as well as the device signal can have two possible values, which we define as ‘up’ and ‘down’ states. We show that these two states are switchable by tuning the driving frequency, the AC magnetic field amplitude, the DC bias magnetic field, or the DC bias electric field. Our multiferroic cantilevers are multi-mode switchable memory devices based on nonlinear mechanical vibration.

4.2 Nonlinearity: the Origin of Hysteresis

The cantilever driven by an external AC field is a damping harmonic oscillator driven by a periodic force. Its equation of motion is described by the Duffing equation

$$m\ddot{x} + \frac{m\omega_0}{Q}\dot{x} + m\omega_0^2x + k_3x^3 = F_0\cos(\omega_{\text{driving}}t + \phi), \quad (4.1)$$

, where m is equivalent mass of the cantilever, x is deflection of the cantilever, ω_0 is resonant frequency ($2\pi f$), k_3 is nonlinear factor, F_0 is external force amplitude, ω_{driving} is driving frequency ($2\pi f$), and ϕ is driving phase.

It is a normal linear damping oscillator driven by an external periodical force plus a nonlinear Duffing term k_3x^3 .

When the driving force is small, the deflection is so small that this Duffing term is negligible. In this regime, the cantilever behaves as to a normal damping oscillator, this is the regime described in Chapter 3. However, now if the driving force is increased, the Duffing term will need to be taken into account.

Fig. 4.1 gives an idea as to how the Duffing term affects the frequency response of the cantilever. When k_3/m from Eq. (4.1) is not zero, either being negative (-0.002) or positive (0.03), the frequency response shows a bistability regime where the Duffing oscillator can have two possible solutions in amplitude at a frequency near the resonance. This bistability gives rise to a hysteresis response when the frequency is swept in measurement. In Fig. 4.1, the dashed brown line shows frequency response with increasing frequency, while the dashed blue line shows the frequency response in the reversed direction. The frequency responses in the two opposite directions overlap with each other at the low frequency area and the high frequency area. However, the two separate around the resonant frequency, where the bistability exists. For instance, consider the blue curve with $k_3/m = 0.03$, the sign of the coefficient k_3 determines which direction the peak of the frequency scanning curve would tilt. When k_3 is positive, the peak tilts to the right, which corresponds to hardening of the cantilever as the resonant frequency is increased. When k_3 is negative, the peak tilts to the left, which corresponds to softening of the cantilever as the resonant frequency is decreased. When k_3 is zero, the cantilever has a Lorentzian peak, and there is no nonlinearity. Furthermore, when we compare the amplitude curve of $k_3/m = -0.002$ with that of $k_3/m = 0.03$, besides that the two curves tilt to the opposite

side, we found that the curve with $k_3/m = 0.03$ tilts more than the curve with $k_3/m = -0.002$. This indicates that the curve with higher absolute value of k_3/m has more nonlinearity.

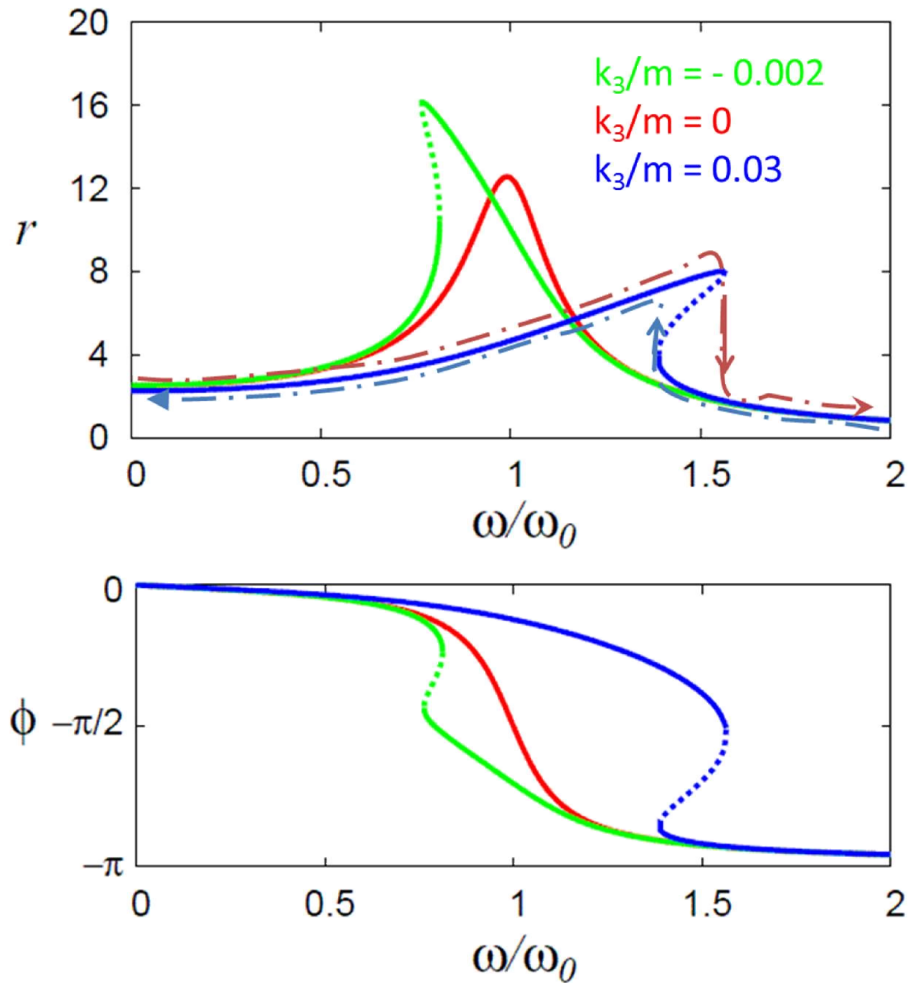


Fig. 4.1 Numerical simulation of amplitude and phase as a function of the driving frequency of a Duffing oscillator. Different colored curves are the simulated response with different value of k_3/m , which is -0.002 , 0 , and 0.03 , respectively. Dashed brown/blue line sweeps frequency in the increasing/decreasing directions. The figures are taken from [122].

Another way of understanding the Fig. 4.1 is through the effective spring constant. The effective spring constant is the spring constant of Duffing Eq. (4.1) when it is treated in a classic way. In this way, $m\omega_0^2x + k_3x^3$ can be seen as the classical restoring force $k_{\text{effective}}x$, where $k_{\text{effective}} = m\omega_0^2 + k_3x^2$. Then, the change of k_3 is closely tied to the change of the resonant frequency f_r , given that f_r is proportional to $k_{\text{effective}}^{1/2}$. As a result, a positive k_3 will lead to the increase of f_r (blue amplitude curve tilts to the right), while a negative k_3 will lead to the decrease of f_r (green amplitude curve tilts to the left).

4.3 Electric-field Driven Mode

4.3.1 Nonlinearity and Hysteresis

Our multiferroic cantilevers can be driven by either an AC electric field or an AC magnetic field. Under an AC electric field, the piezoelectric PZT layer develops a strain due to the applied voltage, which drives the cantilever. With AC magnetic field, the magnetostrictive FeGa layer develops a strain due to the applied magnetic field, which drives the cantilever. However, when studying nonlinearity, we start with electric-field driven mode, which has been studied before [123]. The examples of magnetic-field nonlinearly driven cantilever are rare. Thus, we want first to study the electric-field nonlinearly driven to better understand the nonlinearity of our device in a more predictable way. The magnetic-field nonlinearly driven mode was investigated after electric-field driven mode, and it will be discussed later.

Fig. 4.2 shows the circuit diagram with which the measurement was taken in this model. As Fig. 4.2 shows, a voltage source is equally shared by the two branches with C_v (variable capacitor) and C_s (stray capacitance), respectively. As we minimize the current reading in lock-in amplifier by tuning the variable capacitor, the balance of the current bridge is reached. In this

manner, then the stray capacitance (~ 3 nF) is canceled by the variable capacitor. This leads to a large background signal deduction and an enhanced signal to noise ratio. The readout in Fig. 4.2 is read by the lock-in amplifier, which is locked to the driving source – the function generator. It reads the net current signal from the two branches.

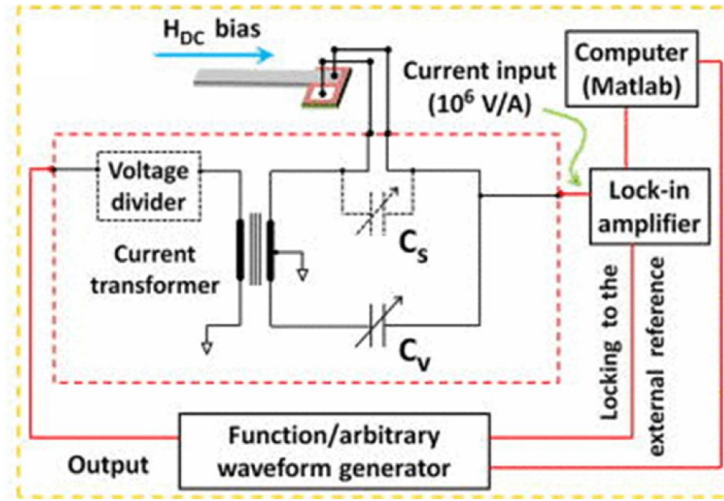


Fig. 4.2 Schematic of the electric-field driven mode, where a current bridge is used to cancel the stray capacitance.

First, we check if the device can be driven nonlinearly. The Duffing oscillator response in Fig. 4.1 is verified by experimental data in Fig. 4.3. The cantilever was driven by a voltage applied to the PZT layer, and current data is taken by a lock-in amplifier. At each voltage, frequency is swept from 3832 Hz to 3842 Hz. Fig. 4.3 shows that as we increase the driving field voltage from 50 mV to 275 mV with a 9:1 voltage divider, the frequency scanning curve evolves from a symmetric Lorentzian curve to an unsymmetrical inclined curve. The resonant peak tilts to the right hand side, indicating that our device has a positive k_3 factor in Eq. (4.1).

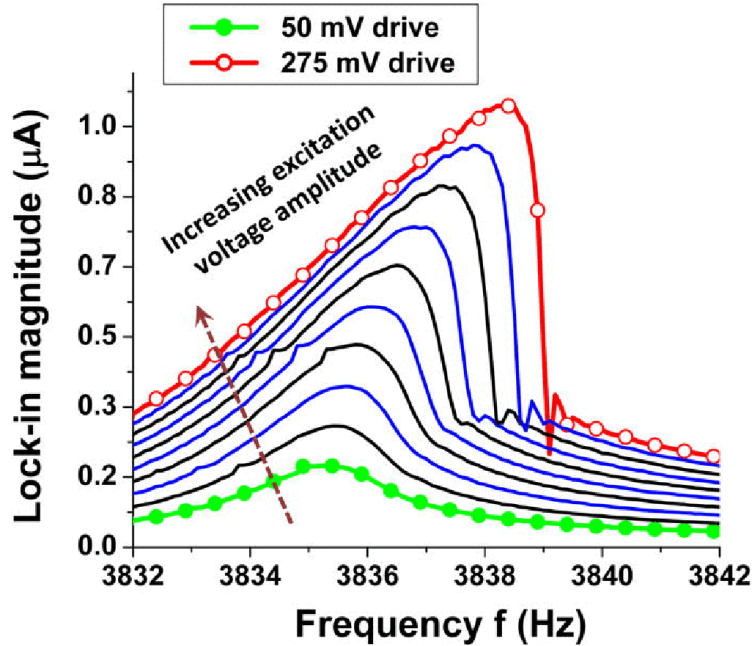


Fig. 4.3 Experimental data: Increasing driving excitation leads to nonlinear tilting of frequency scanning curve. All the curves were recorded in increasing frequency direction.

After seeing the evolution from linear to nonlinear by increasing driving electric field, next we investigate the bias magnetic field dependence in both increasing frequency scan and decreasing frequency scan. Fig. 4.4 (a) is the increasing frequency scan, which shows a broadened and tilted peaks with higher amplitude compared to Fig. 4.4 (b). On the other hand, the decreasing frequency scan has much more narrow peaks with lower amplitude. The DC bias magnetic field still leads to the resonant frequency shift with the change of the shifting direction at the coercive field of FeGa due to the reverse of magnetization. This is similar to the behavior shown in Chapter 3, Fig. 3.6. In the experiment shown in Fig. 3.6, AC driving force was due to AC magnetic field, and there was a DC bias magnetic field. Here, the AC driving force is due to the AC electric field, but there is still a DC bias magnetic field. In the present case, the shape of the device signal peak is not affected by the DC bias field. The former is reasonable because

even though the cantilever is driven by electric field, there is still a magnetic layer modulating the stress on the cantilever through the Zeeman energy and the anisotropy energy, as we discussed in Chapter 3. For the latter phenomenon where there is no DC bias dependence in the peak signal shape, it is due to the fact that the cantilever is driven purely electrically so that there is no magnetostriction involved, thus the driving force is not affected by the DC magnetic bias field. This is different from the cases of magnetic field driven, both the linear case that we have discussed in Chapter 3 and the nonlinear case that we will discuss later in this chapter. In magnetic field driven mode, the intensity of the magnetoelastic (ME) signal depends on the DC magnetic field, because both the magnetostriction λ and the magnetoelastic sensitivity ($\frac{d\lambda}{dH}$) are functions of DC magnetic field, which we have discussed in Chapter 2. However, in this electric-field driven mode, the intensity of piezoelectric signal will not be affected by the DC magnetic field.

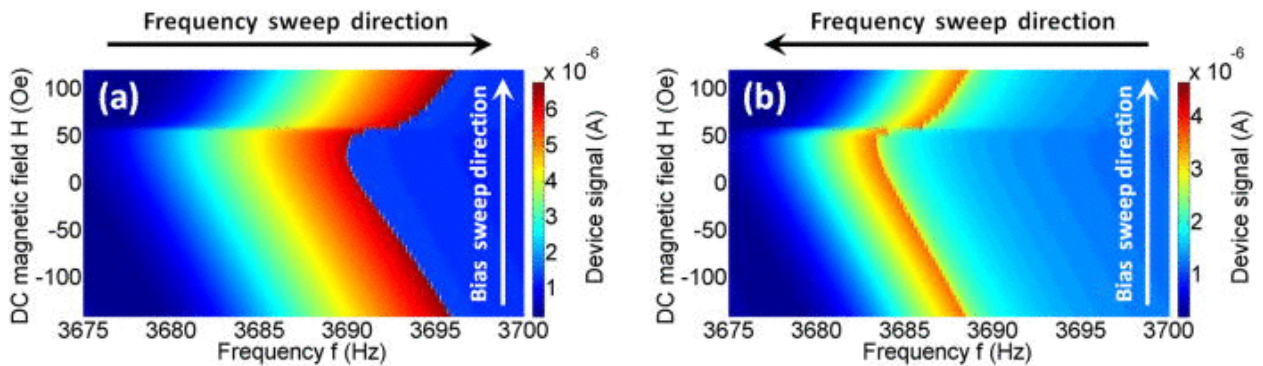


Fig. 4.4 Electric-field driven mode: Intensity plot of the frequency response in increasing direction (a) and decreasing direction (b), with varying DC bias magnetic field. We first sweep the frequency, then the DC magnetic field.

4.3.2 Switchable Memory Based on Nonlinear Mechanical Vibration

Now we have a cantilever that gives a hysteretic driving frequency response when it is driven with a strong electric field. The hysteresis can be the basis of a memory device. The ferromagnetic hysteresis is the fundamental basis of magnetic memory devices such as hard drive disks and magnetoresistive random access memory (MRAM). The ferroelectric hysteresis has also been studied for a long time for ferroelectric random-access memories (FeRAM)[124]. Multiferroic materials, which have both ferroelectric and ferromagnetic properties, are promising in applications of a new type of memory devices whose magnetic domains can be electrically controlled [125]. There are also memory operations based on mechanical states of systems. For instance, memories based on mechanical states of single-wall nanotube systems have been demonstrated with areal density exceeding the superparamagnetic limit of magnetic hard drive disks (100 Gbyte/in²) [126]. There are also demonstrations of mechanical memories based on double clamped beams, whose bistability arises from Duffing oscillations [127,128]. Researchers have also demonstrated mechanical memory operation of bistable cantilevers placed on a mechanical shaker using an optical read-out [123]. In our case, our multiferroic cantilevers are totally new for such applications. The nature of the multiferroic properties makes the cantilever a possible multi-mode memory device. We will characterize our multiferroic cantilever for such application in the next few sections.

If we overlap the frequency response of our device both from the increasing frequency direction and from the decreasing frequency direction at $H_{DC} = 0$ from Fig. 4.4, we obtain a cross-section plot shown in Fig. 4.5 (b), where the amplitude value is reflected in the readout of each point. As we can see in Fig. 4.5 (b), there is a large area of bistability with a bandwidth of 5 Hz. Outside of the bistability area, frequency responses in both directions overlap very well. In

other words, with driving frequency outside of the bistability area, the device will give a unique device signal readout, which is a current signal that represents the amplitude of the cantilever. When the device is driven within the bistability area, we can get two possible amplitudes depending on the mechanical amplitude level of the cantilever. These two amplitudes correspond to the two-solution states in Fig. 4.1 as we discussed previously.

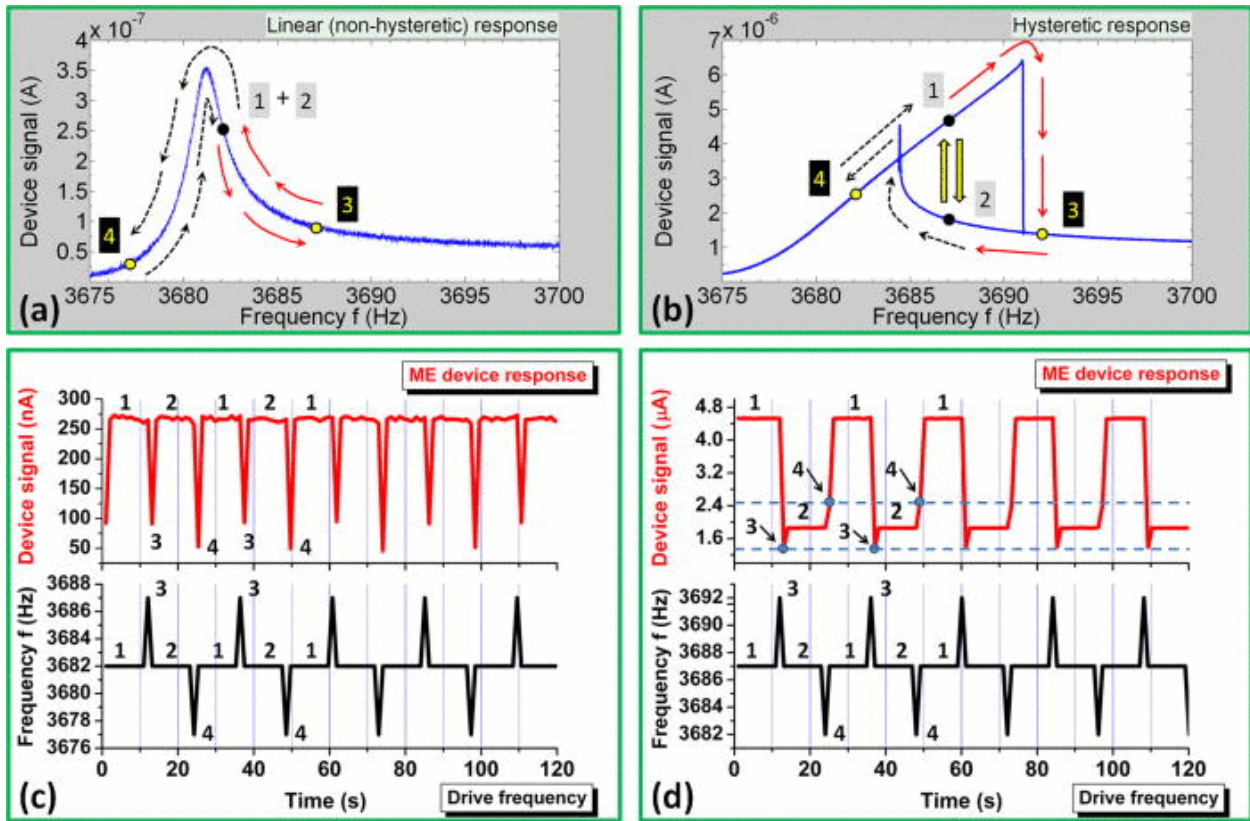


Fig. 4.5 Switching memory test triggered by tuning driving frequency for linear (a), (c) and nonlinear (b), (d) operation of multiferroic device with $H_{DC} = 0$. (a) Frequency response ME device under low voltage excitation (for 50 mV drive). (b) Frequency response ME device under low voltage excitation (for 1V drive). (c) Non-switching behavior of the device was found in the linear operation mode. (d) ME bistable response (red curve) triggered by a frequency pulse drive (black curve) in the nonlinear operation mode.

To better understand how the device behaves in the presence of this hysteresis and how it can be used as a memory device, let us look at some simple scenarios first. We start at State 4 in Fig. 4.5 (b), as we increase the driving frequency, the amplitude of the cantilever moves to State 1 instead of State 2. No matter how we increase or decrease the driving frequency, as long as it is less than 3691 Hz, where the frequency response falls off a cliff, the amplitude will stay in the upper branch with States 1 and 4. One can never reach a amplitude of State 2. However, once the driving frequency exceeds 3691 Hz, the amplitude will come down to the lower branch with State 3. At this point, no matter how you change the driving frequency, as long as it is higher than 3684.5 Hz, the amplitude will remain in the lower branch with States 2 and 3. To get back to State 1, one has to decrease the driving frequency beyond 3684.5 Hz, and then increase the driving frequency back to 3687 Hz.

On the other hand, in the linear case shown in Fig. 4.5 (a), one can change the driving frequency around the resonant frequency, but there are no such jumps of abrupt changes in amplitude.

What the State 1 and State 2 mean physically is the different oscillation amplitudes of the cantilever, even though the driving frequency is the same. Fig. 4.6 is a schematic drawing showing what the cantilever is physically doing at these two states.

This hysteretic behavior in frequency response can be used to switch the amplitude State between 1 and 2 by changing the driving frequency to beyond 3684.5-3691 Hz and bringing the driving frequency back to 3687 Hz. This can be achieved by modulating the driving frequency in pulses: we keep the main driving frequency to be well inside the hysteresis and apply pulses of high and low frequency drive voltages. The black curves in Fig. 4.5 (c) and (d) are the trigger

signal of the driving frequency. We therefore control the driving frequency, by a Matlab programmed function generator, to follow the equation:

$$f_{\text{driving}}(t) = f_{\text{ref}} + \Delta f \cdot \Pi [t - (10.5T + 2\lambda \cdot 10T)] - \Delta f \cdot \Pi [t - (21.5T + 2\lambda \cdot 10T)], \quad (4.2)$$

, where $\Pi(t)$ is rectangular function, λ is integer, T is 1 second, data acquisition interval, f_{ref} is 3687 Hz, the center driving frequency, and Δf is 5 Hz, change of driving frequency used to take the system out of the bistability area.

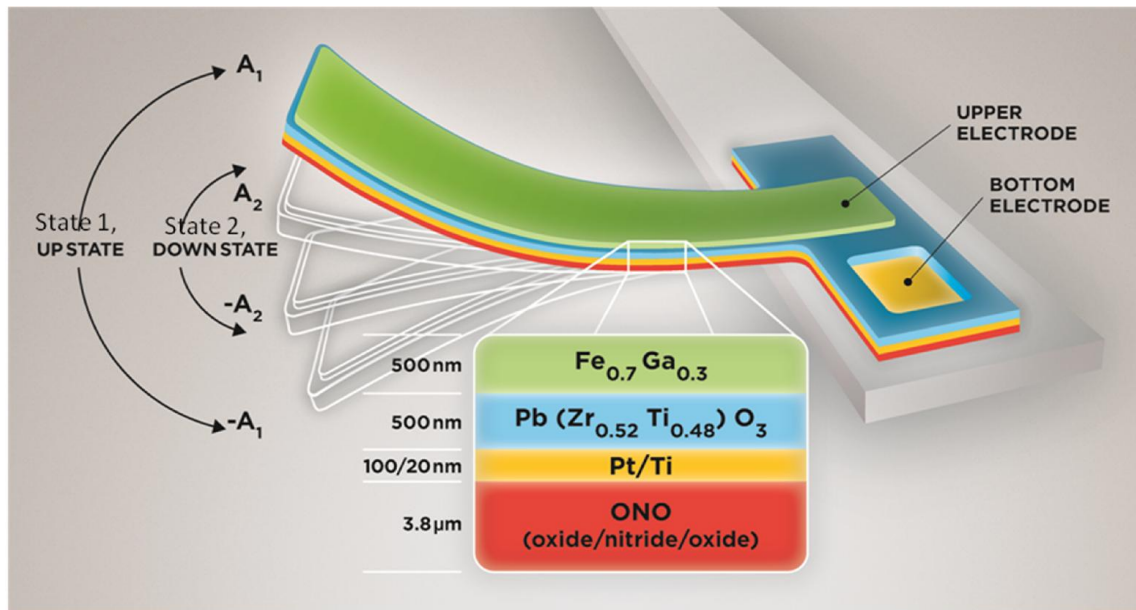


Fig. 4.6 Schematic figure of the cantilever, which can vibrate in two amplitude States at the same driving frequency. A cross-sectional schematic of the cantilever is also presented. State 1 is designated as the UP State and State 2 is designated as the DOWN State. From $-A_1$ to A_1 is the range of the deflection of the cantilever at State 1, while from $-A_2$ to A_2 is the range of the deflection of the cantilever at State 2.

As we apply the driving frequency change according to Eq. (4.2), we get the amplitude as a function of time series in red curves in Fig. 4.5 (c) and (d) for the linear operation mode and the

nonlinear operation mode, respectively. As one can see, in the nonlinear operation mode, the amplitude switches between State 1 and State 2, triggered by the driving frequency change. As we discussed before, this is because each time the driving frequency brings the device out of the hysteretic area and then bring it back to the original frequency, the amplitude switches between the upper frequency response curve with State 1 and the lower curve with State 2. However, for the linear operation mode, there is no hysteresis in frequency response, showed in Fig. 4.5 (a). As a result, the amplitude will always be the same after the triggered frequency change.

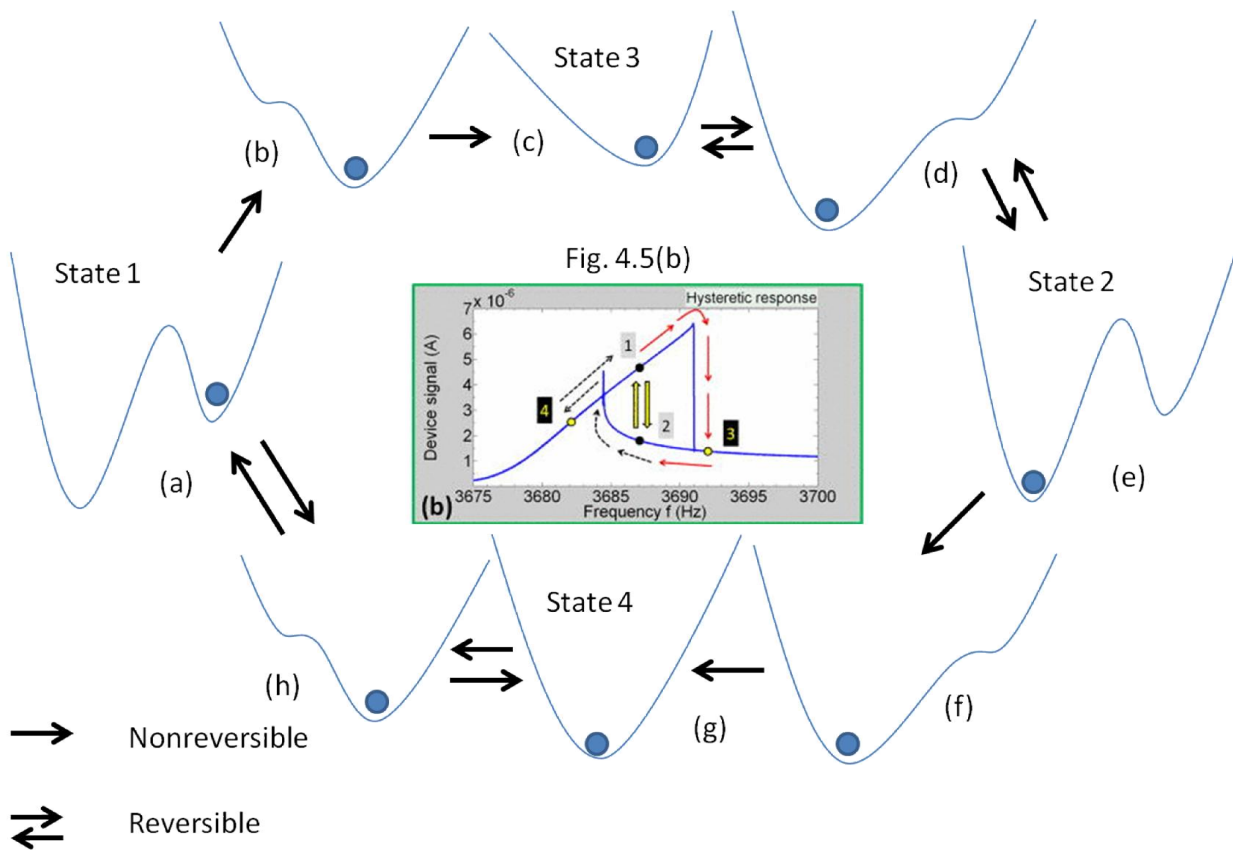


Fig. 4.7 Possible evolution of potential well due to tuning the driving frequency. (a), (b), (c), (d), (e), (f), (g) and (h) are potential wells of the cantilever, when the driving frequency is 3687 Hz, 3691 Hz, 3692 Hz, 3691 Hz, 3687 Hz, 3684.5 Hz, 3682 Hz, and 3684.5 Hz, respectively. The figure in the center is from Fig. 4.5 (b)

In the nonlinear operation, the cantilever system at its bistability area can be seen as operating under a double potential well. However, outside of the bistability area, the system is just in a single potential well. Fig. 4.7 gives a schematic evolution of this potential well of the system. As we stated before, the evolution between States 1 and 4 should be reversible, as they are both in the upper branch of the frequency response in Fig. 4.5 (b). The transition between States 2 and 3 is also reversible, as they are both in the lower branch of the frequency response in Fig. 4.5 (b). However, the system can only go from State 1 to State 3, not vice versa. Also, the system can only go from State 2 to State 4, not vice versa. We also find that the trigger signal sequence in Fig. 4.5 (c) and (d) is following the directional arrow in Fig. 4.7 so that the system is switched between State 1 and State 2 periodically.

4.3.3 The Role Magnetic Layer Plays in Electric-field Driven Mode

The magnetic layer can affect the overall frequency response curve through shifting of the resonant frequency (Fig. 4.4). In the nonlinear driving mode, the DC bias magnetic field does not change the shape of the hysteresis, but it can translate the hysteresis loop in the frequency response (Fig. 4.8).

As a result, the resonant frequency, where the switching process is taking place in Fig. 4.5, is tuned by changing the DC bias magnetic field.

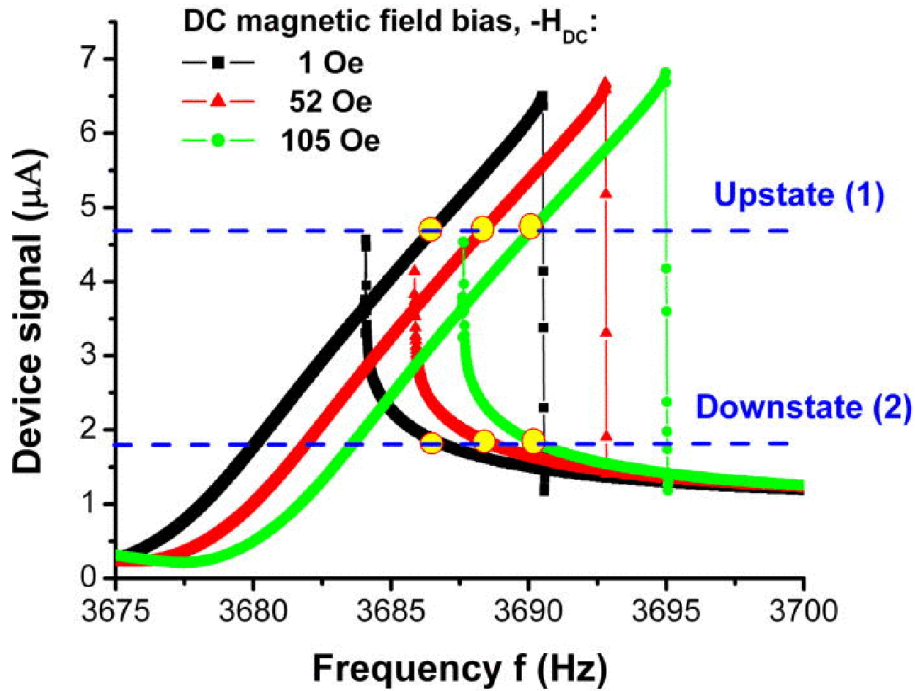


Fig. 4.8 Frequency-response hysteresis loop translation when different (H_{DC}) is applied.

4.3.4 Phase Diagram Analysis

The “phase space” (Fig. 4.9) is a common way to analyze the characteristics of a nonlinear oscillator in plotting its dynamics [129]. The phase space is used to analyze stability of chaotic systems, such as circuits [130] and pendulums [131]. The phase space is also used to characterize particles with in thermal dynamics [132]. It is the plot of momentum \mathbf{P} as a function of position \mathbf{x} . The trajectory as a function of time shows how a system evolves. In our device, the equivalent parameters for a phase diagram are device signal $S=S(f_{drive})$ and its derivative dS/df_{drive} (Fig. 4.9). We obtain our phase space plot where frequency (instead of time) is the key parameter. Then what we will see in such a phase space is how the system evolves as the frequency changes. By analyzing the phase space topology for different driving modes dictated by the direction of the frequency sweep, the device hysteretic behavior can be studied. It is particularly instrumental to

use the “phase space” representation in understanding the stability of device dynamics in different device circuit configurations.

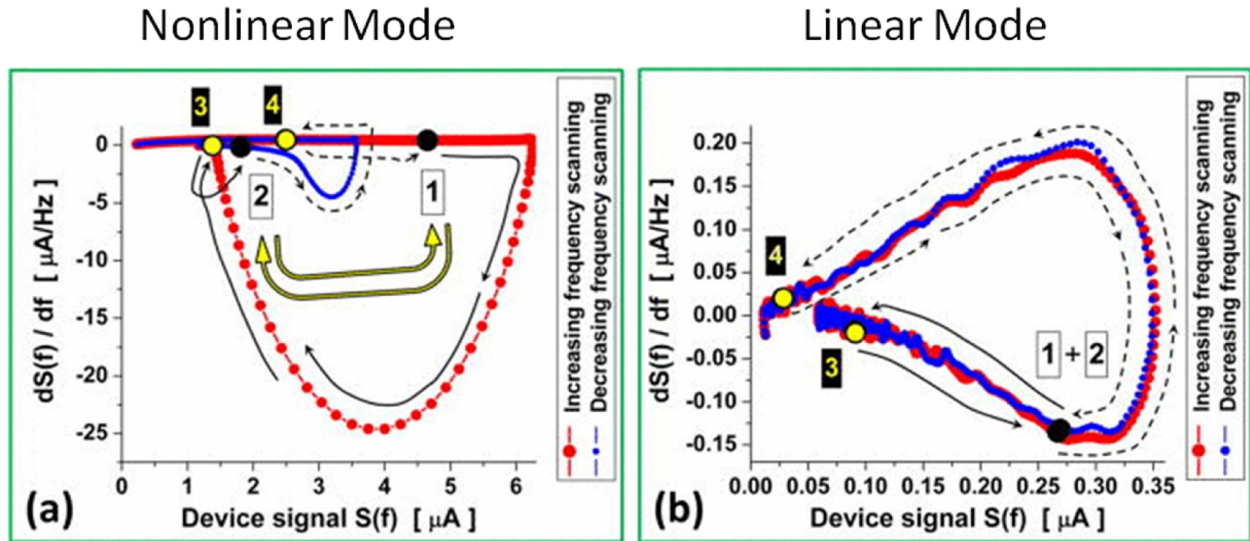


Fig. 4.9 Multiferroic cantilever dynamics in the “phase-space” representation at $H_{DC} = 0$. (a) Nonlinear mode. (b) Linear mode. The loops are not closed because we have limited frequency scan range in the experiments. The black arrows show the direction of the trajectories. The increasing frequency scan is clockwise, while the decreasing frequency scan is counter-clockwise. States 1, 2, 3, and 4 are the same States as in Fig. 4.5 and Fig. 4.7.

In the nonlinear case with high piezoelectric amplitude excitation (Fig. 4.9 (a)), the phase space trajectories are not symmetric to the Device signal axis, corresponding to the asymmetry in frequency response, where the peaks tilt to the higher frequency side. The two loops are also largely different, showing big hysteresis and bistability. The States 1 and 2, which are the two State on the bifurcation area in Fig. 4.5, are on different trajectories in Fig.4.9 (a), showing that the system cannot go directly from State 1 to State 2. Instead, from State 1 to State 2, one has to follow the red curve clockwise (increasing frequency) until the system reaches State 3. Then,

from State 3, the system has to go counter-clockwise following the blue curve (decreasing frequency) to reach State 2. Similarly, from State 2 to State 1, the system has to first follow the blue curve, moving counter-clockwise (decreasing frequency) until it reaches State 4. Then it moves clockwise following the red curve (increasing frequency) to reach State 1. In the linear mode (Fig. 4.9 (b)), the phase space trajectories are both symmetrical and almost overlap, indicating no hysteresis. There is no bistability in Fig.4.9 (b).

4.4 Magnetic-field Driven Mode

In Section 4.1-4.3, we discussed the behavior of the device where AC drive was achieved by applying an electric field to the piezoelectric film. We can also drive the device using AC magnetic field. Fig. 4.10 shows the comparison of butterfly curve intensity plot, the ME signal as a function of the driving frequency and the DC magnetic field, in the linear operation and nonlinear operation in AC magnetic driving mode. In these measurements, where both frequency and the DC magnetic field are swept, we first fix the DC magnetic field, and the frequency of the AC driving magnetic field is swept. The DC magnetic field is then changed and the AC frequency is swept again. In the linear mode (Fig.4.10 (a) and (b)), the device is driven by 1 Oe AC magnetic field with increasing or decreasing driving frequency. This is also the same data shown in Fig.3.8 (a). The DC magnetic field value is scanned downward in Fig.4.10 (a) and upward in Fig.4.10 (b). Here, the data taken while scanning the driving frequency in different directions are identical.

Fig.4.10 (c), (d), (e), and (f) are figures for the nonlinear mode, all with the same AC driving magnetic field of 8 Oe, but with different scanning directions of the driving frequency and the DC magnetic field. The dependence of the resonant frequency on the DC magnetic field and the

resulting magnetic hysteresis behavior were found in both the linear mode (Fig.4.10 (a) and (b)) and the nonlinear mode (Fig.4.10 (c), (d), (e), and (f)). However, hysteresis in driving frequency is also found in the nonlinear mode.

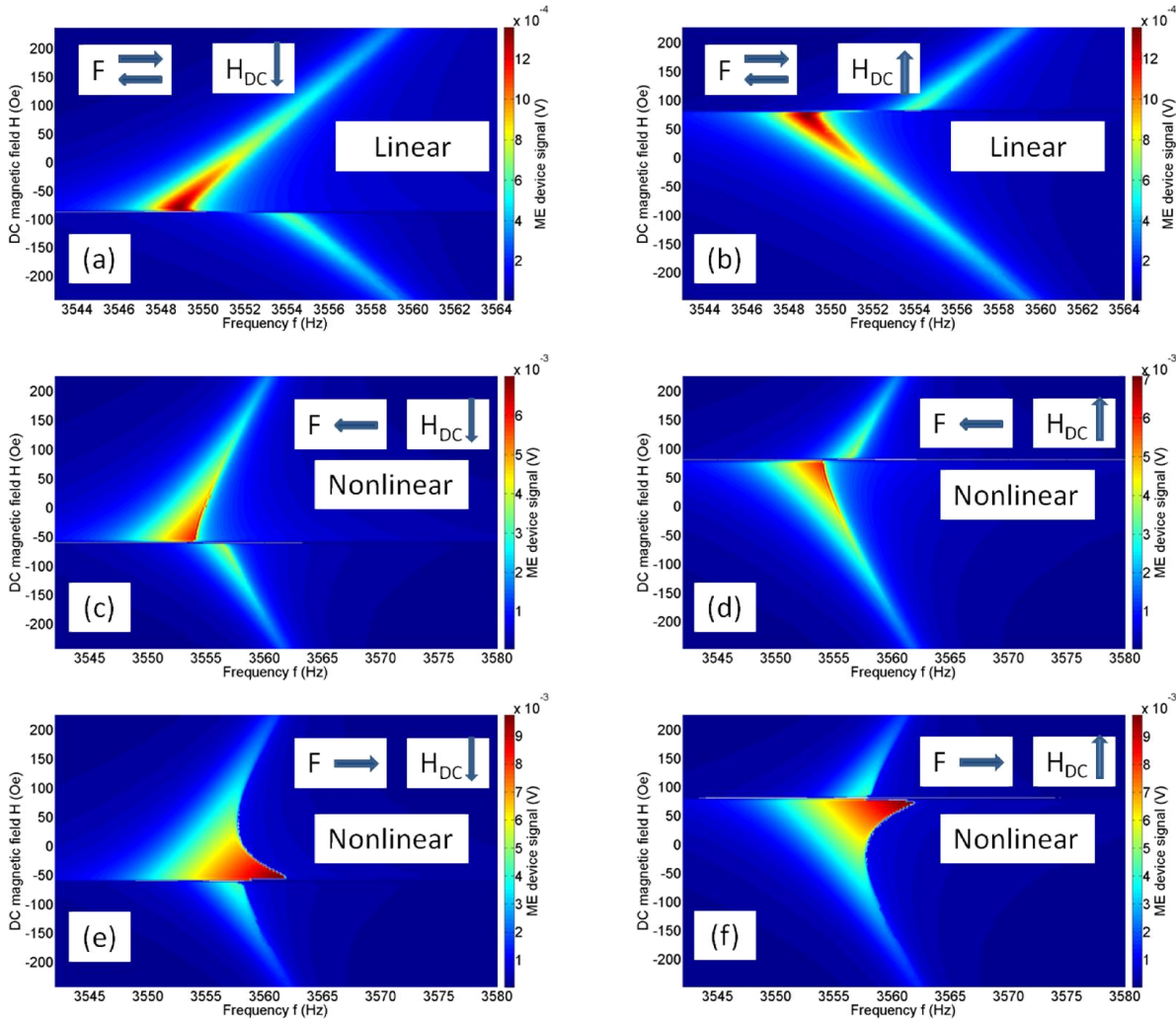


Fig.4.10 (a) and (b) are the ME signal as a function of the driving frequency and DC magnetic field in the linear mode with 1 Oe driving field, while (c), (d), (e), and (f) are in nonlinear mode with 8 Oe driving field. The measurement is taken in such a way so that the driving frequency is swept at a fixed DC magnetic field. Then the DC magnetic field is changed before the frequency is scanned again. And so on. The plots indicate that the symmetry in frequency response is broken by the nonlinearity.

Fig.4.10 shows that the characteristic intensity plots of the ME resonant frequencies as a function of the DC magnetic field are expanded from two plots into four plots for the nonlinear mode. This is because the nonlinearity breaks the symmetry in frequency response and generates the frequency hysteresis. By comparing plots where different responses are seen for different frequency scan directions (while the H_{DC} scan direction is kept the same), one can catch the glimpse of the occurrence of the frequency hysteresis. Comparison of Fig.4.10 (c) where the frequency is decreased with Fig.4.10 (e) where the frequency is increased (the H_{DC} scan is decreasing in both), show that the frequency hysteresis is tunable with changing DC magnetic field. The frequency hysteresis is at a maximum right before the interruption at 60 Oe, where the magnetization reverses. It is at a minimum when the H_{DC} amplitude is large in either the positive or the negative directions. The change in the frequency hysteresis region as a function of DC bias magnetic field (H_{DC}) is essentially due to the fact that the overall device response is still determined by how close it is to H_C the coercive field of the magnetic layer, as is the case in the linear driving mode (seen in Fig. 4.10 (a) and (b)).

4.5 How the Different Driving Modes Are Related

So far, we have introduced several different ways to drive the device as well as linear and nonlinear modes. It is of interest to look at the relationship between them. Here, three modes: E field driven nonlinear mode, B field driven linear mode, and the B field driven nonlinear mode are put together in Fig. 4.11, with the same scanning directions for the driving frequency and the DC magnetic field.

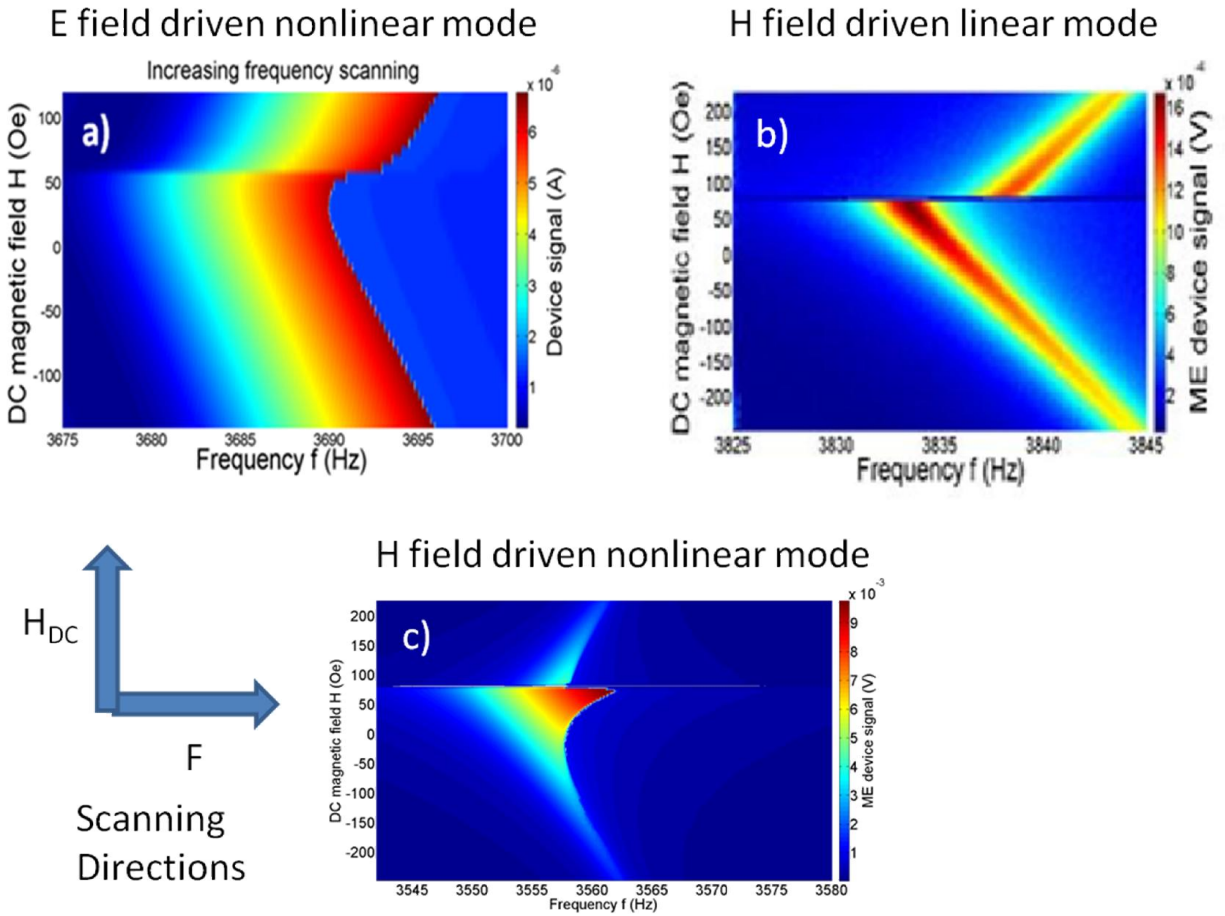


Fig.4.11 ME signal in E-driven nonlinear mode, H-driven linear mode, and H-driven nonlinear mode are presented in (a), (b), and (c), respectively.

What these three modes share in common are: first, the resonant frequency shifts with DC bias magnetic field; secondly, the change in the resonant frequency shows hysteresis as a function of DC magnetic field (not shown). Both of these phenomena were explicitly explained by our new theory based on the thin film model, in Section 3.6 in Chapter 3.

Now we look at the difference between these three modes. First, there are the electric field driven nonlinear mode (a) and the magnetic field driven nonlinear mode (c), which lead to the distorted resonant peak, while magnetic field driven linear mode (b) shows a symmetric

Lorentzian peak. This is due to the fact the two modes are driven with different amplitudes, and nonlinearity gives rise to the distortion in frequency response. Secondly, the electric driving mode in (a) shows a uniform peak in intensity across different DC bias magnetic fields, while in the magnetic field driven mode, for both nonlinear (c) and linear (b) modes, the ME signal changes due to the change of the DC bias magnetic field. This is because that magnetostrictive effect only takes place when the device is magnetically driven. As a result, the magnetic field-driven nonlinear mode (c) shows hysteresis behaviors in frequency response and shows a signal that depends on the DC magnetic field.

4.6 Multi-mode Memory based on Nonlinear Hysteresis

4.6.1 Memory Switch Mechanism

In this section, different switching mechanisms for our cantilevers are discussed in details. After studying the switching mechanisms, different triggering modes of the switch operation are proposed.

Previously, we showed in Section 4.3.2 that our device is switchable by changing the driving frequency periodically. The driving frequency is triggered by a pulse-like input as shown in Fig.4.12 (a). However, the switching parameter, the trigger signal, can be parameters other than the driving frequency. There are two types of switching mechanism that can lead to switching. The first type is the same mechanism when the AC electric-field driving frequency is used as the switching parameter. The switching using AC electric-field driving frequency as switching parameter was previously demonstrated in Section 4.3.2. With this type of switching mechanism, given a hysteresis loop of ME signal versus a switching parameter in Fig.4.12 (b), we can send a pulse like trigger signal in Fig.4.12 (a) to switch the memory bit to up or down. The other

switching parameters that also function based on the first mechanism are the AC magnetic field driving frequency and AC magnetic field driving amplitude. They will be discussed later in this chapter. The AC electric field driving frequency is also believed to be a switching parameter for this first mechanism, as it has been demonstrated [123].

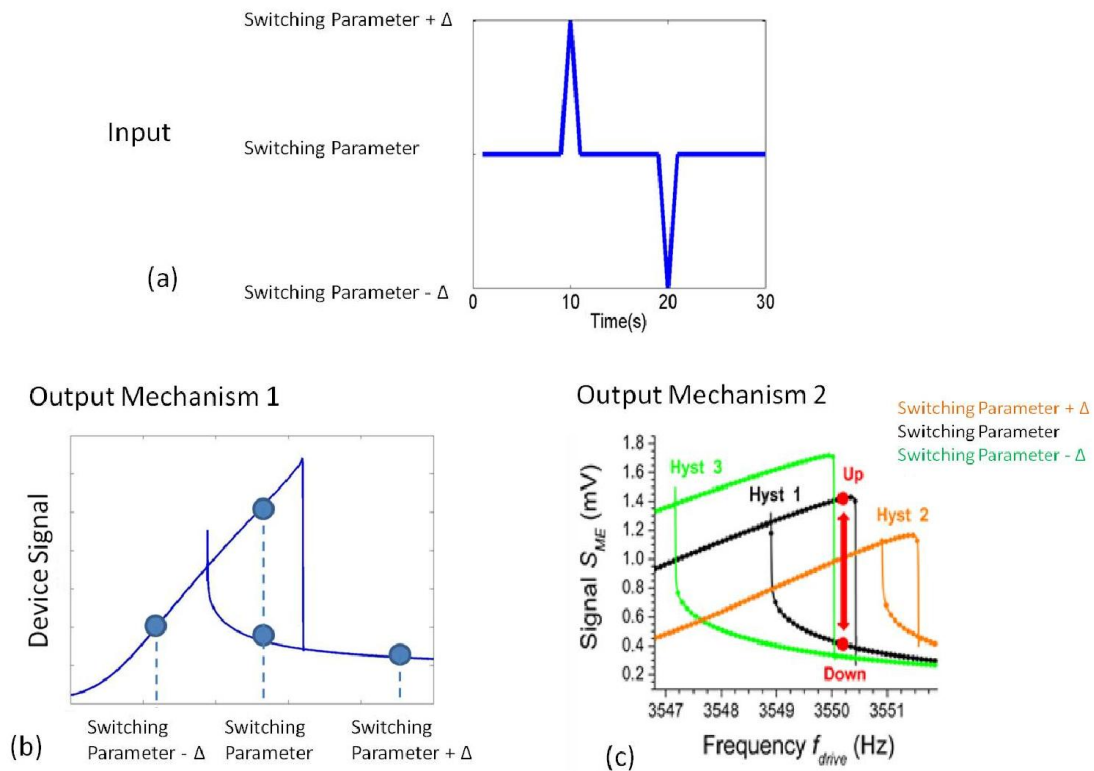


Fig.4.12 (a) Typical pulse like input, which changes the switch parameter, is used to trigger a switch (b) Switching mechanism 1: operation point moves along the hysteretic curve under the change of switch parameter, Δ . (c) Switching mechanism 2: frequency hysteresis loop moves under the change of switch parameter.

Another way to induce the switching behavior is presented in Fig.4.12 (c), where the change in the switching parameter triggers the change in the frequency hysteresis loop. In this case, the

driving frequency remains the same, while the frequency hysteresis loop shifts to the right hand side or the left hand side in frequency space depending on if the switching parameter has an upward pulse or a downward pulse. The shifted frequency hysteresis loop has to completely miss the driving frequency where the device is always driven so that the State can be switched effectively. The DC magnetic field and the DC electric field are such switching parameters that follow this mechanism, and they will be discussed later in this chapter.

4.6.2 Need for New Memory Devices

In Section 4.3.2 we showed that our devices can be used as a memory element triggered by pulses of different driving frequencies. A memory operated in this switching mode was found to work very well. But such a pulse as the input signal is not practical for real electronic devices. In the practical world, people like simple. In the magnetic hard drive disk, DC magnetic field is essentially what is triggering the ferromagnetic domains to switch. Nowadays, this process is considered to be too slow compared to solid state drives, because coils driven by electricity have to be used to provide the DC magnetic field, and the magnetic media has to physically spin under the read/write head so the head can access each memory bit. For a 7200 rpm hard drive disk, the average latency time is about 4.2 ms, which is how long the media spins half period. The need of rotation sets a bottleneck in access speed for hard drive disks. On the contrary, solid state drives whose memory bits are all directly accessible, are about four times faster in read and write [133]. For fast memory access, it will be ideal to have electric field directly triggering switchable memories. Progresses have been made using spin transfer torque device to write magnetoresistive random access memories (MRAM), which have read/write access times between 40 ns to 100 ns [134,135]. There have been a number of proposals to make memory

devices out of single multiferroic materials such as BiFeO_3 taking advantage of the fact that magnetism and ferroelectricity coexist in them, but to date, there have only been limited progress in this front [136]. Here, we show that our multiferroic composite devices can be used to make memory devices switchable by DC magnetic field and/or DC electric field.

As we previously discussed in Sections 4.3.1 and 4.3.2, the switchability of our device arises from the nonlinearity in frequency response. In Section 4.6.1 we showed that any parameter that influences the resonant frequency change can be possibly used as a switching parameter for triggering the switching of the memory bit. DC magnetic field and DC electric field are two such switching parameters that will be discussed in the next section.

4.6.3 DC Magnetic Field or DC Electric Field Triggered Memories

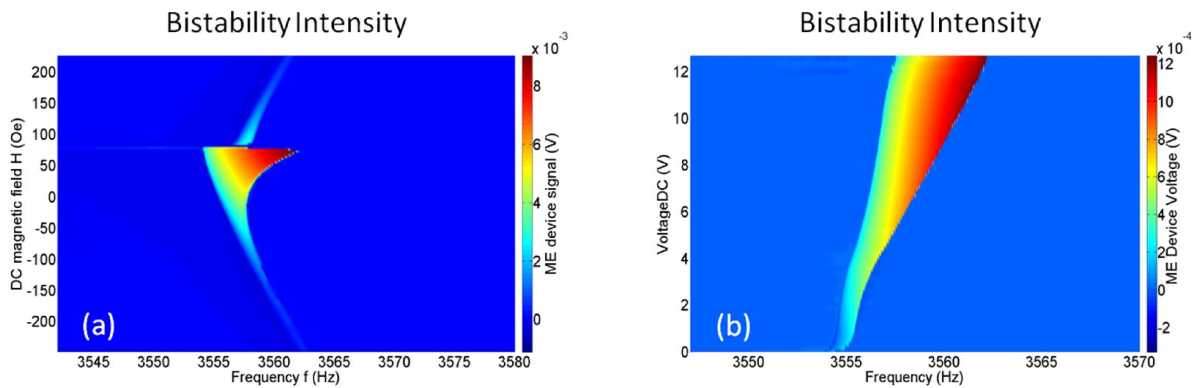


Fig.4.13 Bistability intensity in the frequency response as a function of (a) H_{DC} or (b) E_{DC} . A bistability intensity plot is the result of subtracting the decreasing frequency scan from the increasing frequency scan. Plot in (a) is obtained by subtracting Fig. 4.10 (d) from Fig. 4.10 (f).

To clearly see the location and the size of the frequency hysteresis region, which is the basis of bistability needed for memory operation, we subtract the decreasing frequency scan from increasing frequency scan. For example, by subtracting Fig. 4.10 (d) from Fig. 4.10 (f), we get

the bistability intensity Fig. 4.13 (a). Similarly, the bistability intensity for frequency as a function of E_{DC} is obtained (see Fig. 4.13 (b)). As we can see from Fig.4.13 (a), after subtracting signal of decreasing frequency scanning from signal of increasing frequency scanning, the bistability difference is a function of DC magnetic field. There is no bistability in most area in the figure except where it is around the resonant frequency. We can see the resonant frequency is also shifting with DC magnetic field, which we have been discussing in this thesis. At high DC magnetic field, the bistability intensity is very small for either sign of the field due to the low magnetoelectric excitation at high DC magnetic field. The bistability intensity increases, and its bandwidth widens as the DC magnetic field increases from negative 240 Oe to positive 75 Oe. However, it collapses as the DC magnetic field increases to more than 75 Oe, and magnetization is switched.

The bistability intensity as a function of DC voltage has a different behavior, as seen in Fig.4.13 (b). As the DC voltage is increased from 0 V to 12.8 V, the bistability intensity and its bandwidth both increases from none to maximum. Fig. 4.13 (b) shows experimental data obtained when a DC bias V_{DC} is applied in the device. The device dynamics becomes nonlinear when V_{DC} increases. An increasing frequency scan gives curves at different V_{DC} values that are non-Lorentzian, showing also a hardening of the device spring constant. Due to a different response when a decreasing frequency scan is applied, a resulting frequency hysteretic response (4.13 (b)) of the multiferroic device can be obtained by subtracting the map of decreasing frequency from the map of increasing frequency.

Similar to case that the resonant frequency shifts with H_{DC} , the resonant frequency also shifts with E_{DC} as shown in Fig. 4.13 (b). In the linear regime, a piezo-device shows a E_{DC} -dependent f_R that can be expressed as Eq. (4.3) (Ref. [137]):

$$f_{R, \text{electric}}(E_{\text{DC}}) \approx f_{R0} \left[1 + \frac{b_{\text{pf}}}{b} \left(\frac{d_{33}}{2} - \frac{1}{2} \frac{d_{311}}{s_{11}^E} \right) E_{\text{DC}} \right], \quad (4.3)$$

where f_{R0} is the device resonant frequency at zero electric field bias ($E_{\text{DC}} = 0$), b_{pf} is the thickness of the PZT film, and b is the total thickness of the cantilever. d_{33} is a piezoelectric coefficient, d_{311} is the nonlinear piezoelectric coefficient and s_{11}^E is the elastic compliance under constant electric field. For our devices, $d_{311} \sim d_{31} Y_{\text{pf}}$, where d_{31} is another piezoelectric coefficient and Y_{pf} is the Young's modulus of the piezo-electric film.

We have demonstrated the operation and switching of the memory device using DC magnetic field and DC electric field. Fig.4.14 shows that the device operation switched by pulse-like input of either DC magnetic field (Fig.4.14 (b)) or DC electric field (Fig.4.14 (d)). Fig.4.14 (a) and (c) show that the corresponding frequency response hysteresis changes under the change/application of H_{DC} and E_{DC} , respectively. As we discussed above as the second switching mechanism in Section 4.6.1, the driving frequency at which the device is always operating (black curve) is temporarily taken outside of the intermediate hysteresis loops (green or brown curves), which are the frequency response curves when the H_{DC} or E_{DC} are at the peak of the input curves in Fig.4.14 (b) or (d).

Using this principle, we have demonstrated reversible operations of a two-state multiferroic memory using input signals in the form of DC magnetic field H_{DC} (Fig.4.14 (a), (b)) or a DC voltage V_{DC} (Fig. 4.14 (c), (d)). An excitation H_{AC} of 428 A/m (RMS) is first applied along the cantilever to place it in the nonlinear regime. In Fig. 4.14 (a), we show the mechanism of switching between the two states when the DC magnetic field pulses are applied. In addition to the temporary translation of the hysteresis in the frequency space, there is temporary change in the hysteresis width as seen in Fig. 4.14 (a). With the initial condition of $H_{\text{DC}} = 0$ and $V_{\text{DC}} =$

8.1 V, the cantilever displays the hysteresis labeled Hyst 1 in the frequency space. The frequency of H_{AC} is selected so that it is inside the hysteresis loop.

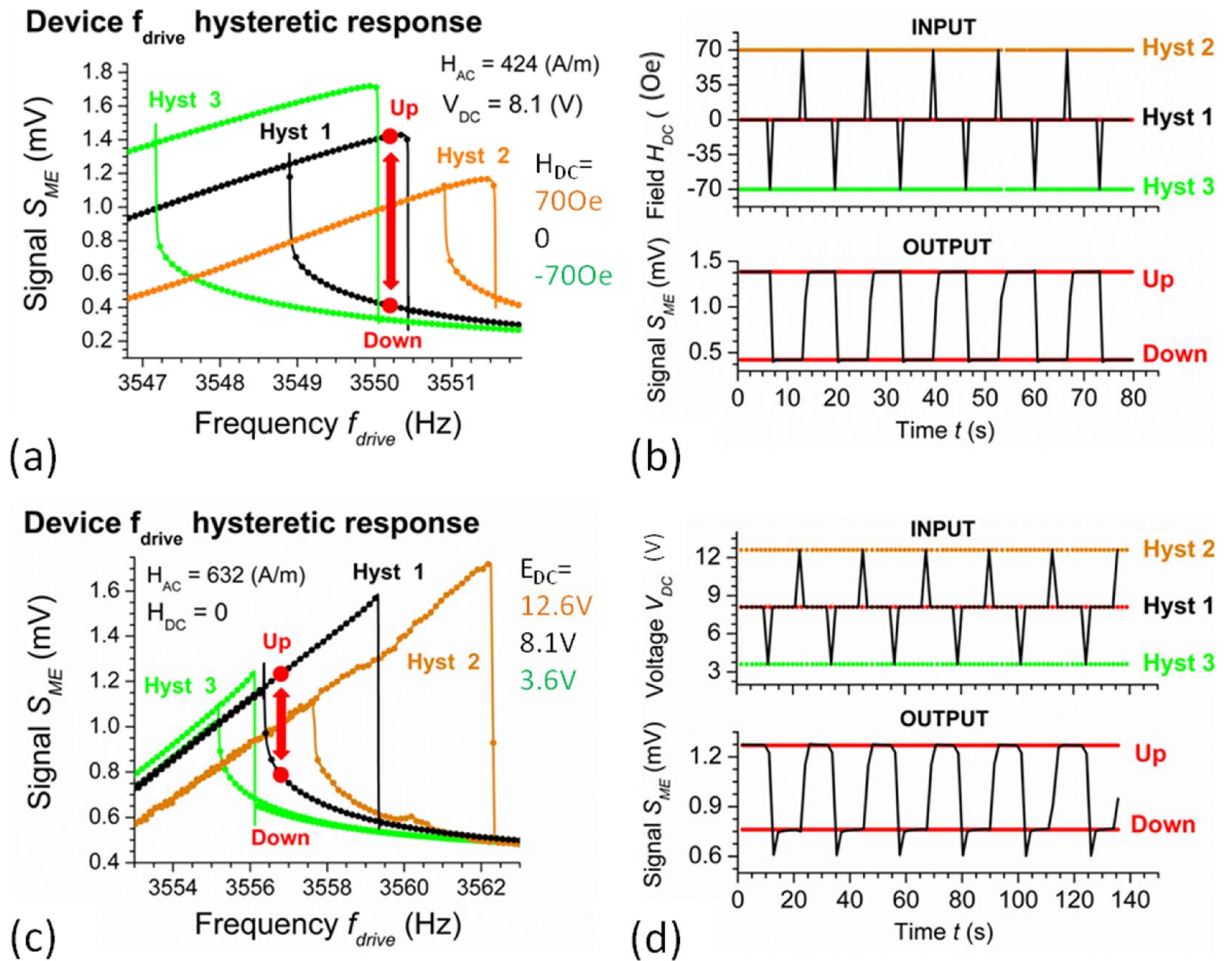


Fig.4.14 Operation of multiferroic memory using H_{DC} and E_{DC} as input. (a) Frequency response hysteresis changes with H_{DC} . (b) Device signal output is switched by H_{DC} input pulses. (c) Frequency response hysteresis changes with E_{DC} . (d) Device signal output is switched by E_{DC} input pulses.

Fig. 4.14 (a) depicts how the H_{DC} pulse results in the upstate switching to the down state and vice versa. Once the pulse of $H_{DC} = 5.6 \text{ kA/m}$ is applied (Fig. 4.14 (b)), the original f_R is temporarily in the intermediate range outside the envelope of Hyst 2. Upon returning to Hyst 1, the switching has now taken place, and the device is in its down state. To go back to the original state, we apply a DC magnetic field pulse of the same magnitude with an opposite sign: the hysteresis loop now shifts in the opposite direction as Hyst 3, and upon returning, the device is in its original state.

In fact, this gives us the guideline to choose H_{DC} , ΔH_{DC} , E_{DC} , and ΔE_{DC} to operate the device. In the experimental example we are showing in Fig.4.14, H_{DC} is chosen to be 0, and the change of H_{DC} , ΔH_{DC} is chosen to be 70 Oe. E_{DC} is 8.1 V, and ΔE_{DC} is 4.5 V. For example, if ΔH_{DC} or ΔE_{DC} is too small, the operating frequency can still remain inside the hysteresis in the intermediate pulse, and the device would not switch.

4.6.4 Frequency Modulation (FM) and Amplitude Modulation (AM) triggered Memory where FM pulses and AM pulses are interchangeable.

In Section 4.3.2, electric-field driven switchable memories triggered by pulse-like driving frequency input was discussed. Its output mechanism was explained in Section 4.6.1 using Fig.4.12 (b). In fact, the input of the memory, which is the trigger signal of up and down pulses, can be considered as a frequency modulation. In other words, our memory devices are switched by modulating the driving frequency. As we explained in Section 4.6.1, driving frequency hysteresis is the fundamental basis of our memory system. All the other switching parameters, such as H_{DC} , E_{DC} , and H_{AC} , rely on the fact that they are influencing the resonant frequency.

Thus the ME signal will show different hysteresis responses when H_{DC} , E_{DC} , or H_{AC} are tuned, and we can use them as our switching parameters.

Similar to frequency modulation, where the driving frequency can be modulated to be the input of our memory device, amplitude of AC magnetic field can also be modulated to be the input of our memories. As a result, the input can be either FM or AM with respect to the AC magnetic field.

Fig.4.15 (a) and (b) are the hysteresis response of the ME signal when the driving frequency and amplitude are varied, respectively. Fig.4.15 (c) or (d) are the figures showing the memory is switchable by either frequency modulation or amplitude modulation.

We also find that the FM and AM switches are interchangeable. The signals of ‘up’ States in FM switch and AM switch are at the same level. The ‘down’ States are at same level in both cases, too. Then it is natural to think if it is possible to switch the State from ‘down’ to ‘up’ by using frequency modulation and then switch it from ‘up’ back to ‘down’ using amplitude modulation. Fig. 4.16 shows the result of this demonstration. As we can see, the pulses of driving frequency and driving amplitude can both trigger the memory to switch. In fact, in this experiment, we have selected FM and AM pulses in such an order so that the signal is switched to the other State each time there is a pulse of either kind.

It needs to be mentioned that FM and AM triggered switches can also be accomplished with electric field.

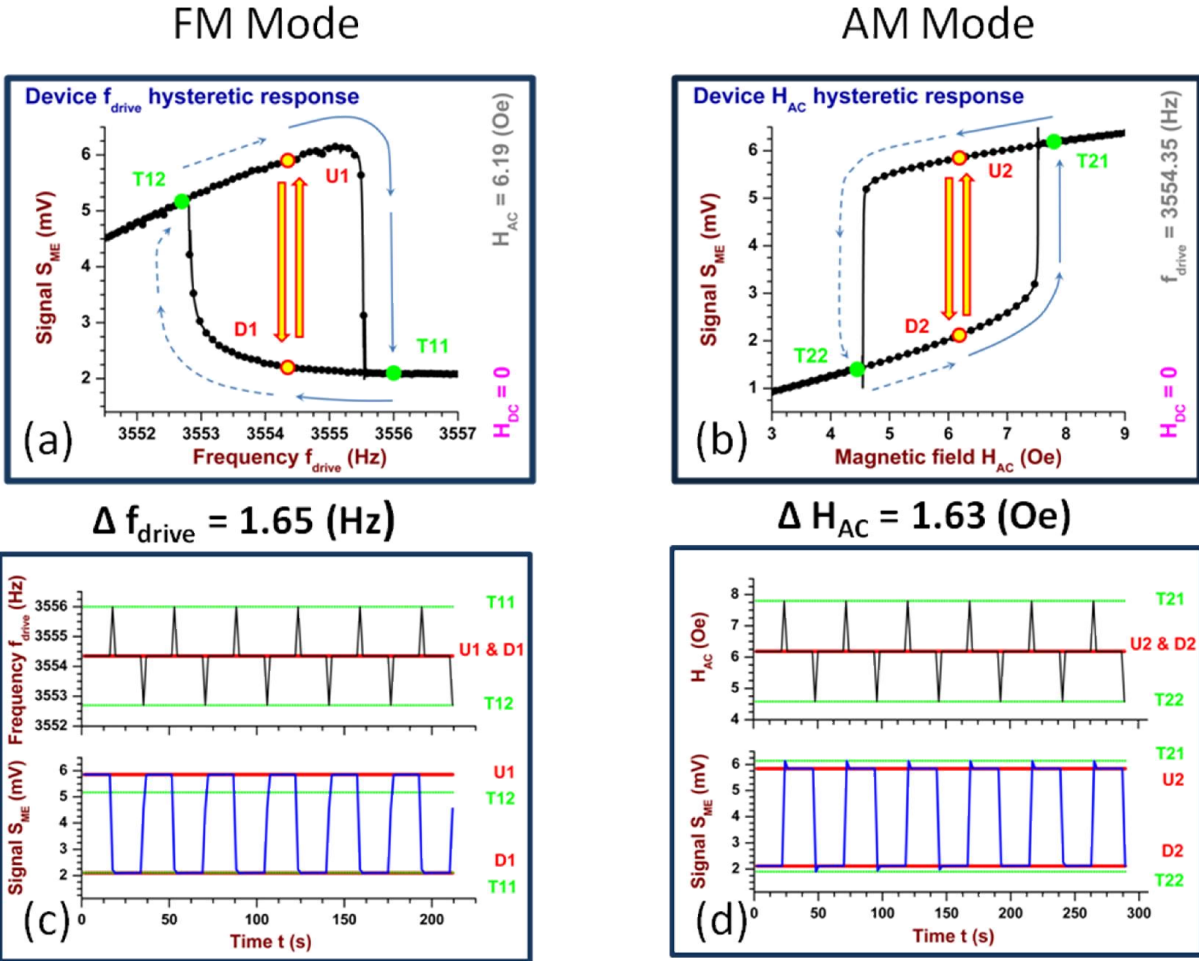


Fig.4.15 (a) Signal hysteresis in driving frequency response (b) Signal hysteresis in driving amplitude response (c) memory is switched by modulation in driving frequency (FM) (d) memory is switched by modulation in driving amplitude (AM). T11 and T12 are the intermediate States that the system is at when the ‘up’ and ‘down’ frequency pulses are applied in the FM mode, respectively. T21 and T22 are the intermediate States that the system is at when the ‘up’ and ‘down’ AC magnetic field amplitude pulses are applied in the AM mode, respectively. U1 and D1 are, respectively, the ‘Up’ and ‘Down’ States that the memory device is at when it is driven by the operation frequency of 3554.35 Hz in the FM mode. U2 and D2 are, respectively, the ‘Up’ and ‘Down’ States that the memory device is at when it is driven by the operation magnetic field amplitude of 6.19 Oe in the AM mode.

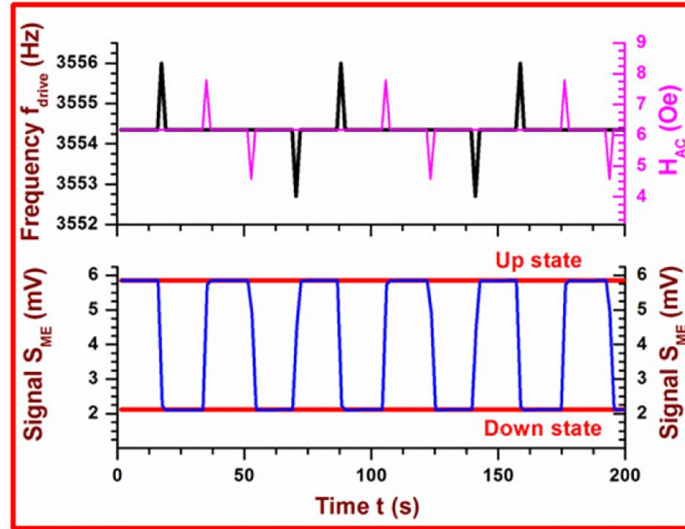


Fig.4.16 Interchangeable operation of frequency modulation and amplitude modulation modes.

4.7 The Size Effect

Our multiferroic cantilevers have been demonstrated to be dynamic mechanical memory devices. There are several advantages by going to smaller devices. First, smaller devices with higher resonant frequencies can switch faster. W. J. Venstra, *et al.* demonstrated bit operations with a $30 \mu\text{m} \times 8 \mu\text{m} \times 150 \text{nm}$ piezoelectric cantilever which has resonant frequency of 193.49 kHz [123]. The cantilevers need to have less than a few 100 nm length to achieve GHz resonant frequency [138]. The double clamped beams generally have higher resonant frequencies than the cantilevers with the same size [139], thus double clamped beams are preferred for this particular application. Secondly, by going to smaller devices, we can further increase the multiferroic materials/substrate materials ratio by reducing the substrate thickness so that the resonant frequency of cantilevers will be more sensitive to DC magnetic/electric field. This is verified by the experience of comparison between our small devices and big devices, as we mentioned earlier in Section 3.6. Last but not least, the smaller devices will need less power to operate, as

we can expect that both mechanical energy and magnetic/electric energy of the devices will be lower.

4.8 Conclusion

In this Chapter, nonlinearity of the multiferroic cantilevers was studied. Nonlinearity from the Duffing term in the equation of motion leads to a hysteretic frequency response using electric field or magnetic field as the driving source of the cantilever. The frequency hysteresis allows us to turn the device into a switchable memory whose states can be changed by modulating the driving frequency. Due to the fact that DC magnetic field, DC electric field, and AC magnetic (electric) field can all influence the resonant frequency, any of these parameters can be used as the primary input source for switching. The FM and AM mode are interchangeable in the switching process. DC magnetic/electric field triggered switches are promising dynamic memories whose switching speed can be greatly improved by going to smaller devices which have higher resonant frequencies.

Chapter 5: Colossal Magnetolectric Effect Assisted by Parametric Amplification

5.1 Abstract

In this Chapter, we describe the use of parametric amplification to substantially increase the magnetolectric (ME) coefficient of the multiferroic cantilevers. Parametric amplification has been widely used in sensing and actuating systems with optical or electric resonators [140-143]. While the cantilever is driven by AC magnetic field at the resonant frequency, by using a pump signal to modulate the spring constant of the system at double the resonant frequency, we are able to significantly increase the gain as the pump signal approaches the threshold value. The gain is also found to be sensitive to both the phase of the pump signal and the phase of the driving field. Using this method, the ME coefficient is amplified from 33 V/(cm × Oe) to 2,000,000V/(cm × Oe). The quality factor of the resonant frequency is also increased from 2300 to 70,000. This boost in the ME coefficient has directly resulted in magnetic field sensitivity of the device to improve from 6 nT/ $\sqrt{\text{Hz}}$ (discussed previously in Chapter 3) to 1 nT/ $\sqrt{\text{Hz}}$.

5.2 Parametric Amplification Theory

Parametric amplification (PA), also called parametric resonance, is a useful way to increase both the gain and the quality factor for most oscillator systems. It gives us an alternative method to actuate resonators. Traditionally, a driving force is applied directly on the resonators at the resonant frequency. However, in parametric amplification, a physical parameter (spring constant in most situations) of the system that is not the driving force is modulated as a function of time, which then modulates the response at the normal resonant frequency.

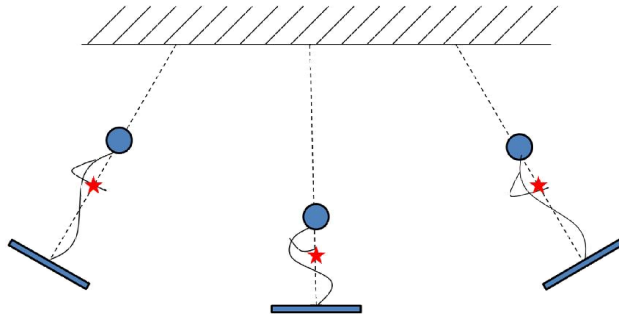


Fig. 5.1 (a) swing by changing center of mass

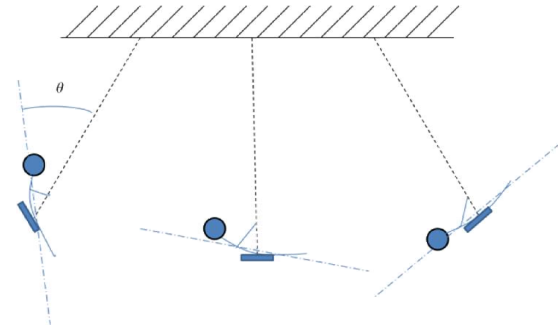


Fig. 5.1 (b) swing by rotating

Let us first look at parametric amplification using a simple phenomenological analogy, and then we will review its theory. The most common example in our daily life of parametric amplification is the swing motion. When a child moves up and down his body on a swing, he/she is parametrically modulating the resonant frequency by changing the center of mass periodically. Experienced swingers know to change their center of mass at double the natural frequency so that they can get the maximum amplification in swing (Fig. 5.1 (a)). However, the phase of the periodical motion of the center of mass is equally as important as the doubled frequency. To attain maximum amplification, swingers must raise the center of mass to highest level when the swing is at maximum height, and he/she must bend down to the lowest height when the swing passes the neutral position as seen in Fig. 5.1 (a). If the swinger does the opposite operation, rising up at the neutral position while bending down when swing is at the highest position, the swing amplitude is attenuated. From the energy point of view, the extra energy to increase the swing amplitude is pumped into the system by the up and down motion of the swinger. In addition to the standing mode in Fig. 5.1 (a), there is the sitting mode as shown in Fig. 5.1 (b). However, the sitting mode, in which the swinger rotates the body with respect to the swing periodically, is not parametric amplification, because the rotation acts as the direct drive, which

does not change the spring constant of the system. On the other hand, swinger in the standing mode modulates the spring constant of the system by adjusting the center of mass.

In a general parametric amplification system, the signal which modulates the natural resonant frequency of the system is called the pumping signal. The frequency of the pumping signal needs to be $2\omega_0/n$, where n is an integer and ω_0 is the angular resonant frequency (Fig. 5.2). However, it is most effective when $n=1$, and as a result pumping signal at $2\omega_0$ is most frequently used.

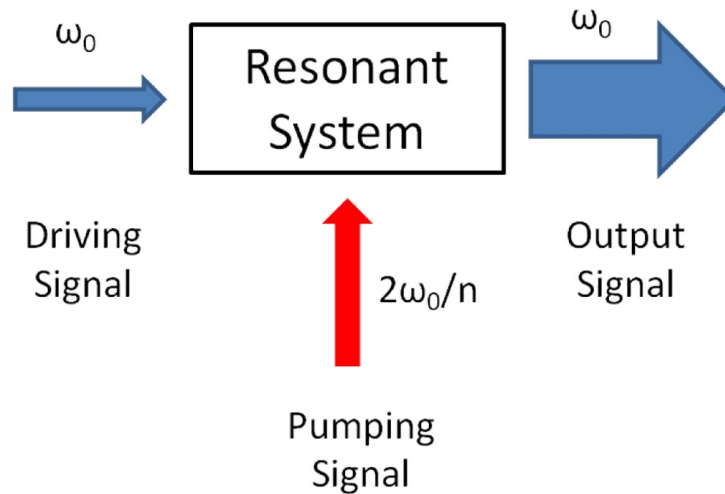


Fig. 5.2 Signal relation of parametric amplification

There are studies about how parametric amplification can help to sense and actuate piezoelectric systems with optical measurements [140,141] and MEMS integrate circuit resonators [142,143]. However, our work is the first work on the use of parametric amplification on multiferroic devices to the best of our knowledge.

In this Chapter, the parametric amplification technique is applied on heterostructured multiferroic cantilevers, which consist of 500 nm PZT, 500 nm FeGa, and 3.2 μm supporting an ONO stack and the Si substrate as described in Chapter 2. The piezoelectric PZT and

magnetostrictive FeGa are the functional layers that are the medium through which we are able to drive or pump the cantilever both electrically and magnetically.

For a resonant system, which is driven by an external periodical driving force at ω_{driving} and pumped by a pumping signal at $2\omega_{\text{driving}}$, we have the equation of motion,

$$m\ddot{x} + \underbrace{\frac{m\omega_0}{Q}\dot{x}}_{\text{classical}} + \underbrace{[m\omega_0^2 + k_p \sin(2\omega_{\text{driving}}t + \theta)]x}_{\text{pumping amplitude } \Delta k} + \underbrace{k_3 x^3}_{\text{Duffing term}} = \underbrace{F_0 \cos(\omega_{\text{driving}}t + \phi)}_{\text{driving force}}, \quad (5.1)$$

, where m is the equivalent mass of the cantilever, x is the deflection of the cantilever, ω_0 is the natural resonant frequency of the cantilever, Q is the natural quality factor without pumping signal, k_p is the pumping amplitude, ω_{driving} is the driving frequency of the driving force, θ is the pumping phase, k_3 is the Duffing coefficient corresponding to nonlinearity, F_0 is the amplitude of driving force, and ϕ is the driving phase.

The term $k_p \sin(2\omega_{\text{driving}}t + \theta)x$, which modulates the resonant frequency at $2\omega_{\text{driving}}$, is the signature term in parametric amplification. Without this term, the device behaves purely as a Duffing oscillator described by the equation of motion

$$m\ddot{x} + \frac{m\omega_0}{Q}\dot{x} + m\omega_0^2 x + k_3 x^3 = F_0 \cos(\omega_{\text{driving}}t + \phi) \quad (5.2)$$

We have discussed this Duffing oscillator behavior previously [144] and in Chapter 4, we showed how the frequency sweeping curves of the device can become distorted under high amplitude driving force. This is due to the fact that the Duffing term $k_3 x^3$ becomes prominent when the displacement is large enough. As we scan the frequency curves in both forward and backward directions, there is a hysteresis loop in the frequency space. As a result, by using the bifurcation of frequency sweeping, the device can be placed in a switchable memory regime, which can be controlled by a multimode input.

However, in this Chapter, let us first focus on the case when the displacement/amplitude is not so large that we can ignore the Duffing term for a moment. Instead, a pumping signal is added to the system. Then the equation of motion becomes

$$m\ddot{x} + \frac{m\omega_0}{Q}\dot{x} + [m\omega_0^2 + k_p \sin(2\omega_{\text{driving}}t + \theta)]x = F_0 \cos(\omega_{\text{driving}}t + \phi) \quad (5.3)$$

This is a Mathieu equation which has been solved by D. Rugar and P. Grütter, for the case of PZT cantilevers [141]. In their paper, with a high Q approximation, the parametric gain as a function of both driving phase and pumping voltage is calculated as

$$\text{Gain} = \frac{A_{\text{pump-on}}}{A_{\text{pump-off}}} = \left[\left(\frac{\cos\phi}{1 + \frac{k_p}{k_t}} \right)^2 + \left(\frac{\sin\phi}{1 - \frac{k_p}{k_t}} \right)^2 \right]^{\frac{1}{2}} \quad (5.4)$$

, where $k_t = 2m\omega_0^2/Q$.

However, if the pumping phase is also considered, the gain expression becomes

$$\text{Gain} = \frac{A_{\text{pumpon}}}{A_{\text{pumpoff}}} = \sqrt{\frac{1 + \left(\frac{k_p}{k_t}\right)^2 - \frac{2k_p}{k_t} \cos(2\phi - \theta)}{\left|1 - \left(\frac{k_p}{k_t}\right)^2\right|}} \quad (5.5)$$

, which can be reduced to Eq. (5.4) if the pumping phase $\theta = 0$. This gain expression (5.5) shows that the gain is sensitive to both the driving phase ϕ and the pumping phase θ , with a period of 180 degrees and 360 degrees, respectively.

Eq. (5.5) is maximized when $2\phi - \theta = 180^\circ + n \times 360^\circ$, for integer n, and it leads to

$$\text{Gain} = \frac{A_{\text{pump-on}}}{A_{\text{pump-off}}} = \frac{1}{\left|1 - \frac{k_p}{k_t}\right|} \quad (5.6)$$

while minimizes when $2\phi - \theta = n \times 360^\circ$, for integer n, giving

$$\text{Gain} = \frac{A_{\text{pumpon}}}{A_{\text{pumpoff}}} = \frac{1}{\left|1 + \frac{k_p}{k_t}\right|} \quad (5.7)$$

In Eq. (5.6), k_p is the pumping amplitude, which makes the maximum gain diverge when it approaches k_t . k_t is called the threshold amplitude, which is given by $k_t = 2 m\omega_0^2/Q$. We can also see from Eq. (5.7) that the minimum gain will always be smaller or equal to 1.

According to Eq. (5.5), with a fixed k_p/k_t ratio, , we can plot the gain as a function of the pumping phase θ and the driving phase ϕ as an intensity plot. This is plotted in Fig. 5.3. The k_p/k_t is 0.5 in this case. As we can see, in order to maximize the gain, it is important to choose the proper phases.

In our previous discussion in Section 1.3.2, we have mentioned that the figure of merit of ME devices is the ME coefficient. Researchers in the field of multiferroics are always working on increasing the ME coefficient. This is because a higher ME coefficient will improve the efficiency of the ME device in applications such as magnetic field sensors and energy transducers when the noise level stays the same. We also showed in Table 1.1 that the current progress in improving ME coefficients. The highest reported ME coefficient to the best of our knowledge is 20 kV/(cm \times Oe) [16]. Here, we see parametric amplification as a unique technique that can boost the ME coefficient with a phase sensitive gain, which diverges as the pumping amplitude approaches the threshold k_t .

The competition between the k_p and k_t can in fact be seen as the competition between the pumping amplitude and the friction force in the system. Thus, it is understandable that when the pumping amplitude is large enough to overcome the friction, the system is equivalently frictionless. As a result, significant increase of gain can be expected.

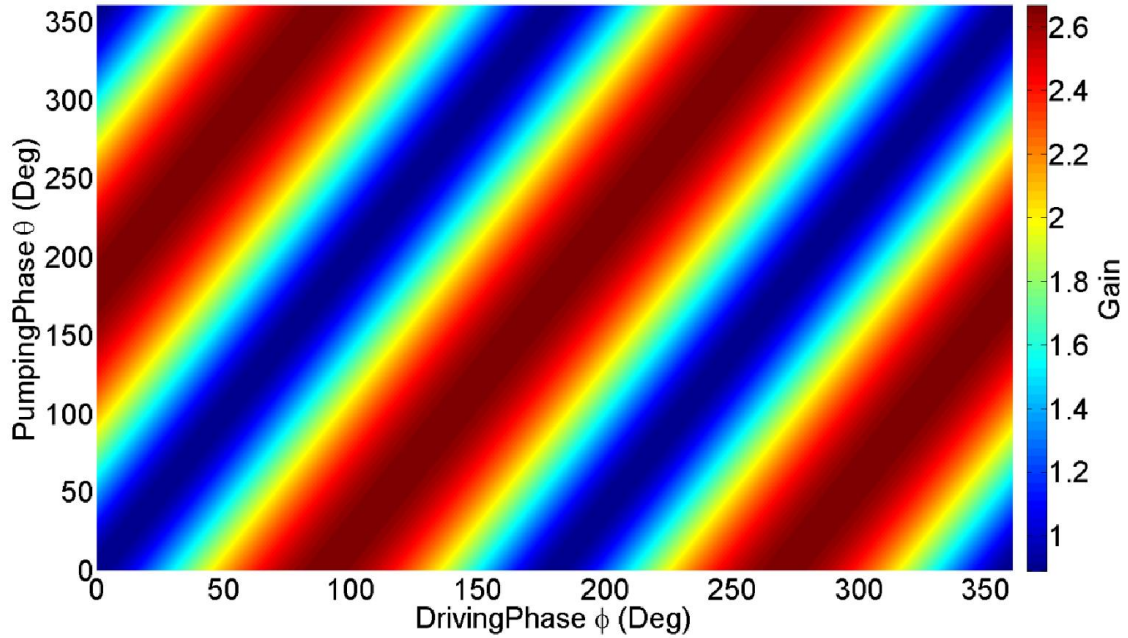


Fig. 5.3 Theory plot according to Eq. (5.5). Gain as a function of pumping phase θ and driving phase ϕ , for $k_p/k_t = 0.5$.

5.3 Parametric Amplification Setup

Fig. 5.4 shows our experimental setup for carrying out the parametric amplification study. The multiferroic cantilever is mounted in a vacuum chamber with vacuum of around 5×10^{-7} Torr. As we have discussed in Chapter 2, our device has higher ME coefficient in vacuum than in air. A pair of Helmholtz coils is fixed outside of the vacuum chamber, providing the AC drive. In these measurements, we take the AC drive signal to be the main signal to be amplified. Indeed, in the magnetic field sensing application (discussed in Chapter 2), the AC drive signal is the field to be detected. Amplification of the signal to be detected will greatly facilitate the sensing operation and the sensitivity. The AC magnetic field is aligned with the cantilever. The coils and the vacuum chamber are surrounded by a rectangular Mu-metal shield box which sits on top of a sand box. This leads to the minimum magnetic noise above 20 Hz and the vibration noise from

environment to the cantilever. Considering the dimension of the cantilever ($950 \mu\text{m} \times 200 \mu\text{m} \times 0.5 \mu\text{m}$) is orders of smaller than that of the Helmholtz coils (10 cm diameter), the cantilever at the center of the two coils is in a very uniform magnetic field. The device mounting setup is basically the same as in previous chapters, but the differences are in external circuit wirings. The uniform driving magnetic field is at ω_{driving} , close to ω_0 , the resonant frequency of the cantilever. At the same time, the pumping signal in the form of electric field at $2\omega_{\text{driving}}$ is provided to the electric contacts on the PZT layer of the cantilever. The current signal is measured by a SR830 lock-in amplifier with the help of a homemade current-to-voltage-converter and a band pass filter. The two source function generators and the lock-in amplifier are all synchronized.

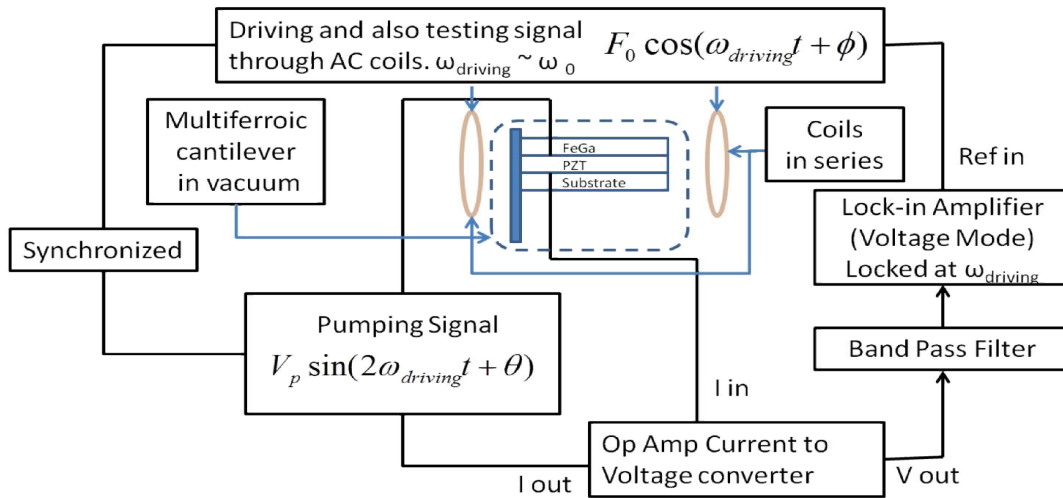


Fig. 5.4 Block diagram showing a multiferroic cantilever driven by magnetic-field drive signal at ω_{driving} , while its spring constant is modulated by the pumping signal at $2\omega_{\text{driving}}$. The response of the cantilever is then measured by a lock-in amplifier at ω_{driving} .

Now let us see how the pumping amplitude k_p can be expressed, considering the pumping signal is in the form of

$$V_{\text{pump}} = V_{\text{offset}} + V_p \sin(2\omega_{\text{driving}}t + \theta) \quad (5.8)$$

We know that Δk , which is the change of the spring constant in the system due to the pumping signal, on one hand can be calculated as

$$\Delta k = \frac{\partial F}{\partial x} = \frac{\partial^2 U_c}{\partial x^2} \quad (5.9) \quad , \text{ where } U_c = \frac{1}{2} CV_{\text{pump}}^2 \quad (5.10)$$

$$\text{On the other hand, } \Delta k = k_p \sin(2\omega_{\text{driving}}t + \theta) \quad (5.11)$$

$$\text{By keeping only } 2\omega_{\text{driving}} \text{ terms, with (5.8)-(5.11), we get } k_p = \frac{\partial^2 C}{\partial x^2} V_{\text{offset}} V_p \quad (5.12)$$

This means $k_p \propto V_p$, when $\frac{\partial^2 C}{\partial x^2} V_{\text{offset}}$ is treated as a constant.

We see that k_p can be controlled by simply tuning V_p . Eq. (5.6) then becomes

$$\text{Gain} = \frac{A_{\text{pump on}}}{A_{\text{pump off}}} = \frac{1}{\left|1 - \frac{V_p}{V_t}\right|} \quad (5.13)$$

$$, \text{ where } V_t = 2 m \omega_0^2 / Q \delta , \text{ with } \delta = \frac{\partial^2 C}{\partial x^2} V_{\text{offset}}. \quad (5.14)$$

5.4 Experimental Data

5.4.1 Measurement of the Phase Sensitive Gain

One of the most important characteristics of parametric amplification is that the gain is phase sensitive, as given by Eq. (5.6). As seen in Fig. 5.5, with the help of parametric amplification, the device signal and the gain are both periodically modulated by the pumping phase and the driving phase, with a period of 360 degrees and 180 degrees, respectively. The resonant frequency does not shift with variation in the pumping phase or the driving phase. Fig. 5.5 (c) and (d) are corresponding data of the gain as a function of pumping phase and driving phase, respectively. The periodic shape of gain curves matches the theory of the parametric amplification, as predicted by Eq. (5.5).

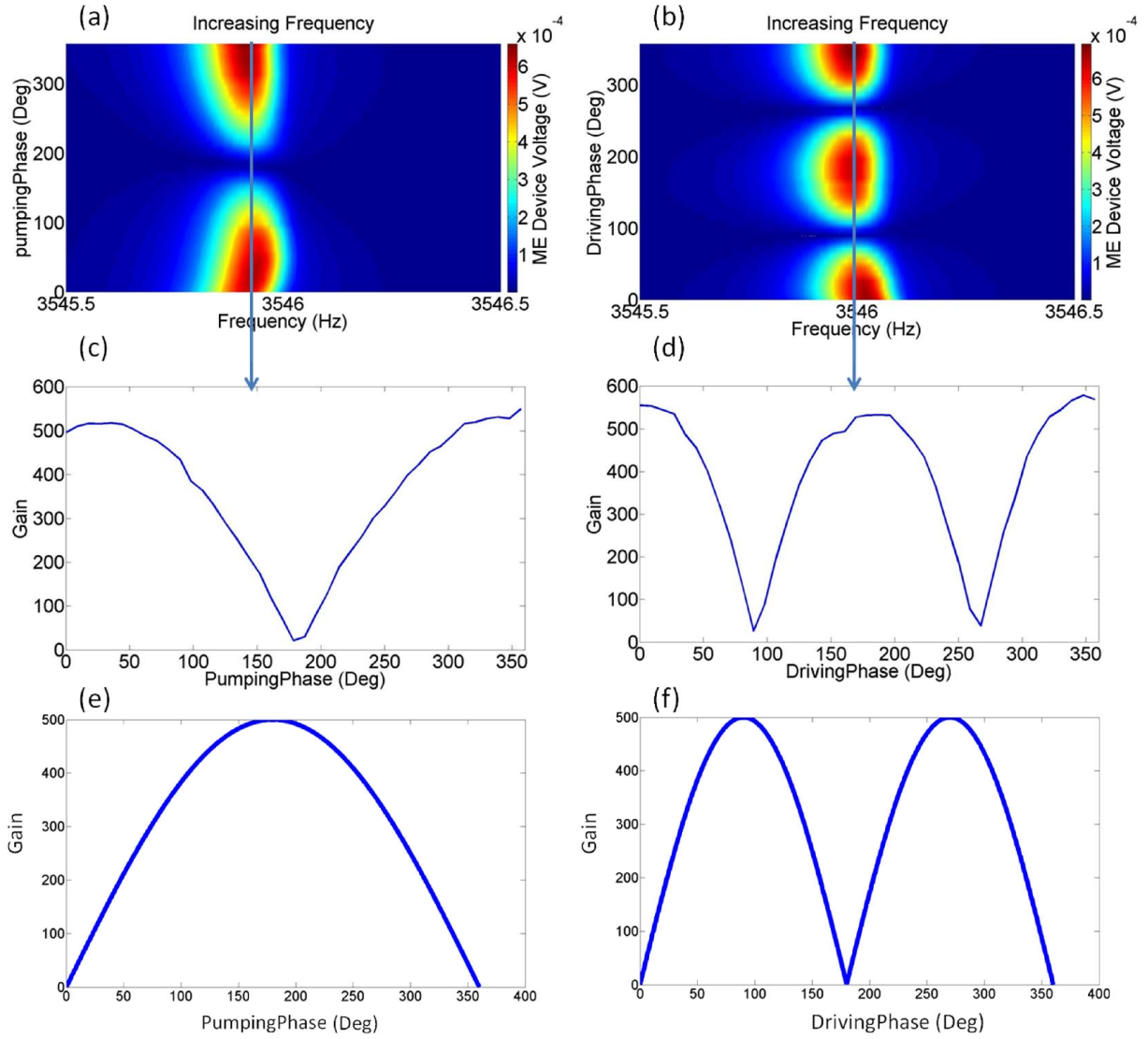


Fig. 5.5 (a) and (b) are frequency sweep of the ME signal vs pumping phase with driving phase set to zero and ME signal vs driving phase with pumping phase set to zero, respectively. (c) and (d) are cross-section images of (a) and (b) at the resonant peak frequency, respectively. Measurements were carried out with driving field of 257 nT and the pumping voltage of 1.16 V. (e) and (f) shows theory plot according to Eq. (5.5) for (c) and (d), respectively.

There is, however, a phase difference as to where the peak of the gain should be compared to the theory, as seen in the Fig. 5.5 (e) and (f). This is due to the intrinsic phase difference in our

system. With some phase corrections, the theoretical and experimental curves are in good agreement with each other.

As the gain is sensitive to both the driving phase and the pumping phase, if one wants to attain the highest gain out of the parametric system, he/she should carefully choose both of them so that the signal is maximized.

5.4.2 Nonlinear Increase of Gain with Pumping Voltage

In the experimental data shown in Fig. 5.6, the driving field is 257 nT (RMS). Gain data points were taken from a series of cross-sectional curves that are similar to Fig. 5.5 (c). As Fig. 5.6 indicates, the gain is amplified substantially as the pumping voltage gets close to the threshold voltage V_t . The maximum gain in Fig. 5.6 is nearly 1000 both in experiment and theory.

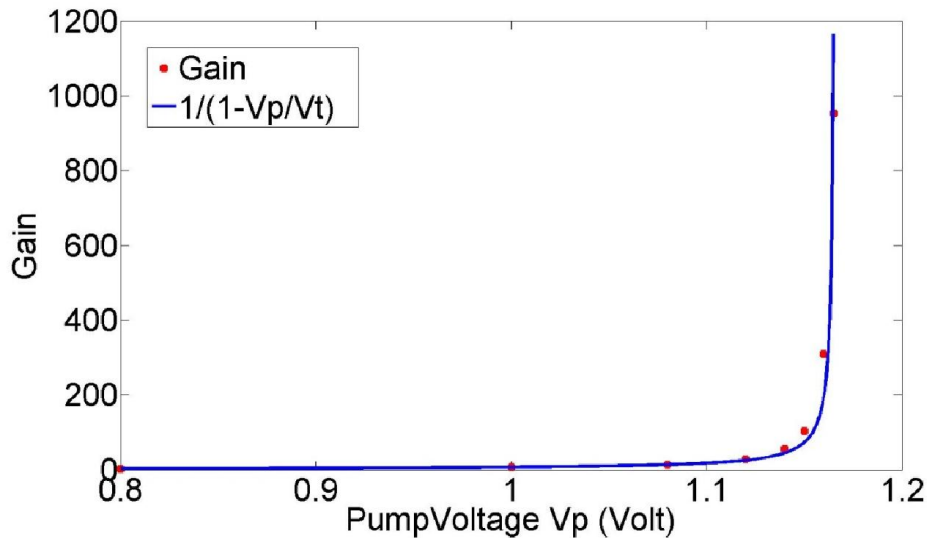


Fig. 5.6 experimental (red dots) and theoretical gain (blue solid line) are shown as a function of the pumping voltage. The theory curve is from Eq. (5.10) using $V_t = 1.166$ V.

In fact, with the threshold voltage as a fitting parameter, the theory predicted by Eq. (5.10) fits the experimental data so well when the $V_t = 1.166$ V. Because the ME voltage signal is amplified without changing the rest of the factors in the definition of the ME coefficient, such as the input magnetic field amplitude and the thickness of the piezoelectric layer, the magneto-electric (ME) coefficient of 33 V/(cm \times Oe) without pumping for a multiferroic cantilever, is then boosted to $33,000$ V/(cm \times Oe) as a result of pumping.

As previously introduced in the parametric amplification theory, gain diverges when the pump voltage is close to the threshold voltage. However, in reality, due to the onset of nonlinearity where the device becomes a Duffing oscillator, the amplified device signal will always start to saturate at around 0.4 mV no matter what the intensity of the driving magnetic field is. As a result, the higher gain and the ME coefficient is more easily achievable with lower magnetic driving fields. The curve with the 6.3 μ T driving field is amplified 100 times to get to 0.4 mV, while the curve with the 63 nT driving field can be amplified 10,000 to get to the same voltage level. The data points in Fig. 5.7 for curve of the 63 nT have significant uncertainties when the pump voltage is low. This is because the signal without pump or with low pump is already below the noise level of 2 μ V. However, referring to the 6.3 μ T curve, it is reasonable to assume that the signal without pump of the 63 nT curve should be 100 times lower than that of the 6.3 μ T curve. Thus we can say that the 63 nT curve is amplified 10,000 times by the parametric amplification. With amplification of 10,000 times, this corresponds to the ME coefficient of $330,000$ V/(cm \times Oe).

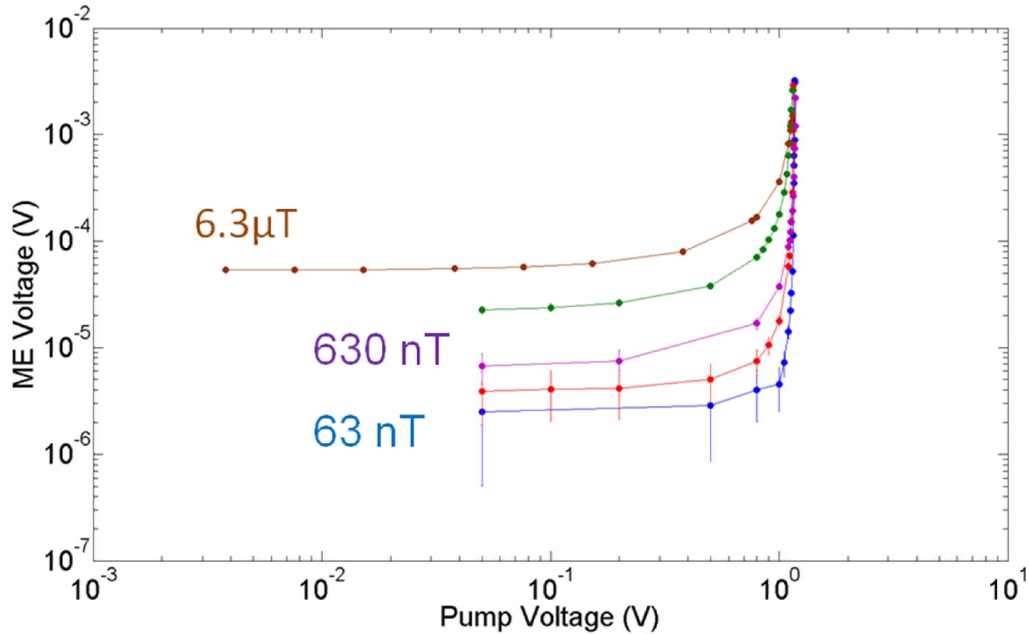


Fig. 5.7 The ME signals as a function of the pump voltage, with different driving fields (63 nT, 630 nT, and 6.3 μT are all in RMS).

As we can see in Fig. 5.8, the ME coefficient is so sensitive to the pump voltage that even 1 mV change in pump voltage will make significant difference in the ME coefficient. The signal changes three orders of magnitude with the change of pump voltage within 1 mV between 1.422 V and 1.423 V. Data points with pump voltage from 1.417 V to 1.421 V are not accurate because of the same reason for the 63 nT curve in Fig. 5.7. This shows that this curve at this extremely low driving field is extremely steep where the ME coefficient increases effectively.

Measurement of the ME coefficient curve as a function of the pump voltage with an even smaller driving field has presented difficulties. For small pump voltages, the signal was lower than the background noise level. For pump voltage that is close to the threshold, the ME coefficient displays rapid increment. What makes it even more difficult is the fact that the threshold drifts slowly at a rate of approximately 0.1 mV/hour. As Eq. (5.14) shows, this small

drifting comes from the variation of natural quality factor which has to do with the stability of the cantilever and vacuum level system. It is this drifting and the steep increase in the ME coefficient-pump voltage plot that prevent us from measuring a lower magnetic field. The 282 pT is the lowest driving field that we can detect with parametric amplification in the present set-up with the current device. With a time constant of 1 s and an equivalent noise bandwidth of 0.078 Hz, this gave a sensitivity of $1 \text{ nT}/\sqrt{\text{Hz}}$ measured at 3546 Hz.

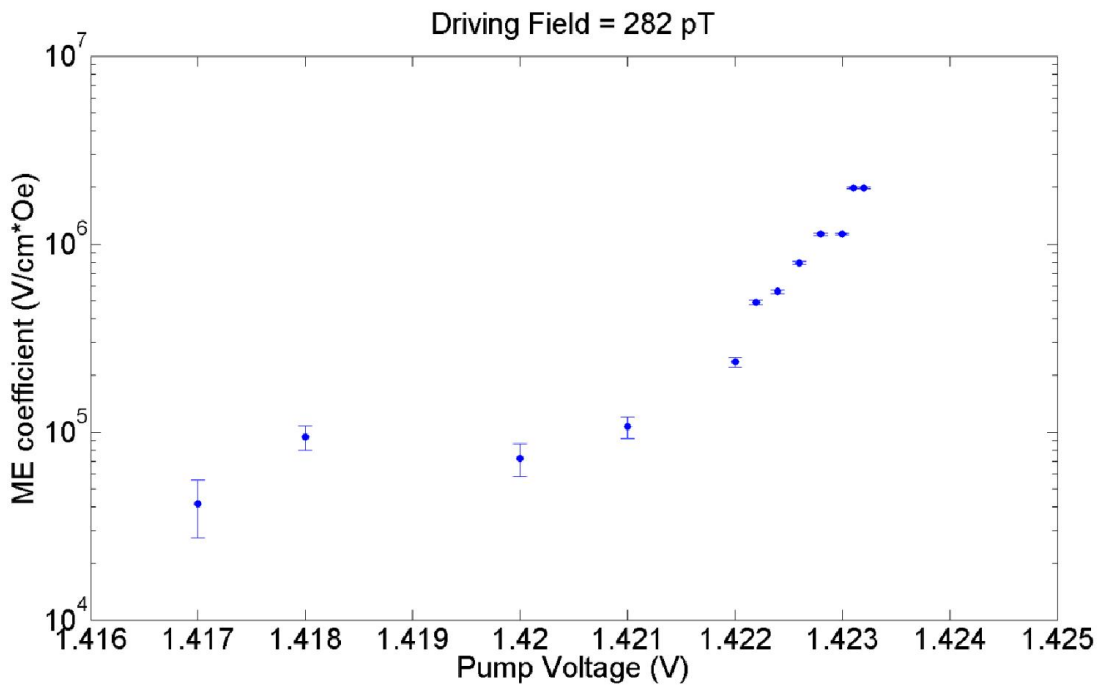


Fig. 5.8 The ME coefficient as a function of pump voltage with driving magnetic field of 282 pT (RMS).

It is important to point out that when the driving magnetic field is lowered to 282 pT, the maximum gain is 60,000 to boost the ME coefficient from 33 V/(cm × Oe) without parametric pump up to 2,000,000 V/(cm × Oe) with pump voltage extremely close to the threshold voltage. This is the highest ME coefficient we have seen to date.

5.4.3 Quality Factor as a Function of Gain or ME voltage

According to Reference [145], the quality factor increases and is proportional to $1/\sqrt{1 - (k_p/k_t)^2}$. This is because the pumping signal can be seen as compensation to the loss of the system, which would then increase the quality factor. In our case, $k_p/k_t = V_p/V_t = 1 - \frac{1}{\text{Gain}}$.

Then Q is related to gain in such way that

$$Q = Q_0 / \sqrt{1 - \left(1 - \frac{1}{\text{Gain}}\right)^2} \quad , \quad (5.15)$$

where $Q_0 = 2300$ is the quality factor without pumping. Eq. (5.15) is plotted in Fig. 5.9 (a) as a theory prediction compared to measured Q values. As we can see, the theory predicts the experimental quality factor values well for the gain less than 1000. However, the quality factor for curves for driving field of 2.82 nT and 0.282 nT start to saturate beyond the gain of 1000 instead of rising higher as the theory predicts. The flattening is due to the fact we are limited to measure Q of 70,000. Given that the resonant frequency is around 3500 Hz, the bandwidth for a frequency response curve with the Q of 70,000 is only 50 mHz. To measure such a small bandwidth, the time constant has to be more than 3 s, making the scanning time of an 80 pixels by 80 pixels intensity plot to be hours, which is too long given the drift in the experiment. To pursue higher Q than 70,000, one can use smaller devices, which have higher resonant frequencies. For example, if the resonant frequency is increased to 3 MHz, the bandwidth of a frequency response curve will be 50 Hz for a quality factor of 70,000. In this case, the time constant can be set to 3 ms, which will reduce the scanning time 1000 times compared with a scan with time constant of 3 s.

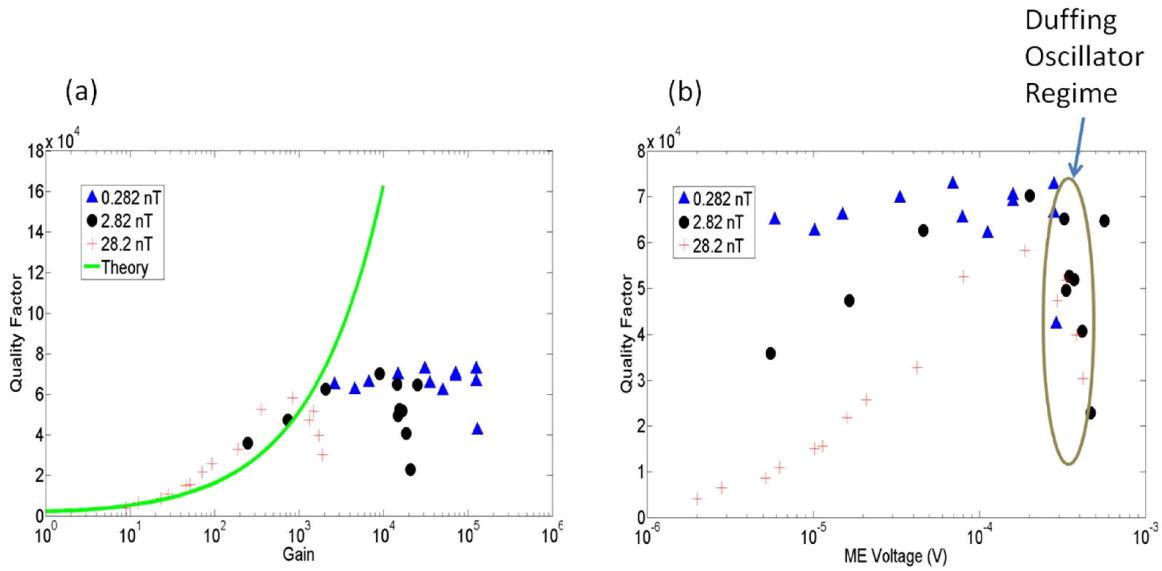


Fig. 5.9 (a) and (b) shows quality factor as a function of gain and ME Voltage, respectively, with different driving field (RMS).

In addition to this saturation, the Q values eventually all begins to fall when the gain is increased to a certain level. We can clearly see this behavior in Fig. 5.9 (b), where all three curves begin to display sudden decrease at about the same ME voltage, at around 0.4 mV. This is the voltage where the cantilever starts to be affected by the Duffing effect, which distorts the frequency scanning curve and widens its bandwidth. This leads to the quality factor to decrease.

5.5 Assessing the Noise

From Fig. 5.8 (b), one can also see that all three curves have a noise level of about $2 \mu\text{V}/\sqrt{\text{Hz}}$. This noise level is considered to be pretty high in a typical sensitivity measurement. For comparison, in the magnetic linear mode measurements described in Chapter 3, the noise floor was about $10 \text{ nV}/\sqrt{\text{Hz}}$ to $20 \text{ nV}/\sqrt{\text{Hz}}$, roughly one hundred times smaller. Some of the noise in parametric amplification measurement comes from the function generator, which is providing the

pump voltage. Considering that it provides about 1V of pump voltage, the error of 1 μV , which is 1 ppm of the output voltage, is not unreasonable.

The lock-in amplifier is also partially responsible because it has to work in the high dynamic reserve mode to filter the large signal at the pumping frequency ($2\omega_{\text{driving}}$) when it is measuring at the driving frequency (ω_{driving}), because the high dynamic reserve mode has a much higher noise than the low noise mode. Even though we have a band pass filter with a bandwidth of 100 Hz to help minimize the pumping signal before the lock-in amplifier, it is apparently not enough to minimize it.

Another source of noise is the vacuum pressure and the temperature drift. We explained that the threshold voltage, which is the critical value for the pump voltage to reach, depends on the quality factor in Eq. (5.14). In Fig. 5.8, we showed that the ME signal is so sensitive that even 0.1 mV change in pump voltage results in a large change in the ME signal. Because according to Eq. (5.14) threshold voltage V_t is inversely proportional to the quality factor, which is then sensitive to vacuum pressure and temperature, 0.1% change in vacuum pressure or temperature can easily lead to change in the threshold voltage V_t .

It is because of the extra noise mentioned above that even though the quality factor is improved by 30 times from 2300 to 70,000, the sensitivity is only improved by 6 times.

5.6 Conclusion

We have demonstrated that the parametric amplification method can be applied to magnetic field sensing for our multiferroic cantilevers. With the pump voltage modulating the spring constant of the cantilever, the magnetoelectric voltage is found to be sensitive to both the phase

of the pump voltage and the phase of the driving field. The ME coefficient is significantly boosted as the pump voltage approaches the threshold voltage.

In our measurement, we used the time constant of 1 second for the lock-in amplifier whose equivalent noise bandwidth is 0.078 Hz. Because the lowest detectable magnetic field is 282 pT, the sensitivity with parametric amplification is then $1.0 \text{ nT}/\sqrt{\text{Hz}}$. This sensitivity is 6 times better compared to the sensitivity without parametric amplification, which is about $6 \text{ nT}/\sqrt{\text{Hz}}$. The enhancement of sensitivity is not as much as what the ME coefficient has increased. This is because noise in the parametric amplification mode is two orders higher than that of the purely magnetic driving mode. The parametric amplification is able to boost the ME coefficient up to 60,000 times higher than the original value, and the ME coefficient as high as $2,000,000 \text{ V}/(\text{cm} \times \text{Oe})$ has been recorded. On the other hand, the parametric amplification mode can only improve the sensitivity by 6 times due to the increased level of the noise.

With parametric amplification the quality factor has increased from 2300 to 70,000 with applied pump voltage. The stability of the natural quality factor of the system, which defines the threshold voltage, is critical. To further improve the noise background level and the stability of the gain-pump voltage curve, more effort needs to be made to have better electronics and less drift in vacuum pressure and temperature.

Chapter 6: Summary and Future Work

In this thesis, we have characterized our multiferroic FeGa/PZT cantilevers, in a variety of operating modes: the linear mode, the Duffing nonlinear mode, and the parametric amplification mode. We have demonstrated their applications in magnetic field sensors, energy harvesters, dynamic mechanical memory devices, and parametric amplification assisted magnetic field sensors.

The heterostructured multiferroic cantilevers that we are working with consist of a piezoelectric PZT layer and a magnetostrictive FeGa layer. PZT with the Zr/Ti ratio of 0.52:0.48 is chosen to be our piezoelectric material because of its high piezoelectric coefficient at the Morphotropic Phase Boundary (MPB). The PZT layer is fabricated by a sol-gel technique followed by rapid thermal annealing so that an optimized piezoelectric coefficient d_{31} of 120 pC/N is obtained. The FeGa layer is fabricated with the magnetron sputtering method. The Fe/Ga ratio of 0.7:0.3 ensures that the magnetostriction of FeGa maximizes with λ of 180 ppm. The detail of this heterostructured device was introduced in Section 3.2. The cantilever is naturally a magnetic field sensor, which converts AC magnetic field signals to AC voltage signals via the magnetoelectric (ME) coupling effect. The ME coefficient is a figure of merit of the ME magnetic field sensor. With the same piezoelectric film thickness and the same noise floor level, the ME sensors with a higher ME coefficient will be more sensitive. For a multiferroic cantilever, its ME coefficient is enhanced by the mechanical resonance. Compared with larger cantilevers ($4.5 \text{ mm} \times 20 \text{ mm} \times 30 \text{ }\mu\text{m}$) with a ME coefficient of $4.5 \text{ V}/(\text{cm} \times \text{Oe})$ previously fabricated by Peng, *et al.*, the small cantilevers ($0.95 \text{ mm} \times 0.2 \text{ mm} \times 5 \text{ }\mu\text{m}$) have the ME coefficient of $33 \text{ V}/(\text{cm} \times \text{Oe})$ at the resonant frequency of 3833 Hz with DC magnetic bias field of 66.1 Oe in vacuum at room temperature. This enhancement of the ME coefficient is due to the minimized

clamping effect from the thinner substrate. The small cantilever has a resonant frequency 10 times larger than that of the large cantilever. Also, even at 3833 Hz, the equivalent magnetic field noise of the device is still pretty high ($1.2 \text{ nT}/\sqrt{\text{Hz}}$) compared to other ME sensors [16,53]. The high noise is mostly because the cantilever has a small size, which captures small magnetic flux. An option of reducing such noise due to the small size is to develop sensor arrays. Sensor arrays with N sensors in it can have $1/\sqrt{N}$ times less noise than a single sensor [146]. In addition, to increase the ME coefficient of the device, AlN can replace PZT and Metglas can replace FeGa in future devices. As the ME coefficient increased, the equivalent magnetic field noise will be lowered. It is important to note however that AlN with its low piezoelectric coefficient will not allow operation of the device in the nonlinear regime, discussed in the rest of the thesis. Also, to make the sensor useful in low frequencies (0.01~1000 Hz) where the $1/f$ noise dominates, the flux concentrator modulation or the frequency conversion technique can be used in future [83,114].

In Chapter 3, by operating our small multiferroic heterostructured FeGa/PZT cantilever ($0.95 \text{ mm} \times 0.2 \text{ mm} \times 5 \text{ }\mu\text{m}$) in the linear mode where the AC magnetic field used to drive the cantilever is less than 3 Oe, we found that the resonant frequency of the cantilever shifts with DC bias magnetic field H_{DC} linearly. This is different from the behavior of larger cantilevers, where the resonant frequency is not affected by H_{DC} . A magnetic cantilever theory, which takes into account the combined effects of the elastic energy, the internal stress, the Zeeman energy, the demagnetization, and the magnetoelastic energy, is used to explain the resonant frequency shift. As an energy harvester, the cantilever is able to deliver electric energy with an efficiency of $0.7 \text{ mW}/\text{cm}^3$ when 1 Oe AC magnetic field is applied at the resonant frequency. This efficiency is close to those of the bulk devices that have been reported. The small dimensions of the present

device enable it to be an ideal power source for wireless microelectromechanical systems (MEMS) where changing of batteries is not desirable.

In Chapter 4, we operated the cantilever in the nonlinear mode with AC magnetic field higher than 3 Oe or the voltage larger than 5 mV. The intense driving force makes the Duffing term k_3x^3 substantial in the large amplitude limit. A bifurcation area arises near the resonant frequency in the frequency response. When the cantilever is driven at a frequency inside the bifurcation area, the cantilever can have two possible amplitudes, which gives two possible voltage or current readouts of the device corresponding to the ‘up’ and ‘down’ states. These two states are switchable by tuning the driving frequency, the AC magnetic field amplitude, the DC bias magnetic field, or the DC bias electric field. Thus, the cantilevers are multi-mode switchable memory devices based on nonlinear mechanical vibration. The memory devices are scalable, and their operating frequencies can be increased from 3500 Hz to GHz by making the devices smaller (*e.g.*, 100 nm in length). They will also consume less power when the size goes down, because the associated mechanical energy will also be smaller. Thus, making smaller sized devices is a clear future direction.

In Chapter 5, we used parametric amplification to operate the device in another nonlinear mode, so that the ME coefficient of our multiferroic cantilevers is substantially increased. In this mode, a pump signal added to the PZT layer is used to modulate the spring constant of the cantilever at double the resonant frequency. The gain is then found to be sensitive to both the phase of the pump signal and the phase of the driving magnetic field. With both phases carefully chosen to maximize the gain, the gain increases nonlinearly as we increase the pump voltage. The gain of parametric amplification diverges when the pump voltage approaches the threshold voltage. With a maximum gain of 60,000, we are able to increase the ME coefficient up to

2,000,000 V/(cm × Oe). This is the highest ME coefficient measured to the best of our knowledge. The quality factor (Q) of the cantilever also increased from 2300 without pump signal to 70,000 with the pump signal. Even though the ME coefficient is significantly increased, the magnetic field sensitivity of the cantilever only improved by one order from 6 nT/ $\sqrt{\text{Hz}}$ to 1 nT/ $\sqrt{\text{Hz}}$. This is because the noise floor of the system is still very high, 2 $\mu\text{V}/\sqrt{\text{Hz}}$ with parametric amplification compared to 10~20 nV/ $\sqrt{\text{Hz}}$ without parametric amplification. The possible noise sources are the noise from the voltage source that provides the pump signal, the fact that the lock-in amplifier works in dynamic reserve mode instead of the low noise mode and drift in vacuum and temperature. If these noises can be reduced further, our multiferroic cantilevers would be more sensitive in measuring AC magnetic field.

Appendix

A.1 Using a Nyquist-like Plot to Subtract the Inductive Signal

The ME signal in the voltage signal are measured with application of magnetic field. The ME signal is in phase with the AC magnetic field. In systems containing magnetic field, there is usually an inductive voltage signal, which is 90 degrees out of phase with the AC magnetic phase. It is important to properly separate the inductive signal from the ME signal. For this purpose, we use the Nyquist-like plot.

The Nyquist plot is often used in the feedback control system to analyze the stability of the system. Considering a system with transfer function of $G(j\omega)$, where G is the gain, j is the imaginary unit, and ω is the driving frequency, the Nyquist plot is the plot of $\text{Re}(G)$ as a function of $\text{Im}(G)$, where $\text{Re}(G)$ is the real part of the gain and $\text{Im}(G)$ is the imaginary part.

However, we will plot ‘Nyquist-like’ plots instead of Nyquist plots. This is because we are going to plot Signal (in phase) as a function of Signal (out of phase) instead of $\text{Re}(G)$ as a function of $\text{Im}(G)$. The in phase and out of phase signal are X and Y signal of the lock-in amplifier.

The reason we want to use the Nyquist-like plot is to separate and remove the inductive signal from the ME signal. When raw data of the device signal is plotted in an intensity plot in Fig. A.1 (a), we often find some of the frequency dependent response (spectra) to displays a negative peak next to a positive peak, as seen in the inset figure. In fact, for the spectra at high DC magnetic fields, the responses only have negative peaks. These negative peaks are due to the inductive effect. We cannot increase the ME signal to inductive signal ratio simply by increasing driving field, because the inductive signal is also proportional to driving field. In the case when the ME signal is high, the inductive signal may not be a serious problem. However, in the case

when the ME signal is small, such as if the device operates in atmosphere instead of in vacuum, the inductive signal will cause a problem in isolating the ME signal. We thus perform a post-measurement data processing to consistently remove the inductive signal.

As previously mentioned, we turned to the Nyquist-like plot (lock-in Y versus lock-in X) to adjust the inductive signal. Fig. A.1 (b) is the Nyquist-like plot data extracted from Fig. A.1 (a). First, one notices that there are two groups of circles of data. The smaller circles correspond to data from signals when H_{DC} is larger than 75 Oe, while the larger circles correspond to data from signals when H_{DC} is smaller than 75 Oe. Each circle corresponds to a frequency spectrum at one particular DC magnetic field. Because the magnetization of magnetic layer (FeGa) is reversed at 75 Oe and the $\frac{d\lambda}{dH}$ reverse the sign as we discussed in Section 4.2.2, there is a 180 degrees phase change in the signal at 75 Oe, and this is why these two groups of data are “opposite” to each other by 180 degrees. Then, on the same circle, data points have the same DC magnetic field but different driving frequencies. The open parts, which all the circles have, are due to the fact that we can only scan a limited range of the driving frequency. The data points close to the open parts of the circles have driving frequency far away from the resonant frequency. Thus, in theory, these data points should be close to zero in both X and Y channels. As we can see, the open parts of the circles in Fig. A.1 (b) have an offset away from the origin of the plot. This offset is mostly due to the inductive signal. As a result, to remove the inductive signal, we only need to translate the entire dataset so that the open parts of the circles are at the origin of the Y-X plot, as done in Fig. A.1 (c). Now if we plot the adjusted Nyquist-like plot in (c) back into 3D color map, we have Fig. A.1 (d). In Fig. A.1 (d), one sees that the spectra all have symmetric upside peaks (as seen in the inset), and the signal only contains the resonant ME signal. Another point one notices is that in this process we had also rotated the circles along the open part from the plot in Fig. A.1

(c), which will make the X channel data symmetric and Y channel data antisymmetric with respect to the driving frequency. However, the rotation is unnecessary if we are to only remove the inductive signal.

The Nyquist-like adjustment is necessary to preprocess our data to remove the inductive signal. This is essential if we want to achieve high sensitivity in our magnetic field detection, using the ME signal.

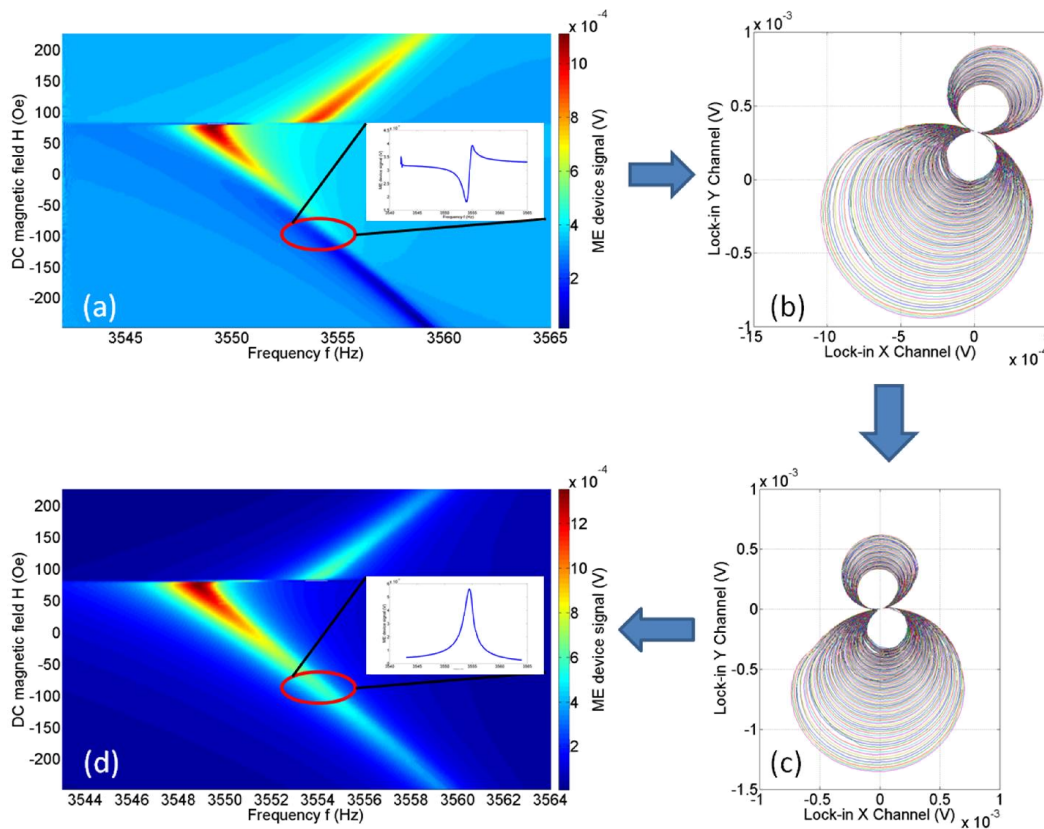


Fig. A.1 Nyquist adjustment process: (a) Frequency response data before the Nyquist adjustment. (b) Nyquist-like plot extracted from data in (a). (c) Nyquist-like plot after adjustment. (d) Data recovered from (c).

A.2 Fit Frequency Response with Lorentzian Function

When the device is driven linearly, under small enough magnetic field or electric field, the frequency response of the signal S squared fits a Lorentzian function. Thus, following the use of the Nyquist-like plot to remove inductive signal, we need to fit our S^2 as a function of the driving frequency with a Lorentzian function, that is

$$S^2 = \frac{1}{\pi} \times \frac{A \times \frac{\text{Width}}{2}}{(f-f_0)^2 + \left(\frac{\text{Width}}{2}\right)^2}, \quad (\text{A.1})$$

, where S is ME signal in volt, Width is bandwidth, f is driving frequency, f_0 is resonant frequency, $2A/(\text{Width} \times \pi)$ is fitted amplitude in Volt^2

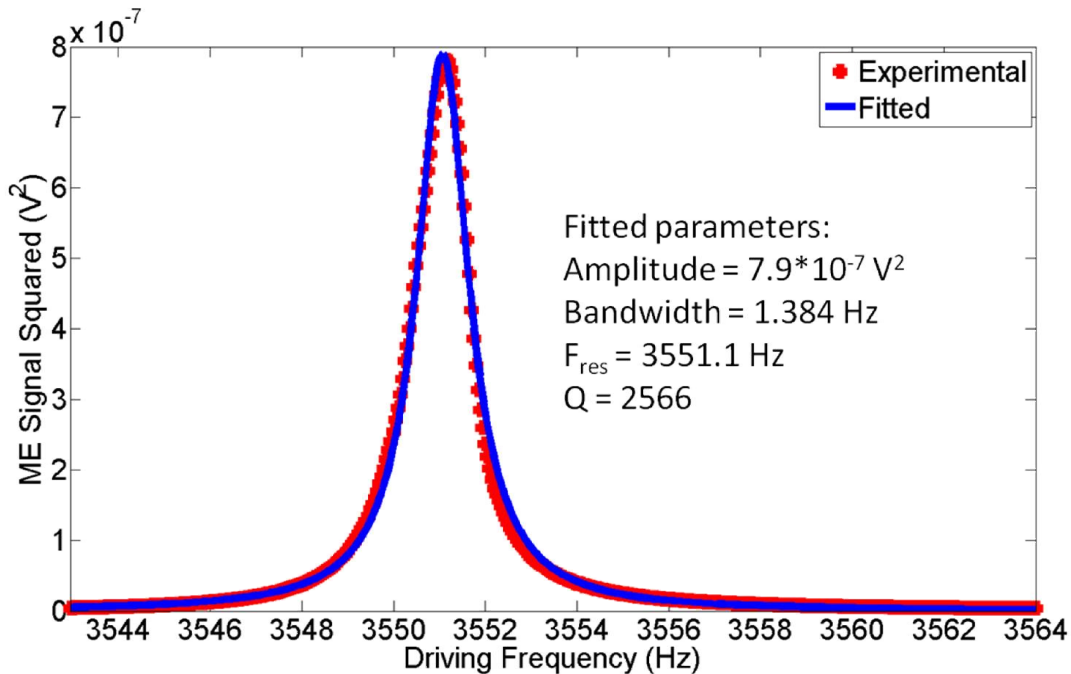


Fig. A.2 ME signal squared as a function of driving frequency is fitted to a Lorentzian function.

As we can see in Fig. A.2, after the ME signal is squared, its frequency response fits with the Lorentzian function of Eq. (A.1) well. With the fitted function, resonant frequency, bandwidth, and quality factor (Q) can be easily extracted.

Bibliography

- [1] N. A. Spaldin and M. Fiebig, *Science* **309**, 391 (2005).
- [2] C. W. Nan, M. I. Bichurin, S. X. Dong, D. Viehland, and G. Srinivasan, *Journal of Applied Physics* **103**, 35, 031101 (2008).
- [3] Valasek, *Phys. Rev.*, pp. 537 , (1920).
- [4] **P. Curie**, *J. Physique*, (1894).
- [5] P. Debye, *Z. Phys.* 36, 300, (1926).
- [6] L. D. L. a. E. M. Lifshitz, (1960).
- [7] I. Dzyaloshinskii, *Zh. Exp. Teor. Fiz.*, p. 881, (1960).
- [8] D. Astrov, *Sov. Phys. JETP*, p. 708, (1960).
- [9] G. T. Rado and V. J. Folen, *Physical Review Letters* **7**, 310 (1961).
- [10] E. Ascher, H. Rieder, H. Schmid, and H. Stossel, *Journal of Applied Physics* **37**, 1404 (1966).
- [11] G. A. Smolensky, V. A. Isupov, N. N. Krainik, Agranovskaya, and A. I, *IsVest. Akad. Nauk SSSR, Ser. Fiz*, p. 1333, (1961).
- [12] J. V. Suchtelen, *Phillips Res. Rep*, pp. 28, (1972).
- [13] D. N. Astrov, *Sov. Phys. JETP*, p. 729, (1961).
- [14] C. W. Nan, *Physical Review B* **50**, 6082 (1994).
- [15] M. Avellaneda and G. Harshe, *Journal of Intelligent Material Systems and Structures* **5**, 501 (1994).
- [16] C. Kirchhof *et al.*, *Applied Physics Letters* **102**, 4, 232905 (2013).
- [17] K. G. Brooks, I. M. Reaney, R. Klissurska, Y. Huang, L. Bursill, and N. Setter, *Journal of Materials Research* **9**, 2540 (1994).
- [18] E. K. F. Dang and R. J. Gooding, *Physical Review Letters* **74**, 3848 (1995).

- [19] J. R. Hattnick-Simpers *et al.*, Applied Physics Letters **93**, 3, 102507 (2008).
- [20] D. Hunter *et al.*, Nature Communications **2**, 7, 518 (2011).
- [21] L. Wang and F. G. Yuan, Smart Materials and Structures **17**, 14, 045009 (2008).
- [22] P. Zhao, Z. L. Zhao, D. Hunter, R. Suchoski, C. Gao, S. Mathews, M. Wuttig, and I. Takeuchi, Applied Physics Letters **94**, 3, 243507 (2009).
- [23] J. Das, J. Gao, Z. Xing, J. F. Li, and D. Viehland, Applied Physics Letters **95**, 3, 092501 (2009).
- [24] H. Greve, E. Woltermann, H. J. Quenzer, B. Wagner, and E. Quandt, Applied Physics Letters **96**, 3, 182501 (2010).
- [25] S. Marauska, R. Jahns, H. Greve, E. Quandt, R. Knochel, and B. Wagner, Journal of Micromechanics and Microengineering **22**, 6, 065024 (2012).
- [26] S. Ju, S. H. Chae, Y. Choi, S. Lee, H. W. Lee, and C. H. Ji, Smart Materials and Structures **22**, 11, 115037 (2013).
- [27] Y. Zhou, D. J. Apo, and S. Priya, Applied Physics Letters **103**, 5, 192909 (2013).
- [28] T. D. Onuta, Y. Wang, C. J. Long, and I. Takeuchi, Applied Physics Letters **99**, 3, 203506 (2011).
- [29] Y. H. Chu *et al.*, Nature Materials **7**, 478 (2008).
- [30] T. Zhao *et al.*, Nature Materials **5**, 823 (2006).
- [31] D. Kan, V. Anbusathaiah, and I. Takeuchi, Advanced Materials **23**, 1765 (2011).
- [32] N. A. Hill, Journal of Physical Chemistry B **104**, 6694 (2000).
- [33] B. B. Van Aken, T. T. M. Palstra, A. Filippetti, and N. A. Spaldin, Nature Materials **3**, 164 (2004).
- [34] T. Kimura, S. Ishihara, H. Shintani, T. Arima, K. T. Takahashi, K. Ishizaka, and Y. Tokura, Physical Review B **68**, 4, 060403 (2003).
- [35] D. Lebeugle, D. Colson, A. Forget, M. Viret, P. Bonville, J. F. Marucco, and S. Fusil, Physical Review B **76**, 8, 024116 (2007).
- [36] C. Ederer and N. A. Spaldin, Physical Review B **71**, 4, 060401 (2005).

- [37] T. Moriya, *Physical Review* **120**, 91 (1960).
- [38] I. E. Dzyaloshinskii, *Sov. Phys. JETP*, p. 1259, (1957).
- [39] W. Ratcliff, Z. Yamani, V. Anbusathaiah, T. R. Gao, P. A. Kienzle, H. Cao, and I. Takeuchi, *Physical Review B* **87**, 6, 140405 (2013).
- [40] C. J. Zuo, N. Sinha, J. Van der Spiegel, and G. Piazza, *Journal of Microelectromechanical Systems* **19**, 570 (2010).
- [41] R. E. Newnham, D. P. Skinner, and L. E. Cross, *Materials Research Bulletin* **13**, 525 (1978).
- [42] Vandenbo.J, D. R. Terrell, R. A. J. Born, and H. Giller, *Journal of Materials Science* **9**, 1705 (1974).
- [43] J. Vandenboomgaard, A. Vanrun, and J. Vansuchtelen, *Ferroelectrics* **10**, 295 (1976).
- [44] G. Srinivasan, E. T. Rasmussen, and R. Hayes, *Physical Review B* **67**, 10, 014418 (2003).
- [45] G. Srinivasan, E. T. Rasmussen, J. Gallegos, R. Srinivasan, Y. I. Bokhan, and V. M. Laletin, *Physical Review B* **64**, art. no. (2001).
- [46] J. Ryu, A. V. Carazo, K. Uchino, and H. E. Kim, *Japanese Journal of Applied Physics Part 1-Regular Papers Short Notes & Review Papers* **40**, 4948 (2001).
- [47] J. Ma, J. M. Hu, Z. Li, and C. W. Nan, *Advanced Materials* **23**, 1062 (2011).
- [48] D. R. T. A. M. J. G. Van Run, J. H. Scholing, *Journal of Materials Science*, 1974), pp. 1710.
- [49] R. A. Islam and S. Priya, *Journal of Materials Science* **43**, 3560 (2008).
- [50] R. A. Islam, Y. Ni, A. G. Khachaturyan, and S. Priya, *Journal of Applied Physics* **104**, 5, 044103 (2008).
- [51] J. Ryu, S. Priya, K. Uchino, and H. E. Kim, *Journal of Electroceramics* **8**, 107 (2002).
- [52] K. Mori and M. Wuttig, *Applied Physics Letters* **81**, 100 (2002).
- [53] S. X. Dong, J. Y. Zhai, J. F. Li, and D. Viehland, *Applied Physics Letters* **89**, 3, 252904 (2006).
- [54] S. X. Dong, J. Y. Zhai, S. Priya, J. F. Li, and D. Viehland, *Ieee Transactions on Ultrasonics Ferroelectrics and Frequency Control* **56**, 1124 (2009).

- [55] Z. Fang, S. G. Lu, F. Li, S. Datta, Q. M. Zhang, and M. El Tahchi, *Applied Physics Letters* **95**, 3, 112903 (2009).
- [56] N. Cai, C. W. Nan, J. Y. Zhai, and Y. H. Lin, *Applied Physics Letters* **84**, 3516 (2004).
- [57] J. Ma, Z. Shi, and C. W. Nan, *Advanced Materials* **19**, 2571 (2007).
- [58] J. X. Zhang, J. Y. Dai, L. C. So, C. L. Sun, C. Y. Lo, S. W. Or, and H. L. W. Chan, *Journal of Applied Physics* **105**, 6, 054102 (2009).
- [59] J. G. E. Gardeniers, A. Verholen, N. R. Tas, and M. Elwenspoek, *Journal of the Korean Physical Society* **32**, S1573 (1998).
- [60] J. Y. Zhai, S. X. Dong, Z. P. Xing, J. F. Li, and D. Viehland, *Applied Physics Letters* **89**, 3, 083507 (2006).
- [61] W. S. Lee and S. S. Lee, *Sensors and Actuators a-Physical* **144**, 367 (2008).
- [62] J. Hillenbrand and G. M. Sessler, *Ieee Transactions on Dielectrics and Electrical Insulation* **13**, 973 (2006).
- [63] J. N. Farrelly, (Krypton Systems LLC, 2013).
- [64] A. V. Carazo and K. Uchino, *Journal of Electroceramics* **7**, 197 (2001).
- [65] S. P. Beeby, M. J. Tudor, and N. M. White, *Measurement Science & Technology* **17**, R175 (2006).
- [66] W. G. Cady, (New York : Dover Publications, 1964).
- [67] A. Arnau, (Berlin ;New York : Springer, 2004).
- [68] A. Barzegar, D. Damjanovic, and N. Setter, *Ieee Transactions on Ultrasonics Ferroelectrics and Frequency Control* **51**, 262 (2004).
- [69] A. Daniels, M. L. Zhu, and A. Tiwari, *Ieee Transactions on Ultrasonics Ferroelectrics and Frequency Control* **60**, 2626 (2013).
- [70] P. T. company, <http://www.piezotechnologies.com/Ceramics/quick-selection-chart.aspx>.
- [71] M. W. Hooker, NASA/CR-1998-208708, 1998).

- [72] J. F. Scott and C. A. P. Dearaujo, *Science* **246**, 1400 (1989).
- [73] T. Tybell, C. H. Ahn, and J. M. Triscone, *Applied Physics Letters* **72**, 1454 (1998).
- [74] R. M. Bozorth, (New York : Van Nostrand, 1951).
- [75] D. Cohen, *Science* **175**, 664 (1972).
- [76] R. Salmelin, R. Hari, O. V. Lounasmaa, and M. Sams, *Nature* **368**, 463 (1994).
- [77] J. J. Chaillout, J. Berthier, and R. Blainpain, *IEEE Transactions on Magnetics* **32**, 998 (1996).
- [78] T. R. Clem, *Naval Research Reviews*, pp. 29, (1997).
- [79] L. Hao, J. C. Macfarlane, P. Josephs-Franks, and J. C. Gallop, *IEEE Transactions on Applied Superconductivity* **13**, 622 (2003).
- [80] T. H. Sander, J. Preusser, R. Mhaskar, J. Kitching, L. Trahms, and S. Knappe, *Biomedical Optics Express* **3**, 981 (2012).
- [81] W. F. Egelhoff, P. W. T. Pong, J. Unguris, R. D. McMichael, E. R. Nowak, A. S. Edelstein, J. E. Burnette, and G. A. Fischer, *Sensors and Actuators a-Physical* **155**, 217 (2009).
- [82] D. Robbes, *Sensors and Actuators a-Physical* **129**, 86 (2006).
- [83] A. S. Edelstein, G. A. Fischer, M. Pedersen, E. R. Nowak, S. F. Cheng, and C. A. Nordman, *Journal of Applied Physics* **99**, 6, 08b317 (2006).
- [84] M. Pannetier, C. Fermon, G. Le Goff, J. Simola, and E. Kerr, *Science* **304**, 1648 (2004).
- [85] S. X. Dong, J. F. Li, and D. Viehland, *Applied Physics Letters* **83**, 2265 (2003).
- [86] Y. J. Wang, D. Gray, D. Berry, J. Q. Gao, M. H. Li, J. F. Li, and D. Viehland, *Advanced Materials* **23**, 4111 (2011).
- [87] R. Jahns, H. Greve, E. Woltermann, E. Quandt, and R. Knochel, *Sensors and Actuators a-Physical* **183**, 16 (2012).
- [88] M. A. Dubois and P. Muralt, *Applied Physics Letters* **74**, 3032 (1999).
- [89] J. Zhai, (2009).

- [90] A. G. Olabi and A. Grunwald, *Materials & Design* **29**, 469 (2008).
- [91] E. P. Wohlfarth, North Holland Publ. Co., (1980).
- [92] A. E. Clark, J. B. Restorff, M. Wun-Fogle, T. A. Lograsso, and D. L. Schlager, *IEEE Transactions on Magnetics* **36**, 3238 (2000).
- [93] A. E. Clark, K. B. Hathaway, M. Wun-Fogle, J. B. Restorff, T. A. Lograsso, V. M. Keppens, G. Petculescu, and R. A. Taylor, *Journal of Applied Physics* **93**, 8621 (2003).
- [94] metglas.com, http://metglas.com/products/magnetic_materials/2714a.asp.
- [95] P. C. Fannin, C. N. Marin, I. Malaescu, N. Stefu, P. Vlazan, S. Novaconi, P. Sfirloaga, S. Popescu, and C. Couper, *Materials & Design* **32**, 1600 (2011).
- [96] V. L. O. de Brito, S. A. Cunha, L. V. Lemos, and C. B. Nunes, *Sensors* **12**, 10086 (2012).
- [97] H. T. a. I. Takeuchi, (Unpublished).
- [98] W. J. Lee, Y. M. Kim, and H. G. Kim, *Thin Solid Films* **269**, 75 (1995).
- [99] B. Piekarski, M. Dubey, E. Zakar, R. Polcawich, D. DeVoe, and D. Wickenden, *Integrated Ferroelectrics* **42**, 25 (2002).
- [100] X. J. Meng, J. G. Cheng, J. L. Sun, J. Tan, H. J. Ye, and J. H. Chu, *Thin Solid Films* **368**, 22 (2000).
- [101] A. Chand, M. B. Viani, T. E. Schaffer, and P. K. Hansma, *Journal of Microelectromechanical Systems* **9**, 112 (2000).
- [102] T. R. Albrecht, P. Grutter, D. Horne, and D. Rugar, *Journal of Applied Physics* **69**, 668 (1991).
- [103] J. P. Cleveland, S. Manne, D. Bocek, and P. K. Hansma, *Review of Scientific Instruments* **64**, 403 (1993).
- [104] H. G. Craighead, *Science* **290**, 1532 (2000).
- [105] S. Marauska, R. Jahns, C. Kirchhof, M. Claus, E. Quandt, R. Knochel, and B. Wagner, *Sensors and Actuators a-Physical* **189**, 321 (2013).
- [106] Z. J. Davis *et al.*, *Sensors and Actuators a-Physical* **105**, 311 (2003).

- [107] Bbanerje, (<http://en.wikipedia.org/wiki/File:BeamVibrationPlot.svg>).
- [108] S. K. Lee and M. V. Romalis, *Journal of Applied Physics* **103**, 10, 084904 (2008).
- [109] B. C. Stipe, H. J. Mamin, T. D. Stowe, T. W. Kenny, and D. Rugar, *Physical Review Letters* **86**, 2874 (2001).
- [110] N. M. W. P. Glynn-Jones, *Sensor Review*, pp. 91, (2001).
- [111] I. CardioMEMS,
www.cardiomems.com/content.asp?display=aboutus&view=technology%20overview.
- [112] S. X. Dong, J. Y. Zhai, J. F. Li, D. Viehland, and S. Priya, *Applied Physics Letters* **93**, 3, 103511 (2008).
- [113] R. C. O'Handley, J. K. Huang, D. C. Bono, and J. Simon, *Ieee Sensors Journal* **8**, 57 (2008).
- [114] R. Jahns *et al.*, *Journal of the American Ceramic Society* **96**, 1673 (2013).
- [115] E. Lage, C. Kirchhof, V. Hrkac, L. Kienle, R. Jahns, R. Knochel, E. Quandt, and D. Meyners, *Nature Materials* **11**, 523 (2012).
- [116] I. Kovacic, 2011).
- [117] Z. Liu, (Shanghai Scientific and Technology Education Shanghai, China, 1994), pp. 36.
- [118] G. Y. Wang, D. J. Chen, J. Y. Lin, and X. Chen, *Ieee Transactions on Industrial Electronics* **46**, 440 (1999).
- [119] L. Kocarev and U. Parlitz, *Physical Review Letters* **74**, 5028 (1995).
- [120] W. J. Venstra, H. J. R. Westra, and H. S. J. van der Zant, *Nature Communications* **4**, 6, 2624 (2013).
- [121] R. Almog, S. Zaitsev, O. Shtempluck, and E. Buks, *Applied Physics Letters* **88**, 3, 213509 (2006).
- [122] T. Kanamaru, *Scholarpedia*, 2008), p. 6327.
- [123] W. J. Venstra, H. J. R. Westra, and H. S. J. van der Zant, *Applied Physics Letters* **97**, 3, 193107 (2010).
- [124] Y. Arimoto and H. Ishiwara, *Mrs Bulletin* **29**, 823 (2004).

- [125] Y. J. Chen, T. Fitchorov, C. Vittoria, and V. G. Harris, *Applied Physics Letters* **97**, 3, 052502 (2010).
- [126] T. Rueckes, K. Kim, E. Joselevich, G. Y. Tseng, C. L. Cheung, and C. M. Lieber, *Science* **289**, 94 (2000).
- [127] I. Mahboob and H. Yamaguchi, *Nature Nanotechnology* **3**, 275 (2008).
- [128] R. L. Badzey, G. Zolfagharkhani, A. Gaidarzhy, and P. Mohanty, *Applied Physics Letters* **85**, 3587 (2004).
- [129] D. D. Nolte, *Physics Today* **63**, 33 (2010).
- [130] R. Q. Almudena Suárez, pp. 27.
- [131] Y. V. Mikhlin, T. V. Shmatko, and G. V. Manucharyan, *Computers & Structures* **82**, 2733 (2004).
- [132] *D. t. Haar*, (1995).
- [133] A. Baxter, http://www.storagereview.com/ssd_vs_hdd.
- [134] T. Kawahara *et al.*, *Ieee Journal of Solid-State Circuits* **43**, 109 (2008).
- [135] R. Takemura *et al.*, *Ieee Journal of Solid-State Circuits* **45**, 869 (2010).
- [136] M. Bibes and A. Barthelemy, *Nature Materials* **7**, 425 (2008).
- [137] Q. M. Wang, T. Zhang, Q. M. Chen, and X. H. Du, *Sensors and Actuators a-Physical* **109**, 149 (2003).
- [138] H. Kawakatsu, S. Kawai, D. Saya, M. Nagashio, D. Kobayashi, H. Toshiyoshi, and H. Fujita, *Review of Scientific Instruments* **73**, 2317 (2002).
- [139] X. K. Sun, J. J. Zheng, M. Poot, C. W. Wong, and H. X. Tang, *Nano Letters* **12**, 2299 (2012).
- [140] G. Prakash, A. Raman, J. Rhoads, and R. G. Reifenberger, *Review of Scientific Instruments* **83**, 12, 065109 (2012).
- [141] D. Rugar and P. Grutter, *Physical Review Letters* **67**, 699 (1991).
- [142] M. Sharma, E. H. Sarraf, R. Baskaran, and E. Cretu, *Sensors and Actuators a-Physical* **177**, 79 (2012).

- [143] W. H. Zhang, R. Baskaran, and K. L. Tumer, *Sensors and Actuators a-Physical* **102**, 139 (2002).
- [144] T. D. Onuta, Y. Wang, C. J. Long, S. E. Lofland, and I. Takeuchi, *Applied Physics Letters* **101**, 4, 043506 (2012).
- [145] R. Lifshitz and M. C. Cross, *Nonlinear Dynamics of Nanomechanical and Micromechanical Resonators* 2008).
- [146] Z. H. Huang and X. P. Wang, *Optical Engineering* **52**, 6, 044403 (2013).

Yi Wang

University of Maryland • Department of Physics

College Park, Maryland 20742 USA

billwang0102@gmail.com

EDUCATION

Ph.D., Physics (Aug 2014)

University of Maryland, College Park, USA

Thesis topic: Characterization and applications of FeGa/PZT multiferroic cantilevers

Advisor: Ichiro Takeuchi

B.S., Physics (Jun 2008)

Nanjing University, Nanjing, China

PROFESSIONAL AFFILIATIONS

- American Physical Society (APS) 2012-Present
 - Materials Research Society (MRS) 2013-Present
-

PUBLICATIONS

1. **Y. Wang***, T. Onuta*, and I. Takeuchi, “Parametric Amplified Magnetic Sensing with Multiferroic Device”, to be published (2014).
2. T. Onuta, **Y. Wang**, S. E. Lofland, and I. Takeuchi, “Robust MEMS Flipflop based on Nonlinear Multiferroic Cantilevers”, submitted to Nature Physics, 2014.
3. **Y. Wang**, T. Onuta, C. J. Long, S. E. Lofland, and I. Takeuchi, “All-thin-film PZT/FeGa Multiferroic Cantilevers Resonant Frequency Shifting and Applications in Energy Harvesting, Switching”, Proceeding of the 16th US-Japan seminar on dielectric and piezoelectric materials, 205-207, 2013.
4. **Y. Wang***, T. Onuta*, C. J. Long, S. E. Lofland, and I. Takeuchi, “Dynamic state switching in nonlinear multiferroic cantilevers”, Applied Physics Letters 101, 043506 (2012).
5. T. Onuta, **Y. Wang**, C. J. Long, and I. Takeuchi, “Energy harvesting properties of all-thin-film multiferroic cantilevers”, Applied Physics Letters 99, 203506 (2011).

PATENT TO BE SUBMITTED

Multifunctional multiferroic cantilevers for use in magnetic field sensors and dynamic memory devices.

SELECTED CONFERENCE TALKS & POSTERS

1. **Y. Wang**, T. Onuta, C. J. Long, I. Takeuchi, S. E. Lofland, “All-thin-film PZT/FeGa Multiferroic Cantilevers and Their Applications in Memory Devices and Parametric Amplification”, Materials Research Society Fall Meeting, Boston, MA, December 2013.
2. **Y. Wang**, T. Onuta, C. J. Long, and I. Takeuchi, “Energy Harvesting Properties of All-thin-film Multiferroic Cantilevers”, PiezoMEMS, Dulles, VA, April 2013.
3. **Y. Wang**, T. Onuta, S. E. Lofland, and I. Takeuchi, “Multimode Characterization of FeGa/PZT Multiferroic Thin Film Devices”, Center for Nanophysics and Advanced Materials Seminar, College Park, MD, March 2013.
4. **Y. Wang**, T. Onuta, C. J. Long, S. E. Lofland, and I. Takeuchi, “Dynamic state switching in nonlinear multiferroic cantilevers”, American Physics Society March Meeting, Baltimore, MD, March 2013.
5. **Y. Wang**, T. Onuta, C. J. Long, and I. Takeuchi, “Characterization of FeGa/PZT Multiferroic Thin Film Devices”, Center for Nanophysics and Advanced Materials Seminar, College Park, MD, April 2012.